THERMAL TRANSPORT THROUGH INDIVIDUAL NANOSTRUCTURES AND THEIR CONTACTS

By

YANG YANG

Dissertation

Submitted to the faculty of the

Graduate School of Vanderbilt University

in partial fulfillment of the requirements

for the degree of

DOCTOR OF PHILOSOPHY

in

Mechanical Engineering

August, 2013

Nashville, Tennessee

Approved:

Professor Deyu Li

Professor Robert W. Pitz

Professor Greg Walker

Professor Yaqiong Xu

To my parents and sisters

for their love, faith and constant support through my life

ACKNOWLEDGEMENTS

I would like to thank my advisor Prof. Deyu Li for his sharp insight and inspiration which guided me into the field of micro/nanoscale heat transfer and gave me the opportunity to deal with cutting-edge scientific and engineering problems. I'm also grateful for Prof. Li's patience, trust and constant encouragement as well as his rigorous attitude and critical thinking towards everything that will have a lifetime impact on me. He always expresses his hope for me to be an independent researcher and I regard this expectation as a strong commitment I made to myself.

I would like to thank Dr. Juekuan Yang for his selfless help as a mentor and collaborator during my Ph.D. study. His intelligence, depth of thinking, problem-solving ability and willingness to help, gave me a good example of how great a researcher and person could be.

I would like to thank Prof. Terry T. Xu, Zhe Guan and Youfei Jiang for their excellent work as strong and reliable partners in conquering scientific and technological puzzles.

I am grateful to my committee members: Profs. Robert W. Pitz, D. G. Walker and Yaqiong Xu for their time and valuable advices.

I'm extremely thankful to the help, companion and happiness brought by the past and present members I met in Prof. Deyu Li's group: Dr. Saumitra K. Vajandar, Dr. Jiashu Sun, Dr. Yandong Gao, Dr. Min Chen, Dr. Yanyan Ge, Dr. Virginia Pensabene,

Scott W. Waltermire, Bryson Brewer, Qian Zhang, Kyle G. Otte, Lijie Yang, Kirsten A. Heikkinen. I really enjoyed my life here and you made it a wonderful experience for me.

I also want to express my deep appreciation to Vanderbilt University and the National Science Foundation, for their financial support throughout my entire Ph.D. study.

For an experimentalist like me, facility support is extremely important. I want to thank the support from Cornell Nanoscale Science & Technology Facility (CNF), Center for Nanophase Material Science (CNMS) at Oak Ridge National Laboratory and Vanderbilt Institute of Nanoscale Science and Engineering (VINSE).

Five years has been a long journey in my life. There were ups and downs, whenever I shared my joys or tears, my parents and sisters were always there, even though they normally sit thousands of miles away, on the other side of the Pacific Ocean. Without them, I will never be able to complete this dissertation.

Finally, to all the lovely and kind friends I met at Vanderbilt, Nashville and in the U. S.: it’s my great pleasure to have you all in my life.

TABLE OF CONTENTS

LIST OF FIGURES

1. INTRODUCTION

One-dimensional (1D) nanostructures, such as various kinds of nanotubes, nanowires and nanoribbons, could possess unique thermophysical properties due to both classical and quantum confinement effects on phonons. Studying phonon transport through these 1D nanostructures is, therefore, of fundamental scientific significance. Moreover, the unique thermophysical properties could have important implications in thermal management of microelectronic and optoelectronic devices and in novel nanostructured thermoelectric energy converters. Not surprisingly, thermophysical properties of individual nanostructures have attracted great interest and intensive efforts have been devoted to related theoretical, numerical, and experimental studies in recent years. Experimental studies of thermophysical properties of 1D nanostructures pose many challenges related to sample preparation and accurate measurements. For thermal measurements, a sample is usually placed between a heat source and a heat sink, and one particularly challenging and unsolved issue is how to eliminate the effects of contact thermal resistance between the nanostructures and heat sources/sinks. This dissertation seeks to tackle this issue to extract intrinsic thermal conductivities of individual nanotubes and nanoribbons. In addition, this dissertation also explores thermal conductivity of boron carbide nanowires and contact thermal conductance between individual Multi-Walled Carbon Nanotubes. In the introduction section, we first briefly review the pioneering work that has been done in experimental studies of thermal transport through individual nanostructures and their contacts.

1.1 Phonon Transport in Nanowires

Experimental studies on phonon transport in nanowires were first initiated by Tighe *et al.* (Tighe, Worlock *et al.* 1997), who designed and fabricated a GaAs-based heterostructure composed of a rectangular semi-insulating intrinsic GaAs thermal reservoir (~3 μm^2) suspended above the substrate by four 5.5 μm long intrinsic GaAs beams (cross section ~200 nm × 300 nm). The four suspended beams constitute the thermal conductor of interest. The isolated reservoir is Joule heated by a source transducer patterned on top of it; and the generated heat is transferred to the substrate through the four monocrystalline intrinsic GaAs beams that suspend the isolated reservoir. A separate local sensing transducer on the isolated reservoir is used to measure an elevated reservoir temperature, arising in response to this heat input. This scheme allows direct measurement of the parallel thermal conductance (and thereafter effective mean free path) of the four nanoscale GaAs support beams at low temperature (< 6 K).

Using the Landauer formulation of transport theory, Rego and Kirczenow (Rego and Kirczenow 1998) predicted that dielectric quantum wires should exhibit quantized thermal conductance at low temperatures in a ballistic phonon regime. The quantum of thermal conductance is universal, independent of the characteristics of the material, and equals to $\pi^2 k_B^2 T/3h$, where k_B is the Boltzmann constant, h is the Planck's constant, and T is temperature. This quantized thermal conductance was later experimentally observed by Schwab *et al.* at very low temperature (< 1 K) (Schwab, Henriksen *et al.* 2000). They used a modified device similar to that of Tighe *et al.* (Tighe, Worlock *et al.* 1997), which includes a phonon 'cavity' (a quasi-isolated thermal reservoir) suspended by four phonon 'wave-guides'. One modification is that the material of the suspended structure was

changed from GaAs to silicon nitride with patterned Au resistors serving as the local heater and thermometer. More importantly, the shape of the waveguides was also modified to ensure ideal coupling between the suspended beams and thermal reservoirs to achieve a high phonon transmissivity at the contact region. Although this kind of devices can be used to study quantum transport of phonons in nanostructures at ultra-low temperature (< 6 K), there are limitations for them to be used for general studies of thermal transport in 1D nanostructures in a broad temperature range. First, it is difficult to use this device to measure various nanowires synthesized separately because in this set-up the samples have to also serve as the mechanical supporting beams. Second, since the beams as the sample constitute an essential part of the device, the materials must be non-conducting and able to be grown by epitaxy. Third, the beams are also used to support the central pads, and therefore, if the size of the nanoscale beam gets down to tens of nanometers, the mechanical strength might be an issue.

While a general thermophysical property measurement scheme remained an issue, huge success was achieved in nanowire synthesis targeting at various applications. Thermal transport properties of these nanowires stimulated the interest of theorists and some pioneering theoretical work was carried out by different groups. For example, Walkauskas *et al.* (Walkauskas, Broido *et al.* 1999) calculated the lattice thermal conductivity of free standing GaAs nanowires by solving the Boltzmann transport equation, which suggested that the nanowire thermal conductivity would be significantly lower than the bulk value because of enhanced surface phonon scattering. The thermal conductivity of silicon nanowires was investigated by Volz and Chen (Volz and Chen 1999) using molecular dynamics (MD) simulations. Their simulation results indicate that

for very small nanowires with square cross sections, the thermal conductivity could be about two orders of magnitude lower than those of bulk crystalline Si in a wide temperature range (200–500 K).

Inspired by the growing interest in thermal transport through nanowires, Li *et al.* (Li, Wu *et al.* 2003) measured the thermal conductivity of individual silicon nanowires using a microfabricated suspended device. As shown in **Figure 1.1**, an individual Si nanowire thermally connects two side-by-side silicon nitride (SiN_x) membranes each suspended by five SiN_x beams that are 420 μm long and 0.5 μm thick. A thin Pt resistance coil and a separate Pt electrode are patterned onto each membrane. Each resistor is electrically connected to four contact pads by the metal lines on the suspended beams, thus enabling four-point measurement of the resistance of the Pt coil. The Pt resistor can serve as a heater to increase the temperature of the suspended membrane, as well as a resistance thermometer to measure the temperature of each membrane. In the measurement, a bias voltage was applied to one of the resistors R_h, created Joule heating and increased the temperature, T_h, of the heating membrane above the thermal bath temperature T_0. Under steady state condition, part of the heat would flow through the nanowire to the other resistor R_s, and raised its temperature T_s. Based on the measured information, a heat transfer model of the whole system can be solved to extract the thermal conductance of the nanowire, under the assumption that the thermal resistance of the two contacts between the nanowire and the suspended membranes is much smaller than that of the nanowire. Furthermore, with the measured dimensions of the nanowire, its thermal conductivity can be derived.

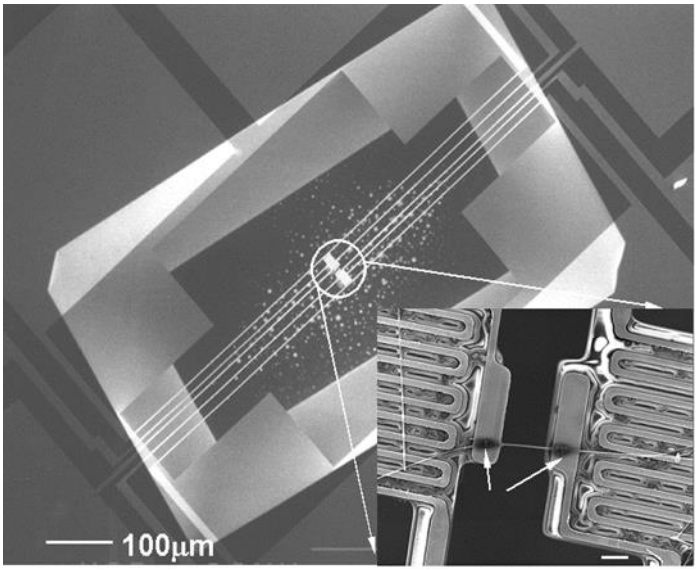

Figure 1.1 An SEM micrograph of the suspended microdevice (Li, Wu *et al.* 2003). The lower inset shows a 100 nm diameter Si nanowire bridging the two membranes, with wire-membrane junctions wrapped with amorphous carbon deposits (shown by arrows). The scale bar in the inset represents 2 μm.

Using this technique, thermal conductivities of individual 22, 37, 56, and 115 nm in diameter single crystalline Si nanowires prepared by vapor-liquid-solid method were measured. The measured thermal conductivities of Si nanowires are more than one order of magnitude lower than that of the bulk at room temperature, and the wire thermal conductivity reduces as the wire diameter decreases, as shown in **Figure 1.2(a)**. The results clearly indicate the effect of enhanced boundary scattering on phonon transport in Si nanowires. At low temperature, the thermal conductivity of the 22 nm diameter wire significantly deviates from the Debye T^3 law, as shown in **Figure 1.2(b)**, suggesting that, on this scale, effects other than phonon–boundary scattering may play an important role.

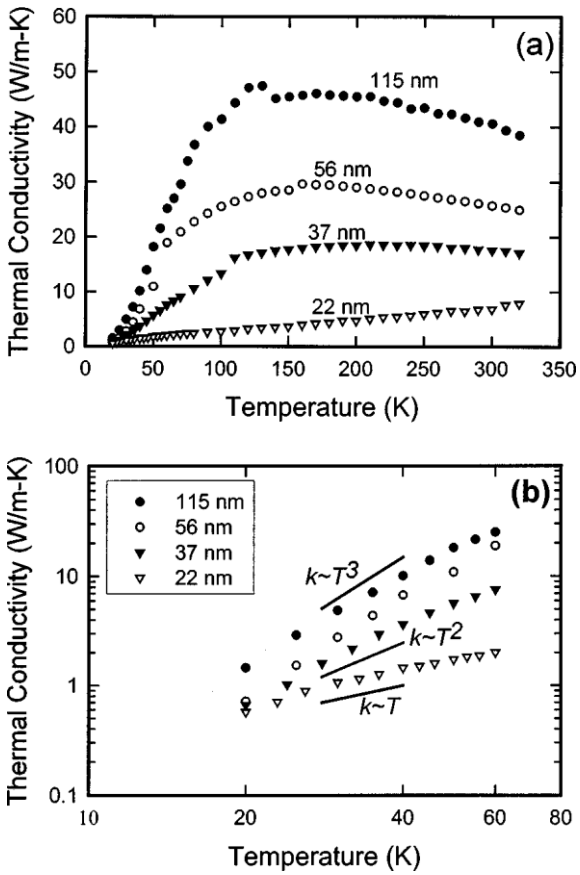

Figure 1.2 (a) Measured thermal conductivity of different diameter Si nanowires (Li, Wu *et al.* 2003). The number beside each curve denotes the corresponding wire diameter. **(b)** Low temperature experimental data on a logarithmic scale (Li, Wu *et al.* 2003). Also shown are T^3, T^2, and T^1 curves for comparison.

Using the same measurement method, Li *et al.* (Li, Wu *et al.* 2003) also measured thermal conductivities of individual 58 and 83 nm diameter single crystalline Si/SiGe superlattice nanowires. Comparison with the thermal conductivity data of intrinsic Si nanowires suggests that alloy scattering of phonons in the Si-Ge segments is the dominant scattering mechanism in these superlattice nanowires. However, boundary scattering also contributes to thermal conductivity reduction. Shi *et al.* (Shi, Hao *et al.*

2004) measured the thermal conductivities of a 53 nm thick and a 64 nm thick tin dioxide (SnO_2) nanobelt in the temperature range of 80–350 K using the same measurement method. The thermal conductivities of the nanobelts were found to be significantly lower than the bulk values due to the enhanced phonon-boundary scattering rate. They also measured the Seebeck coefficient (S), electrical conductivity (σ) and thermal conductivity (κ) of electrodeposited bismuth telluride (Bi_xTe_{1-x}) nanowire (Zhou, Jin *et al.* 2005). The results showed that the Seebeck coefficient (S) of the Bi_xTe_{1-x} nanowire can be either significantly higher or much lower than their bulk counterparts depending on the atomic ratio. The measured thermal conductivity (κ) indicated that below 300 K, phonon-boundary scattering overshadowed phonon-phonon Umklapp scattering in the nanowires. However, a monotonic decrease of κ with decreasing wire diameter d was not observed, likely due to different surface roughness of different nanowires. Chen *et al.* (Chen, Hochbaum *et al.* 2008) measured thermal conductance of individual single crystalline silicon nanowires with diameters less than 30 nm in the temperature range from 20 K to room temperature. The observed thermal conductance shows unusual linear temperature dependence at low temperature, consistent with the observation of Li *et al.* for the 22 nm silicon nanowire (Li, Wu *et al.* 2003). Hochbaum *et al.* (Hochbaum, Chen *et al.* 2008) further measured the thermal conductivity of silicon nanowires with rough surfaces and found that compared with bulk Si, nanowires with diameters of about 50 nm exhibited ~100-fold reduction in thermal conductivity, while maintained similar Seebeck coefficient and electrical conductivity as doped bulk Si, thus yielding a thermoelectric figure of merit ZT = 0.6 at room temperature. Boukai *et al.* (Boukai, Bunimovich *et al.* 2008) reported that due to reduced thermal conductivities, silicon nanowires of cross-

sectional areas of 10 nm × 20 nm and 20 nm × 20 nm could achieve ZT values of approximately 100-fold higher than that of bulk Si over a broad temperature range, including ZT ≈ 1 at 200 K.

1.2 Phonon Transport in Nanotubes

Unlike nanowires, in which enhanced phonon-boundary scattering tends to reduce the thermal conductivity, nanotubes, including carbon nanotubes (CNTs) and boron nitride (BN) nanotubes, are expected to be extremely good thermal conductor due to their unique structure which almost excludes boundary scattering effect. Using molecular dynamics simulations, Berber *et al.* (Berber, Kwon *et al.* 2000) predicted a thermal conductivity of an isolated (10, 10) nanotube as high as 6600 W m^{-1} K^{-1} at room temperature, which is the highest thermal conductivity of any known materials in the world.

Because of the challenges of handling individual CNTs for thermophysical property measurements, the specific heat, thermal conductivity and thermal power (TEP) of millimeter-sized mats of CNTs were first measured by several groups (Kim, Shi *et al.* 2001). Even though these measurements answered some questions related to thermophysical properties of CNTs, issues related to tube heterogeneity and contacts between CNTs prevented researchers from acquiring intrinsic properties of CNTs. One problem is that all these measurements yield the average value of a number of different CNTs in a "bulk" sample, which makes the results more qualitative than quantitative. In addition, since there are numerous tube-tube junctions in these CNT mats, it is difficult to extract intrinsic values of the thermal properties. In fact, these junctions are believed to

pose dominant resistance to thermal transport in the "bulk" CNT mats (Kim, Shi *et al.* 2001).

The first experimental study of thermal transport through individual multi-walled carbon nanotubes (MWCNT) was conducted by Kim *et al.* (Kim, Shi *et al.* 2001). They developed a microfabricated suspended device with an integrated MWCNT to measure thermal transport through the tube free from contacts within tube bundles. Their results showed that the thermal conductivity of an individual 14 nm-diameter MWCNT is more than 3000 W m^{-1} K^{-1} at room temperature, which is one order of magnitude higher than the value from previous experiments with macroscopic mat samples. Brown *et al.* (Brown, Hao *et al.* 2005) used a temperature sensitive scanned microscope probe to measure the thermal and electrical conductance of protruding individual MWCNTs from the ends of MWCNT bundles, which demonstrated both ballistic phonon and electron transport in MWCNTs. Later, experimental results of Yu *et al.* (Yu, Shi *et al.* 2005) indicated that the thermal conductance of a 2.76 μm-long individual suspended single-wall carbon nanotube (SWCNT) was very close to the calculated ballistic thermal conductance of a 1 nm-diameter SWCNT without showing signatures of phonon-phonon Umklapp scattering in the temperature range from 110 to 300 K. Pop *et al.* (Pop, Mann *et al.* 2006) extracted the thermal conductivity of an individual SWCNT over the temperature range of 300-800 K from high-bias (V > 0.3 V) electrical measurements by inverse fitting using an existing electrothermal transport model, as seen in **Figure 1.3**.

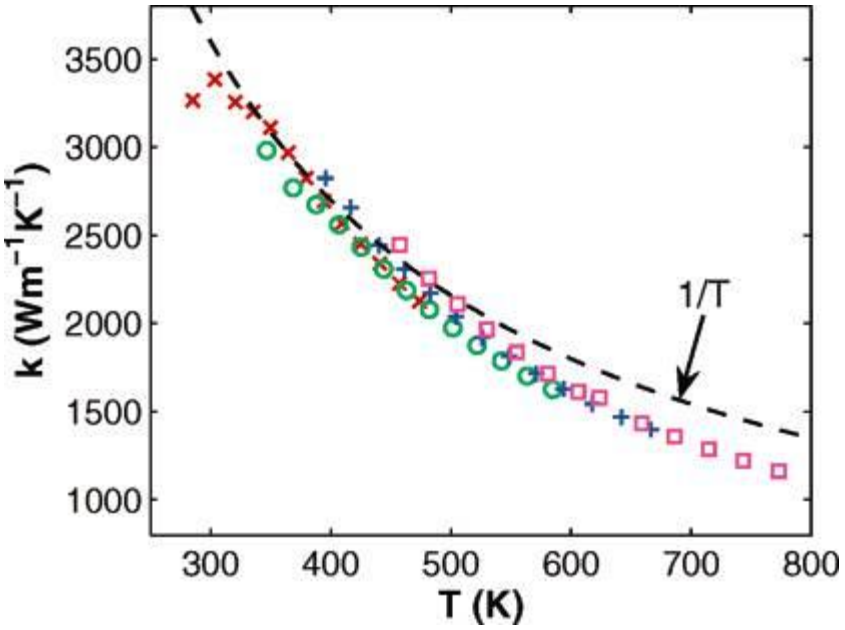

Figure 1.3 Extracted values of the thermal conductivity of a SWCNT vs the average tube temperature from fitting the high bias *I-V* data (Pop, Mann *et al.* 2006).

Fujii *et al.* (Fujii, Zhang *et al.* 2005) measured the thermal conductivity of MWCNTs using a suspended sample-attached T-type nanosensor. They found that the thermal conductivity of CNTs at room temperature increases as the tube diameter decreases, which indicates the enhanced phonon scattering rates as the tube diameter increases. For a CNT with a diameter of 9.8 nm, the measured thermal conductivity is 2069 W m^{-1} K^{-1} and the measured thermal conductivity for a CNT of 16.1 nm-diameter increases with temperature and appears to have an asymptote near 320 K. Chiu *et al.* (Chiu, Deshpande *et al.* 2005) deduced the thermal conductivity of a free-standing MWCNT with a diameter of 10 nm as 600 W m^{-1} K^{-1} by linearly fitting measured electrical breakdown power P and the inverse of the suspended length L^{-1} of different MWCNT lengths. Choi *et al.* (Choi, Poulikakos *et al.* 2006) used a four-point 3ω method

to measure the thermal conductivity of individual MWCNTs, and the measured room temperature value was 300 ± 20 W m^{-1} K^{-1}. The lower values of the MWCNT thermal conductivity are most probably from the low quality of the MWCNTs synthesized with chemical vapor deposition method, which tend to have bonding and structural defects that scatter phonons. The MWCNT samples with high thermal conductivities are mostly from the arc-discharge method, which yield high quality tubes with much less defects.

For thermal conduction through CNTs, two questions are of great interest. First, how high is the ballistic lattice thermal conductance? Second, how long a CNT can be in which phonon transport remains ballistic? Mingo and Broido (Mingo and Broido 2005) answered these two questions by calculating upper bounds of the lattice thermal conductance of SWCNTs, graphene, and graphite, showing phonon transport in CNTs with very long ballistic lengths (on the order of micron long below room temperature). The calculated theoretical ballistic conductance of graphite agreed reasonably well with the experimental results of MWCNTs below 200 K by a factor of 0.4, suggesting that MWCNTs and graphite are very similar in their thermal conduction mechanism below 200 K.

1.3 Contact thermal resistance

The idea that a thermal resistance might exist between liquid helium and a solid was first expressed as early as 1936 by Kurti *et al.* (Kurti, Rollin *et al.* 1936). They assumed that such a thermal resistance to be small and therefore ignored it. A few months later, Keesom *et al.* recognized that the thermal resistance at the interface was “relatively very considerable”, but they too allowed the idea to pass without further investigation

(Keesom and Keesom 1936). In 1941, Kapitza reported his measurements of the temperature drop near the boundary between helium and a solid when heat flowed across the boundary, and the related thermal resistance at the boundary is later called Kapitza resistance (Swartz and Pohl 1989). In the presence of a heat flux J (W m^{-2}) across the boundary, this thermal resistance causes a temperature discontinuity ΔT at the boundary, and the thermal boundary resistance (TBR) is defined as $R_k = \Delta T/J$.

The idea that an interface should produce a thermal resistance is intuitively appealing, since an interface constitutes an interruption in the regular crystalline lattice on which phonons propagate. For an interface between dissimilar materials, the different densities and sound speeds result in a mismatch in the acoustic impedances, which is directly analogous to the mismatch in the refractive indices of two optically different materials. Based on this analogy, the effects that this impedance mismatch has on phonon transmission could be captured by an acoustic-mismatch model (AMM). Assuming that no scattering takes place at the interface, and by imposing appropriate stress and displacement boundary conditions at the interface, the AMM gives a transmission coefficient t_{AB} for phonon energy in material *A* incident normally upon the interface with material *B* as:

$$t_{AB} = \frac{4Z_A Z_B}{(Z_A + Z_B)^2}, \tag{1.1}$$

where $Z = \rho c$ is the acoustic impedance, with c and ρ being the speed of sound and mass density, respectively. In AMM, the interface has no intrinsic properties but merely joins the two grains, and the fraction of energy transmitted through the interface is independent of the structure of the interface itself (Cahill, Ford *et al.* 2003). By contrast, a diffuse mismatch model (DMM) assumes that all phonons striking an interface lose memory of

where they come from, and the probability of the phonons being diffusely scattered into one side of the interface or the other is simply proportional to the phonon density of states.

For most reported experimental studies of thermal conductance of nanowires or nanotubes, the derived thermal conductivity is an effective one, including the contribution from the contact thermal resistance between the nanowires/nanotubes and the heat source/sink. If the contact thermal resistance is not negligible, then the intrinsic thermal conductivity of the measured nanowires or nanotubes should be higher. This issue has been realized and efforts have been made by several groups to quantify the contact thermal resistance between individual nanowires/nanotubes and the substrate surface, aiming at extraction of the intrinsic thermophysical properties of nanowires/tubes.

For example, scanning thermal microscopy (SThM) has been used to study the contact thermal resistance. A scanning thermal microscope operates by bringing a sharp temperature-sensitive tip in close proximity to a sample solid surface (see **Figure 1.4**). Localized heat transfer between the tip and the sample surface changes the tip temperature, which can be detected by various mechanisms. By scanning the tip across the sample surface, a spatial map of the tip-sample heat transfer can be constructed. The SThM can operates in two modes - if the tip comes into local equilibrium with the sample, one obtains the spatial temperature distribution of the sample surface, whereas if the temperature change is determined for a known heat flux, one could obtain the local thermal properties (Cahill, Ford *et al.* 2003).

In Kim *et al.*'s (Kim, Shi *et al.* 2001) measurement of the thermal conductivity of individual MWCNTs, they estimated a contact thermal conductance ~5×10^{-7} W K^{-1} for a contact length ~1 μm at room temperature by a separate study of scanning thermal

microscopy (SThM) on a self-heated MWCNT. While the total measured thermal conductance is 1.6×10^{-7} W K^{-1} and therefore they claimed that the intrinsic thermal conductance of the tube was the major part of measured thermal conductance. Since the estimation was based on an indirect measurement of a different MWCNT samples and because of the resolution limit of scanning thermal microscopy, quantitatively determining the contact thermal resistance has remained an issue.

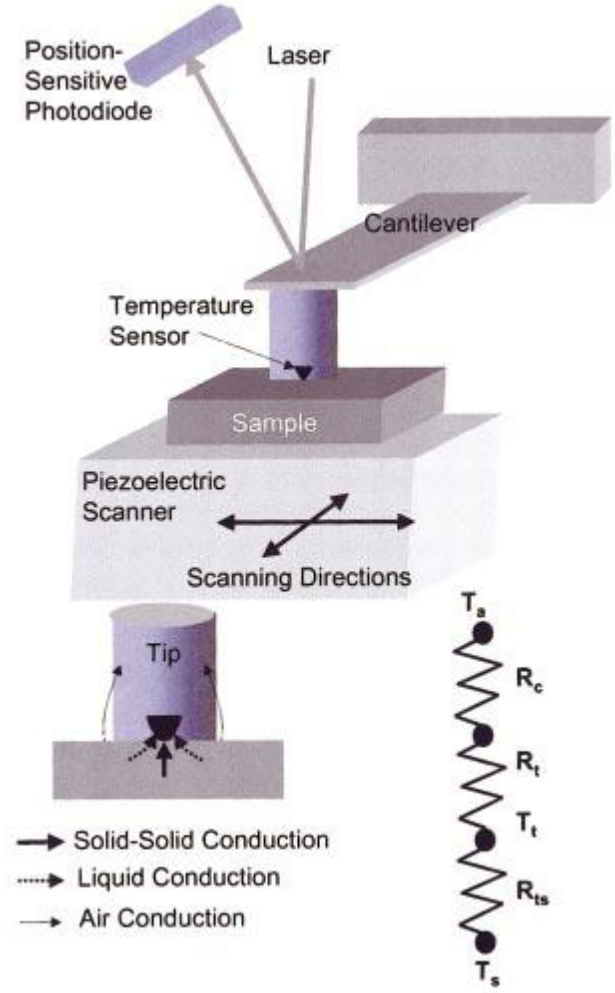

Figure 1.4 Schematic diagram of a scanning thermal microscope, which consists of a sharp temperature-sensitive tip mounted on a cantilever probe (Cahill, Ford *et al.* 2003). The sample is scanned in the lateral directions while the cantilever deflections are

monitored using a laser beam-deflection technique. Topographical and thermal images can be obtained simultaneously. The thermal transport at the tip-sample contacts consists of air, liquid, and solid–solid conduction pathways. A simple thermal resistance network model of the sample and probe combination, shows that when the sample is at temperature T_s , the tip temperature T_t depends on the values of the thermal resistances of the tip-sample contact, R_{ts} , the tip, R_t , and the cantilever probe, R_c.

To avoid the thermal contact resistance problem, Li *et al.* (Li, Liu *et al.* 2009) used a non-contact Raman spectra shift method to measure the intrinsic thermal conductivity of individual single-walled and multi-walled CNTs. In their method, the CNT was suspended over a trench and heated electrically, as shown in **Figure 1.5**. The temperature difference between the middle and the two ends of the CNT was determined by the temperature-induced shifts of its G band Raman spectra. By assuming that the two ends of the suspended CNT have the same temperature and the temperature at the middle point is the highest, the intrinsic thermal conductivity of the CNT was derived as

$$\kappa = \frac{P_{heat} L}{4S \times (T_h - T_l)}, \tag{1.2}$$

where P_{heat} is the heating power generated on the suspended CNT, L is half length of the suspended section, S is the cross-sectional area of the CNT, and T_h and T_l are the temperatures of the middle point and the two ends of suspended section of the CNT, respectively.

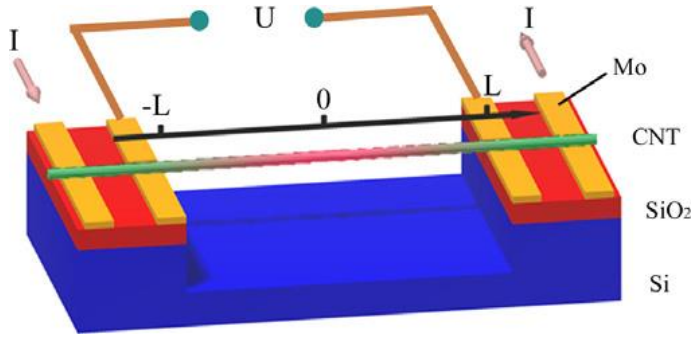

Figure 1.5 A schematic of an individual suspended CNT that is self-heated electrically (Li, Liu *et al.* 2009). A coordinate was constructed for the suspended section. The zero point is at the middle and *L* is the half length of the suspended CNT.

Based on the linear relationship between Raman shift and temperature of the CNT, T_h-T_l in Eq. (1.2) can be obtained, thus the thermal conductivity of the CNT can be derived. However, there are several problems need to be addressed in this method. First of all, the legitimacy of linear relationship between the observed Raman spectra shift and the temperature of the CNT needs to be confirmed with more experiments. From the noisy experimental data of G band frequency of an individual CNT at different temperatures, it's difficult to exclude some non-linear fitting functions other than the linear relation. Secondly, the temperature distribution along the CNT which assumes same temperature at the two ends and highest temperature at the middle point, needs further confirmation.

Efforts to eliminate the contact thermal resistance were also made by Hippalgaonkar *et al.* (Hippalgaonkar, Huang *et al.* 2010). They modified the fabrication process of the suspended microdevice developed by Shi and coworkers (Shi, Li *et al.* 2003) to further integrate with fabricated silicon nanowires having rectangular cross

sections to measure their thermal conductivities. A linear fit of the measured thermal resistance of fabricated silicon nanowires with identical cross sections and different lengths showed that the residual conductance at L=0 is negligible (see in **Figure 1.6**), indicating that the monolithic contact within the device layer eliminates the contact resistance between the nanowires and the measurement device. However, the fabrication process of this integrated microdevice is quite complex involving multiple lithography and etching steps, which might affect the properties of the measurement sample. In addition, this method is also difficult to modify to measure 1D nanomaterials other than silicon based structures.

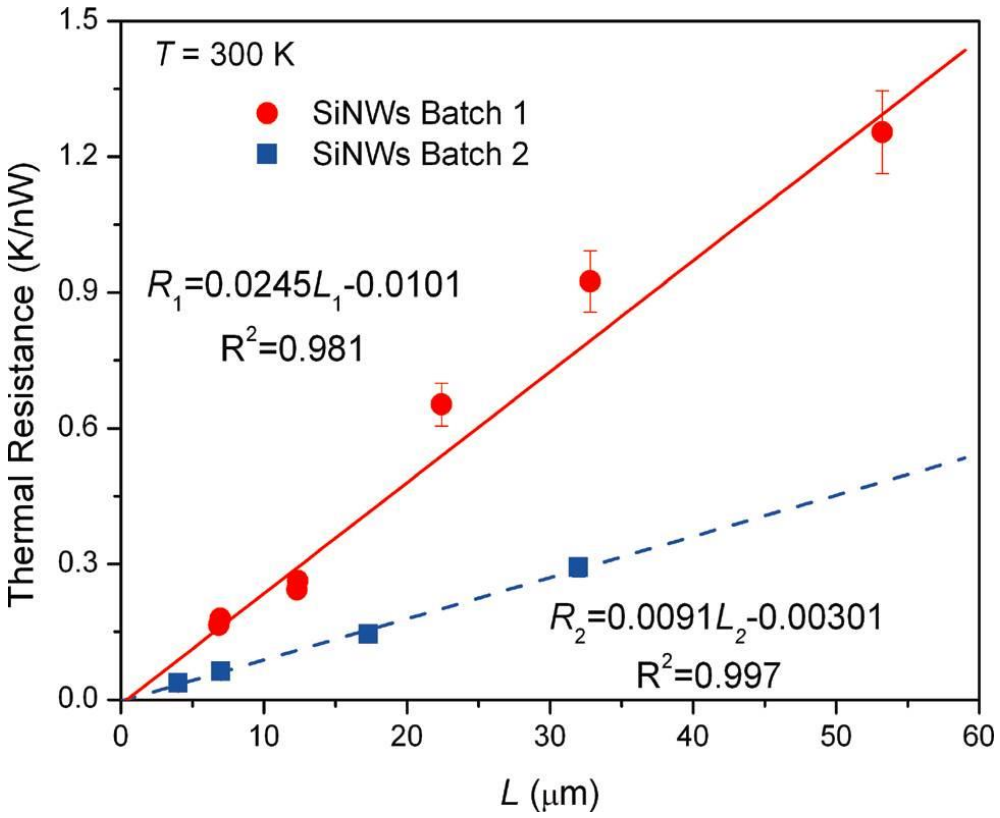

Figure 1.6 Plot of the thermal resistance (K/nW) as a function of nanowire length (3 μm up to 50 μm) for batch 1 (circles) and batch 2 (triangles) (Hippalgaonkar, Huang *et al.*

2010). The linear fit passes very close to the origin indicating nearly zero contact resistance. Error bars are included for all points.

Mavrokefalos *et al.*(Mavrokefalos, Nguyen *et al.* 2007; Mavrokefalos, Pettes *et al.* 2007) developed a four-probe thermal measurement scheme, which use the nanostructure sample itself as a differential thermocouple to determine the temperature drops at the contacts and thus quantify the contact thermal resistance, as shown in **Figure 1.7**. This method is limited to samples which have relatively high Seebeck coefficient.

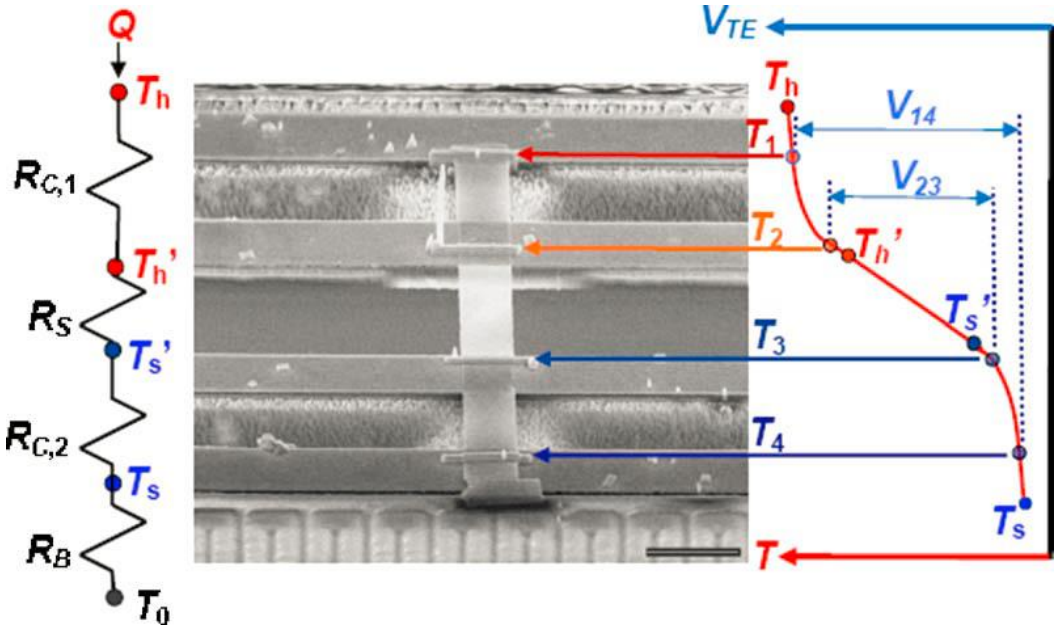

Figure 1.7 A schematic diagram of four-probe thermal measurement methods (Mavrokefalos, Pettes *et al.* 2007). T_h and T_s are the temperatures of the heating (upper) and sensing (lower) membranes, respectively. T_1, T_2, T_3, and T_4 are the temperatures at the four Pt contacts deposited on the nanofilm. T_0 is the temperature of the substrate. R_S and R_B are the thermal resistances of the nanofilm and the six beams supporting one membrane, respectively. $R_{C,1}$ and $R_{C,2}$ are the contact thermal resistances between the

nanofilm and the heating and sensing membranes, respectively. V_{14} and V_{23} are the thermoelectric voltage (V_{TE}) measured between the two outer electrodes and that between the two inner electrodes, respectively. The scale bar in the SEM image is 2 μm.

1.4 Summary

The pioneering studies of thermal transport in 1D nanostructures have led to a better understanding of nanoscale thermal transport. However, there are still lots of puzzles on thermal transport through nanostructures and their contacts that need to be solved. In the following chapters of this dissertation, we modify and develop several new measurement methods based on the versatile suspend device measurement platform to address some of these puzzles.

In Chapter 2, the measurement principle, including device fabrication, sample preparation, electrical measurement setup, measurement error and uncertainty will be introduced and discussed.

Contact thermal resistance remains an important and challenging issue in determining the intrinsic thermal conductivity in almost all steady-state heat flow and electrical measurement methods. In order to address this long-standing issue, we develop a measurement method based on the suspended device to extract the intrinsic thermal conductivity of MWCNTs and silicon nanoribbons through multiple measurements of the same MWCNT and silicon nanoribbon samples with different lengths of suspended segments between the heat source and the heat sink. With this new method, intrinsic

thermal conductivity of most 1D nanostructures can be determined. These will be discussed in Chapter 3 and 4.

Utilizing the same measurement platform and taking advantage of etch-through suspended microdevice, we are able to perform property-structure characterization on individual boron carbide nanowires. This part is covered in Chapter 5.

By measuring the thermal conductance of two CNTs with a contact and individual CNTs separately, contact thermal conductance between bare MWCNTs and tubes with humic acid coating was extracted and some novel thermal transport mechanism in the cross-plane direction of graphite was revealed. Chapter 6 will focus on this part.

Chapter 7 will summarize the research results and discuss some future directions on thermal transport through individual nanostructures and their contacts.

2. DEVICE FABRICATION AND MEASUREMENT SETUP

2.1 Introduction

To measure the thermal conductivity of thin films, several different steady-state and transient techniques have been developed, such as the 3ω method and the thermoreflectance method (Mirmira and Fletcher 1998). Generally, a thin film sample is heated by Joule heating of a thin metal line or laser to create a temperature gradient. By monitoring the temperature or reflectivity change of the probing element and based on the heat transfer model of measurement samples, the thermal conductivity of the thin film can be extracted. However, conventional techniques for thin film thermal property measurement, cannot be readily extended to 1D nanostructures due to the small sample size. Shi and coworkers developed a suspended microdevice for measuring thermal conductivity and thermoelectric properties of individual 1-D nanostructures (Shi, Li *et al.* 2003). This chapter describes the design and fabrication of this type of device and the associated experimental techniques for measuring the same sample with different lengths between the heat source and heat sink.

2.2 Device Fabrication

Figure 2.1 shows a Scanning Electron Microscopy (SEM) image of the microdevice, which consists of two adjacent 18.2 μm × 27.1 μm low stress silicon nitride (SiN_x) membranes suspended with six 0.5 μm thick, 415.9 μm long and 2.2 μm wide SiN_x beams. There is one platinum resistance thermometer (PRT) composed of 30 nm

thick and 500 nm wide platinum line on each SiN_x membrane. To prevent electrically conductive sample from shorting the heater coils and hence disturbing the measurement circuits, the PRT area is covered by 200 nm thick low temperature silicon oxide (LTO) layer. The PRT is connected to 400 μm × 500 μm platinum contact pads located on the substrate via 1.2 μm wide platinum leads on the long SiN_x beams. For simultaneous measurements of electrical transport properties, one or two additional platinum electrodes can be fabricated on the edge of each SiN_x membrane, allowing for measurements of electrical conductivities and Seebeck coefficients.

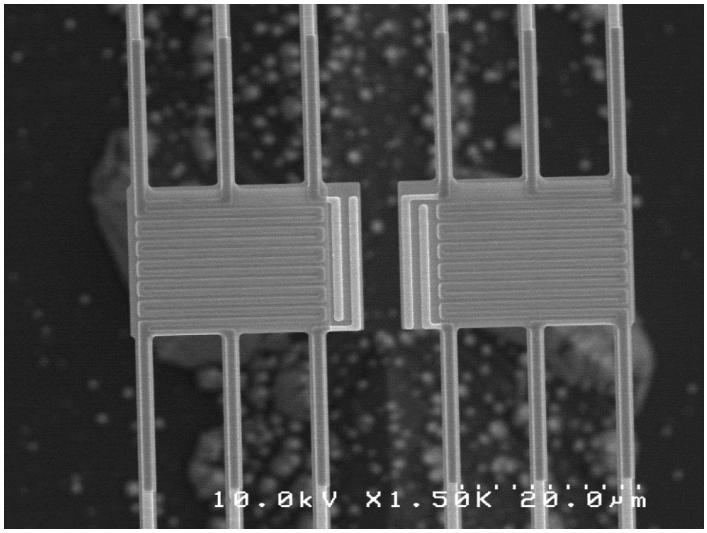

Figure 2.1 Scanning Electron Microscopy (SEM) micrograph of the two suspended membranes with electrical and temperature sensors.

The device is batch-fabricated using a wafer-scale microfabrication process, as shown in **Figure 2.2**. The fabrication process begins with deposition of a 0.5 μm thick low stress SiN_x film on both sides of a 4″ (100 mm) diameter Si wafer using low pressure chemical vapor deposition (LPCVD). A 30 nm thick Pt film is then coated on the SiN_x

film by radio frequency (RF) sputtering. The Pt film is patterned by standard photolithography process using a GCA Autostep 200 DSW i-line wafer stepper and etched using ion milling. During the lithography step, the photoresist is cured by UV photoresist stablizer before ion milling to facilitate photoresist removal after ion milling. After stripping the photoresist, a 200 nm thick low temperature silicon dioxide (LTO) film is deposited on the patterned Pt layer by plasma enhanced chemical vapor deposition (PECVD). The LTO and low stress SiNx films are then patterned by photolithography and etched by reactive ion etching (RIE), after which the photoresist is stripped. The microfabrication process is completed with etching of the Si substrate with 10% tetramethylammonium hydroxide (TMAH) using the patterned SiN_x as a mask.

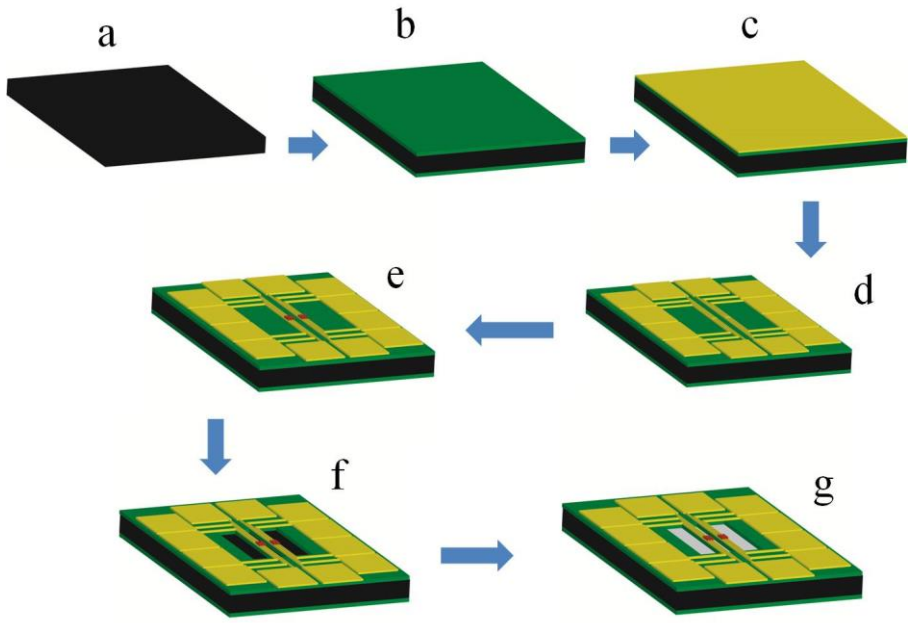

Figure 2.2 Schematic of the suspended microdevice fabrication process. (a) bare silicon wafer, (b) LPCVD deposition of 0.5 μm low stress silicon nitride (SiN_x) on both sides of the wafer, (c) sputtering coat of 30 nm platinum layer, (d) patterning of platinum layer, (e)

PECVD deposition of 200 nm LTO and patterning, (f) SiN_x layer patterning, (g) silicon substrate wet etch by TMAH.

For Si surface with (100) orientation, the etch rate of 10% TMAH at 70 °C is around 0.41 μm/min (Hull 1999), 4–5 hours of etch will remove about ~120 μm thick Si substrate. However, longer than 5 hours etching could cause damage to the long platinum leads on the SiN_x beam, which could begin to be stripped off, as can be seen in **Figure 2.3**. Using this wafer-scale microfabrication process, about 1000 densely packed suspended microdevices can be made on a 100 mm diameter wafer.

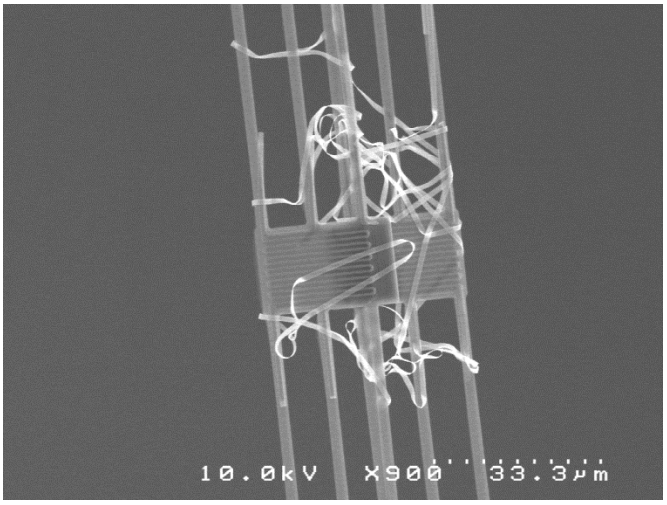

Figure 2.3 Thin platinum leads (white ribbon in the image) are stripped off from the SiN_x beams after long time TMAH etch.

As the Si substrate under the suspended SiN_x membranes is not completely etched away, it blocks electron transmission and makes transmission electron microscopy (TEM) examination of the 1D nanostructure samples on the device impossible. Besides, the standard device made from 500 μm thick Si wafer is normally too thick to insert into the

TEM sample holder. For example, for a Gatan double tilt TEM sample holder (**Figure 2.4**), a device thickness less than 200 μm is required. To overcome these limits and obtain etch-through device to conduct TEM study on measured nanostructures, several more steps can be adopted. First, when patterning the LTO layer, instead of just leaving LTO to cover the PRT part, all the suspended part is covered. The LTO layer will protect all Pt patterns from being stripped after long time TMAH etch, as discussed before. After patterning the SiN_x film, the backside low stress nitride film is completely removed by RIE. The whole wafer is then clamped in a single side etch chuck to expose only the backside of the wafer and sit in 25% KOH solution at 80 °C for about 100 min. This will etch away ~100 μm thick backside silicon layer. After that, remove the single side etch chuck and sit the wafer in 22% TMAH solution at 90 °C for about 5–6 hours to etch through the center window of the device. This step also thins down the device thickness below 200 μm. A final step vapor HF etching is applied to remove the LTO layer. **Figure 2.5** shows a SEM micrograph of an as-fabricated etch-through device.

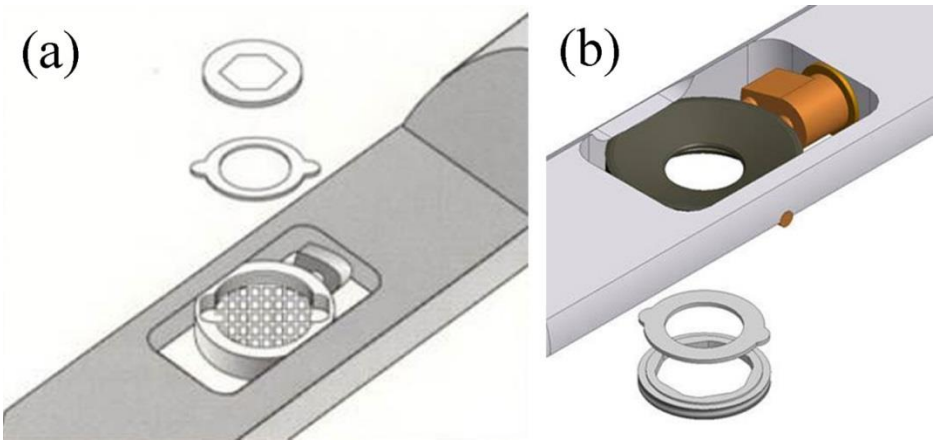

Figure 2.4 Schematic of front and back side view of the Gatan double tilt TEM sample holder. **(a)** front side view **(b)** back side view

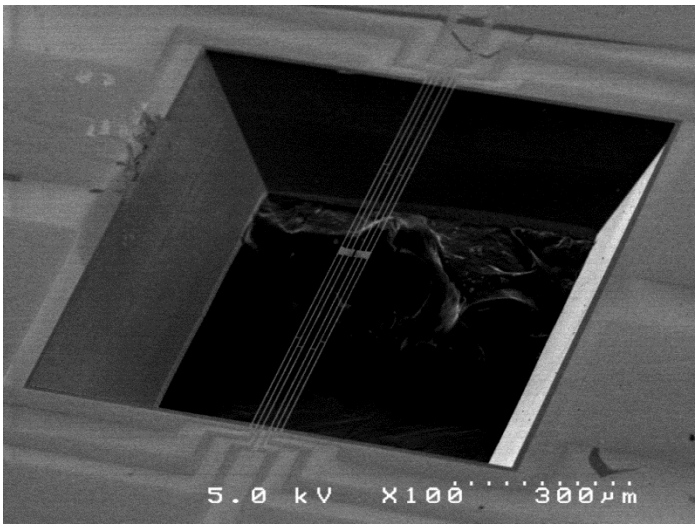

Figure 2.5 An SEM micrograph of a fabricated etch-through measurement device.

For intrinsic thermal conductivity measurement, the length of the nanotubes and nanowires between the two suspended membranes need to be varied; and therefore, devices with different distances (2, 3, 4 and 6 μm) between the two suspended membranes are fabricated, as shown in **Figure 2.6**.

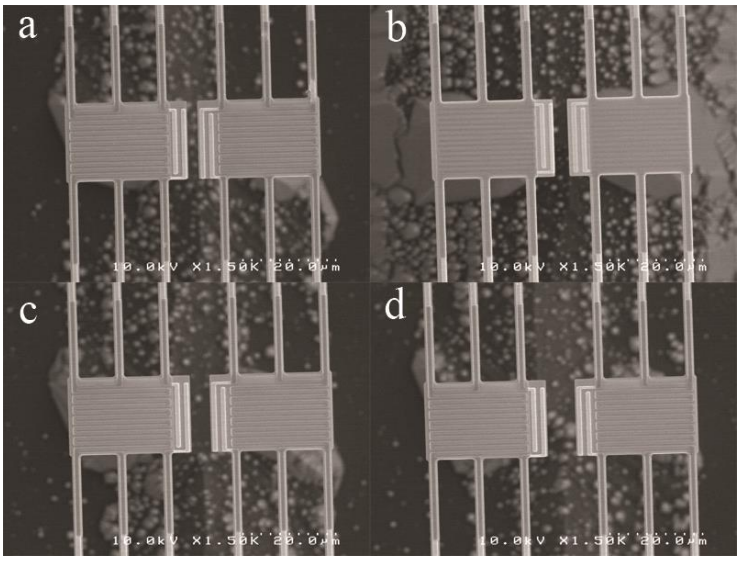

Figure 2.6 Suspended microdevices with different distance D between two suspended membranes. **(a)** D = 2 μm, **(b)** D = 3 μm, **(c)** D = 4 μm, **(d)** D = 6 μm.

The fabricated suspended devices can be used for not only thermal conductivity measurement, but also other important transport properties (Seebeck coefficient, electrical conductivity) measurement. To achieve these capabilities, either one or two additional platinum electrodes are patterned on the edge of each SiN_x membrane, as shown in **Figure 2.7**. Devices with one wide platinum electrode on each membrane are fabricated specifically for thermal conductivity measurement. Wide, flat platinum membranes provide good thermal contacts with nanotubes and nanowires, ensuring constant contact thermal resistance between samples and suspended membranes, as discussed in details later. On the other hand, devices with two platinum probes on each membrane are used to realize four-probe electrical resistance measurement.

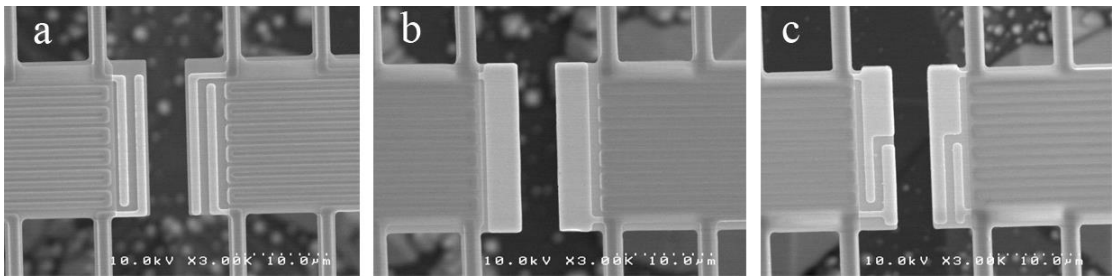

Figure 2.7 SEM micrograph of suspended microdevices of different designs. **(a)** a microdevice with 4 platinum electrodes, **(b)** a microdevice with 2 wide platinum electrodes, and **(c)** a microdevice with partial 4 platinum electrodes and partial 2 platinum electrodes.

2.3 Sample Preparation

For measurement of thermophysical properties with the above-described device, a crucial step is to place individual 1D nanostructures between the two suspended

membranes. To do so, an in-house assembled micromanipulator, as shown in **Figure 2.8**, has been used to manipulate the samples and place them at the desired locations.

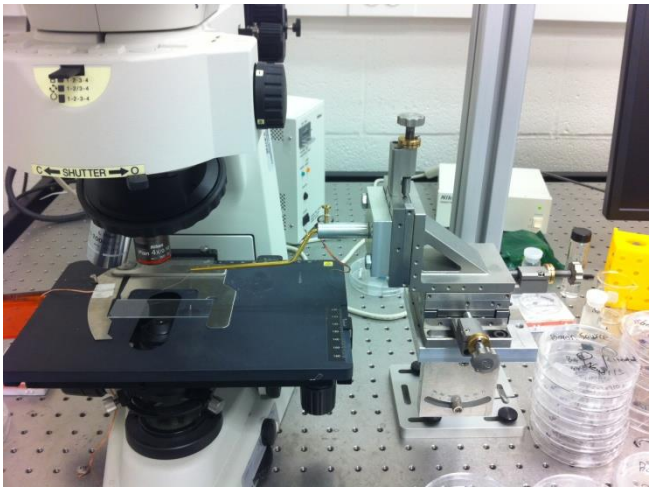

Figure 2.8 A photo of the in-house assembled micromanipulator with a Nikon microscope used to place the individual nanostructure at desired locations.

The sample placement process usually includes two steps. First, 1D nanostructures, such as CNTs and various nanowires/ribbons, are dispersed in solutions such as reagent alcohol or isoproponal alcohol (IPA) to form a suspension. A few drops of the suspension are casted on a piece of polydimethylsiloxane (PDMS). After the solvent was evaporated, we can find many individual 1-D nanostructures at the edges of the PDMS. In addition, some nanowires or nanotubes grown or fabricated on a chip can also be directly transferred to the elastomeric PDMS piece through stamping, as shown in **Figure 2.9**.

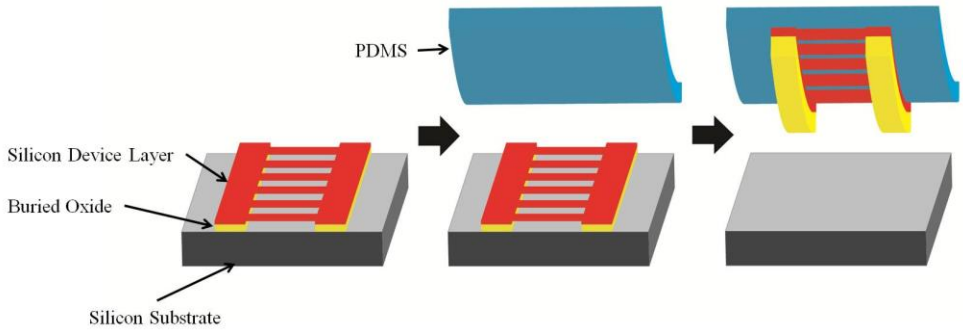

Figure 2.9 Schematic showing fabricated silicon nanoribbons transferred from SOI wafer to a piece of PDMS through a stamping process.

The second step is to use a sharp probe with a tip radius of ~0.1 μm mounted on the micromanipulator to pick up a single nanotube, nanowire or nanoribbon from the PDMS and place it between the two suspended membranes, as shown in **Figure 2.10**. The whole process is performed under a 100×, long working distance (6.5 mm) objective lens mounted on a Nikon optical microscope.

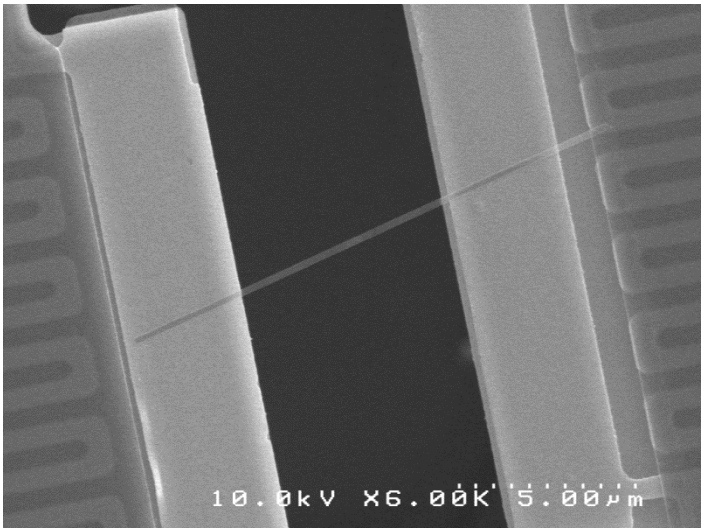

Figure 2.10 An SEM micrograph showing an individual silicon nanoribbon bridging two suspended membranes.

To improve the thermal and electrical contact between the sample and the membranes, electron beam induced deposition (EBID) technique can be used to locally deposit gold or platinum to increase the contact area between the 1D nanostructure and the suspended membrane, as shown in **Figure 2.11**.

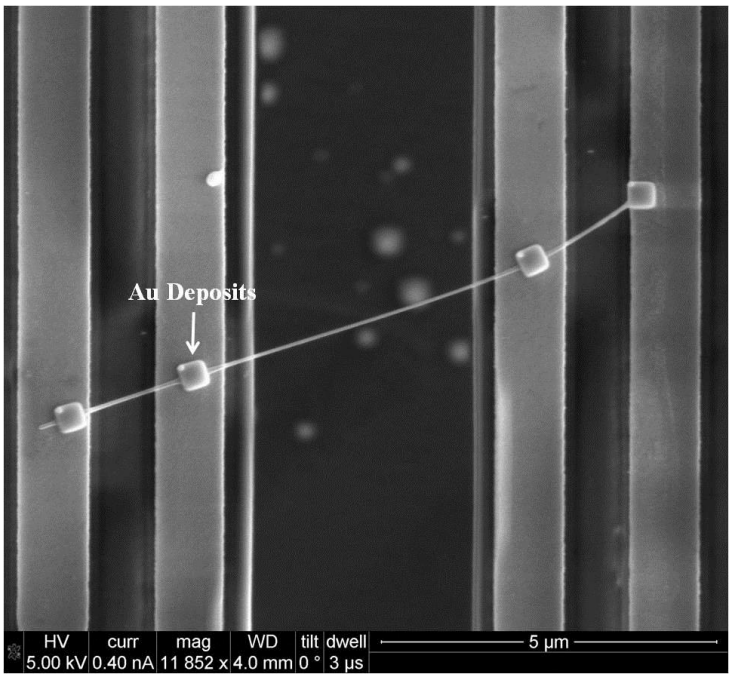

Figure 2.11 An SEM micrograph of a boron carbide nanowire bridging the four electrodes on the microdevice with EBID local deposition of Au at the contact.

2.4 Measurement Setup

Figure 2.12 shows the schematic diagram of the measurement setup. The suspended microdevice with a 1D nanostructure is placed in a cryostat with a vacuum level below 10^{-6} Torr. Two lock-in amplifiers (Stanford Research SR850) are used to measure the voltage change of the PRTs on the heating and sensing side, respectively. A small sinusoidal ac signal from the lock-in amplifier on the heating side is coupled with a

DC heating current source through an integrated differential amplifier (Analog Devices SSM2141). Two resistors with large resistances (500 kΩ on the heating side and 1 MΩ on the sensing side) are connected into the circuit to achieve constant current condition under each designated DC heating voltage.

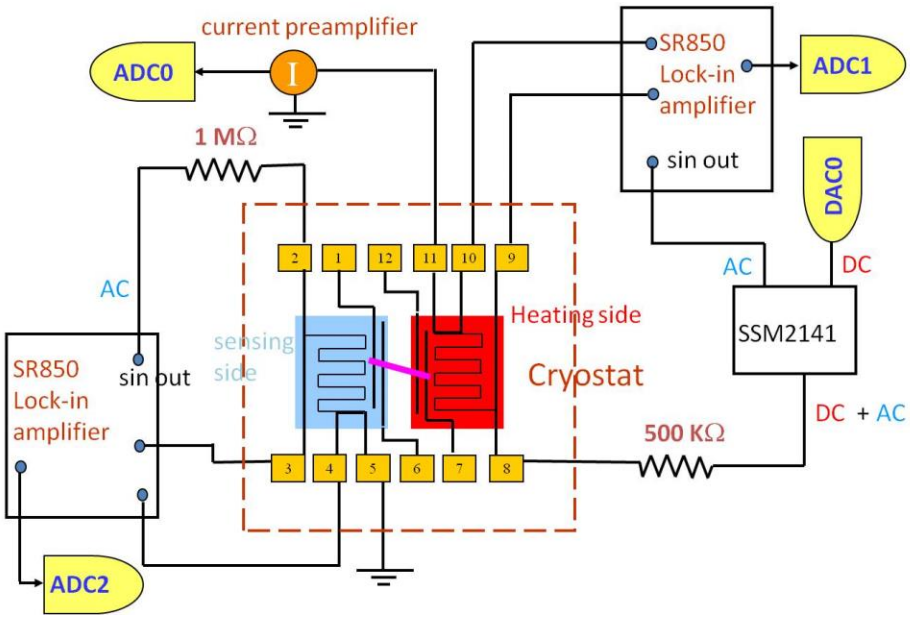

Figure 2.12 A schematic diagram of the measurement setup.

Figure 2.13 shows the thermal circuit of the measurement setup. The two suspended membranes are denoted as the heating membrane and the sensing membrane, respectively. A dc current (I) passes through the PRT on the heating membrane. As a result, a certain amount of Joule heat, $Q_h = I^2R_h$, is generated in this heating PRT, where R_h is the PRT's electrical resistance. The PRT on each membrane is connected to the contact pads by four Pt leads, allowing for four-probe resistance measurement. The resistance of each Pt lead is R_L, which is about half of R_h. Therefore, Joule heat of $2Q_L = 2I^2R_L$ is dissipated in the two Pt leads that supply the dc current to the heating PRT. The

temperature of the heating membrane can be assumed to increase to a uniform temperature T_h, which is justified by the fact that the internal thermal resistance of the heating membrane is much smaller than the thermal resistance of the long narrow beams thermally connecting the membrane to the silicon chip at temperature T_0. A certain amount of heat Q_2 is conducted through the sample from the heating membrane to the sensing one, raising the temperature of the latter to T_s. In vacuum and with a small ΔT_h ($\Delta T_h = T_h - T_0 < 5K$), heat transfer between the two membranes by residual air conduction/convection and thermal radiation is negligible compared to Q_2. The heat transfer through the sample, Q_2, is further conducted to the substrate (silicon chip) through the six beams supporting the sensing membrane. The rest of the heat, i.e. $Q_1 = Q_h + 2Q_L - Q_2$, is conducted to the environment through the other six beams connected to the heating membrane.

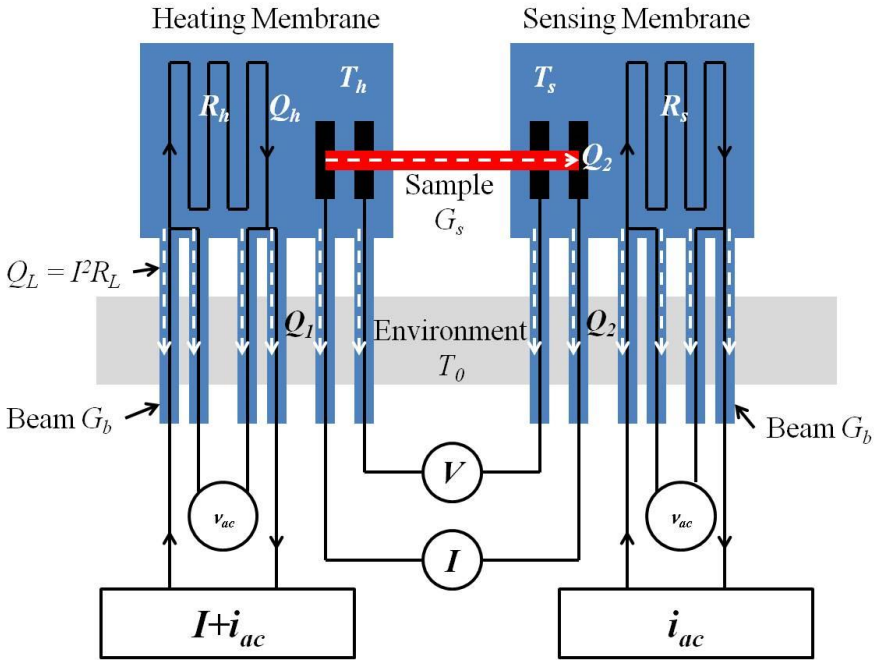

Figure 2.13 The thermal circuit of the measurement setup.

The six beams supporting each membrane are designed to be identical. Below 400 K, heat losses from the membrane and the six supporting beams to the environment through radiation and residual air conduction/convection are small as compared to the conduction heat transfer through the six beams. The total thermal conductance of the six beams can be written as $G_b = R_b^{-1} = 6k_lA/L$, where k_l, A, and L are the thermal conductivity, cross sectional area, and length of each beam, respectively. We can obtain the following equation from the thermal resistance circuit shown in **Figure 2.13**,

$$Q_2 = G_b(T_s - T_0) = G_s(T_h - T_s), \tag{2.1}$$

where G_s is the thermal conductance of the sample, consisting of the intrinsic thermal resistance of the sample and the contact thermal resistance between the sample and the two membranes, i.e.

$$G_s = \frac{1}{R_s} = (\frac{1}{G_n} + \frac{1}{G_c})^{-1}. \tag{2.2}$$

Here $G_n = k_nA_n/L_n$ is the intrinsic thermal conductance of the 1D nanostructure, where k_n, A_n and L_n are the thermal conductivity, cross sectional area, and length of the sample segment between the two membranes, respectively. G_c is the contact thermal conductance between the sample and the two membranes. Because the temperature rise ΔT_h is small, G_s, G_b and G_c are assumed to be constant as ΔT_h is ramped up.

G_b and G_s can be further expressed as a function of ΔT_h, ΔT_s ($\Delta T_s = T_s - T_0$), Q_h and Q_L, as

$$G_b = \frac{Q_h + Q_L}{\Delta T_h + \Delta T_s}, \tag{2.3}$$

and

$$G_s = G_b \frac{\Delta T_s}{\Delta T_h - \Delta T_s} . \tag{2.4}$$

Q_h and Q_L can be calculated readily from the current and the voltage drops across the heating PRT and the Pt leads. ΔT_h and ΔT_s are calculated from the measured resistance of the two PRTs and their temperature coefficient of resistance (TCR = (dR/dT)/R). The four-probe electrical resistance R_s of the sensing PRT is measured using an SR850 lock-in amplifier with a ~300 nA 637 Hz sinusoidal excitation current. The temperature rise of the sensing membrane ΔT_s depends on the dc current I of the heating PRT, and is related to R_s according to the following equation

$$\Delta T_s(I) = \frac{\Delta R_s(I)}{\frac{dR_s}{dT}}, \tag{2.5}$$

where $\Delta R_s(I) = R_s(I) - R_s(0)$.

The temperature rise of the heating membrane, ΔT_h, can be obtained in the similar way. A 300-500 nA sinusoidal current, i_{ac}, with a frequency f can be coupled to the much larger dc heating current I. An SR850 lock-in amplifier is used to measure the first harmonic component (v_{ac}) of the voltage drop across the heating PRT, yielding $R_h = v_{ac}/ i_{ac}$. For R_h obtained by this method, it can be shown that

$$\Delta T_h(I) = \frac{\Delta R_h(I)}{3\frac{dR_h}{dT}}, \text{ for } f << \frac{1}{2\pi\tau} \tag{2.6a}$$

and

$$\Delta T_h(I) = \frac{\Delta R_h(I)}{\frac{dR_h}{dT}}, \text{ for } f >> \frac{1}{2\pi\tau} \tag{2.6b}$$

where τ is the thermal time constant of the suspended device, and is estimated to be on the order of 10 ms. The difference between these two solutions for different frequency ranges is caused by a first harmonic modulated heating component, i.e. $2i_{ac}IR_h$. At a very low (high) frequency compared to $1/(2\pi\tau)$, the modulated heating yields a nontrivial (trivial) first harmonic component in T_h. This further causes a nontrivial (trivial) first harmonic oscillation in R_h. This effect gives rise to a factor of 3 difference in ΔR_h measured by the lock-in method. In addition, τ is proportional to C/k, where C and k are the heat capacity and thermal conductivity, respectively. According to the kinetic theory, k is proportional to Cl, where l is the phonon mean free path and increases as temperature drops. Hence, τ is proportional to $1/l$ and decreases for lower temperature. Therefore, the transition between the two solutions in Eq. (2.6) occurs at an increased frequency as the temperature decreases. In practice, we use f = 1400 Hz, for which Eq. (2.6b) is valid in the temperature range of 20−420 K.

To measure additional electrical and thermophysical properties (Seebeck coefficient, electrical resistance) of 1D nanostructures, the sample can be placed across the four platinum electrodes on the SiN_x membrane and the contacts between the sample and platinum electrodes can be treated with EBID to enhance the electrical contact and minimize the contact electrical and thermal resistance, as mentioned before. The four electrodes make it possible to conduct four probe electrical resistance measurements.

For samples of significant thermoelectric effects, the temperature difference of the two membranes yields a Seebeck voltage that can be measured using the inner two Pt probes contacting the nanostructure, i.e. $V_{TE} = (S_s - S_{Pt})(T_h - T_s)$. The Seebeck coefficient of

the Pt electrodes, S_{Pt}, is small and can be calibrated separately. By measuring T_h, T_s, and V_{TE}, the Seebeck coefficient S_s of the sample can be obtained.

2.5 Measurement Sensitivity

The sensitivity of thermal conductance measurement determines the minimum or noise-equivalent sample thermal conductance that can be measured using the microdevice. Usually $\Delta T_h >> \Delta T_s$ in our measurements. Hence, from Eq. (2.4), the noise-equivalent thermal conductance (NEG_s) of the sample is proportional to the noise-equivalent temperature rise (NET) of the sensing membrane, i.e.

$$NEG_s = G_b \frac{NET}{\Delta T_h - \Delta T_s}. \tag{2.7}$$

The *NET* is further related to the noise equivalent resistance (*NER*) in the R_s measurement as

$$NET = \frac{NER / R_s}{TCR}. \tag{2.8}$$

For the resistance measurement method using a lock-in amplifier,

$$\frac{NER}{R_s} = \frac{\delta \upsilon}{\upsilon} + \frac{\delta i}{i}, \tag{2.9}$$

where $\delta \upsilon$ and δi are the noise in the ac voltage measurement and that of the current source, respectively.

There are a variety of intrinsic noise sources which are present in all electronic signals, such as Johnson noise, Shot noise and *1/f* noise. Shot noise originates from the non-uniformity in the electron flow. It can appear as voltage noise when current is passed through a resistor, or as noise in a current measurement. The Shot noise is given by

$$I_{noise}(rms) = \sqrt{2qI\Delta f}\ , \tag{2.10}$$

where q is the electron charge (1.6×10^{-19} Coulomb), I is the RMS ac current or dc current depending on the circuit, Δf is the bandwidth. Since the current input of lock-in is used to measure an AC signal current, the bandwidth Δf is small that the influence of Shot noise can be neglected.

1/f noise arises from fluctuations in resistance due to current flowing through the resistor and has a *1/f* spectrum, where *f* is the frequency. The *1/f* noise is typically small, for example, for carbon composition resistors, the *1/f* noise is typically 0.1 μV – 3 μV of rms noise per Volt of applied voltage across the resistor. Metal film and wire-wound resistors have about 10 times less noise (StanfordResearchSystems 2007). In our measurement, where the frequency of ac excitation current is set as 637 Hz and 1400 Hz, the influence of *1/f* noise can also be neglected.

Johnson noise is the electronic noise generated due to thermal fluctuations in the electron density within the resistor. These fluctuations give rise to an open-circuit noise voltage,

$$\delta\upsilon = \sqrt{4k_B TR\Delta f}\ , \tag{2.11}$$

where k_B is the Boltzmann's constant, T is temperature, R is the resistance, and Δf is the noise bandwidth. For a sensing PRT with resistance R_s = 5 kΩ and for lock-in SR850 with a noise bandwidth of 0.3 Hz, $\delta\nu \approx 5$ nV, the voltage on the sensing PRT $\nu = iR_s$ = 1.5 mV. Therefore,

$$\frac{\delta\upsilon}{\upsilon} = \frac{5}{1.5}\frac{nV}{mV} \approx 3.3\times 10^{-6}.$$

The current source $i = v_{out}/R$, where v_{out} is a sinusoidal 637 Hz output voltage from the lock-in amplifier and R is the 1 MΩ resistance of a 10 ppm/K precision resistor that is coupled to the sinusoidal voltage output of the lock-in amplifier for converting a constant ac voltage source to a constant ac current source. Therefore,

$$\frac{\delta i_{ac}}{i_{ac}} = \frac{\delta \upsilon_{out}}{\upsilon_{out}} + \frac{\delta R}{R}. \tag{2.12}$$

The relative noise in the ac voltage output from the lock-in amplifier ($\delta\upsilon_{out}/\upsilon_{out}$) is about 4×10^{-5}, The resistance fluctuation of the 1 MΩ precision resistance $\delta R/R = 10 \times 0.2 / (1 \times 10^6) = 2 \times 10^{-6}$, for a 0.2 K fluctuation of room temperature. Therefore, $\delta i_{ac}/i_{ac} \sim 4.2 \times 10^{-5}$. The noise in the current source is the dominant noise source. From Eqs. (2.10) – (2.12), we can get

$$\frac{NER}{R_s} \approx 4.5 \times 10^{-5}. \tag{2.13}$$

The resistance of the sensing PRT at baseline temperature, R_s ($I = 0$) is measured in the temperature range of 20 – 420 K. As an example, the measured zero current resistance for a measurement with a silicon nanoribbon as the sample is shown in **Figure 2.14**. As pointed out by Chen *et al.* (Chen, Jang *et al.* 2009), a simple linear fit $R_s(T) = a_0 + a_1 T$ is clearly inadequate to fit $R_s(T)$ over the entire temperature ranges of interest. Instead, a Bloch-Grüneisen (BG) formula that includes three adjustable parameters is used to fit the measured $R_s(T)$ (Ziman 1960; Poker and Klabunde 1982; Bid, Bora *et al.* 2006), shown as the solid line in **Figure 2.14**. Compared with linear fitting, the BG fit gives a much better fitting result for measured resistance of the sensing PRT $R_s(T)$. As expected the residuals of the BG fit is much smaller than the linear fit, as shown in **Figure 2.15**.

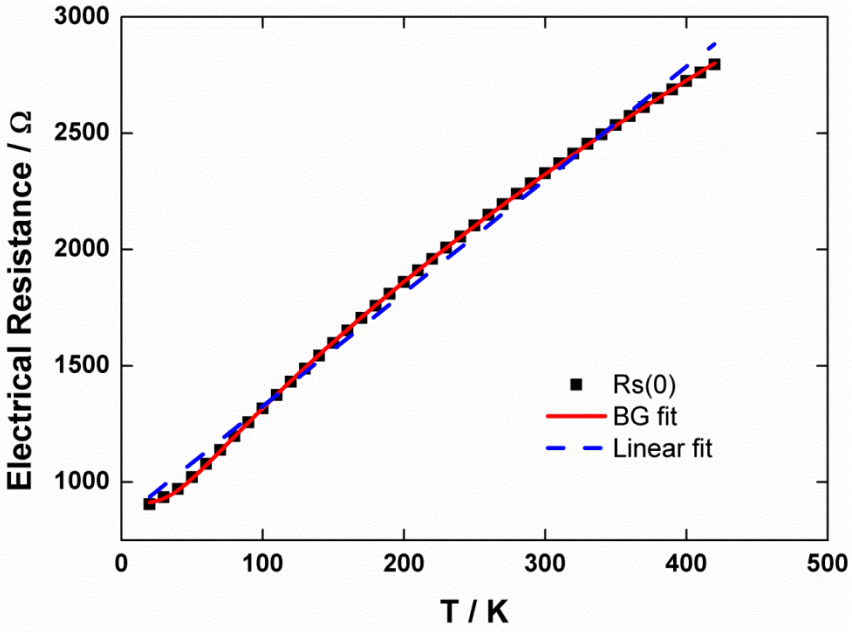

Figure 2.14 The resistance (R_s ($I=0$)) of the PRT as a function of temperature.

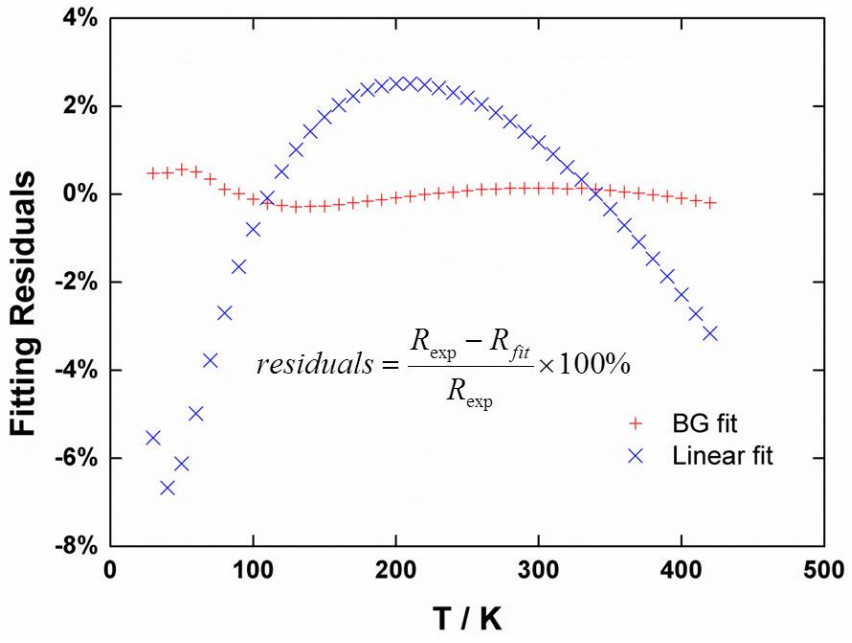

Figure 2.15 Fitting residuals for the BG fit and linear fit.

Figure 2.16 shows the Temperature Coefficient of Resistance (TCR) as a function of temperature from the same measurement as shown in **Figure 2.14**. The TCR is roughly in the range of $8 \times 10^{-4} - 5.5 \times 10^{-3}$ K^{-1} in the whole temperature domain. Take TCR within this range and substituting Eq. (2.13) into Eq. (2.8), we can get NET in the range of 8 – 56 mK, which is smaller than the temperature rise in the sensing membrane ΔT_s for most 1-D samples we measured.

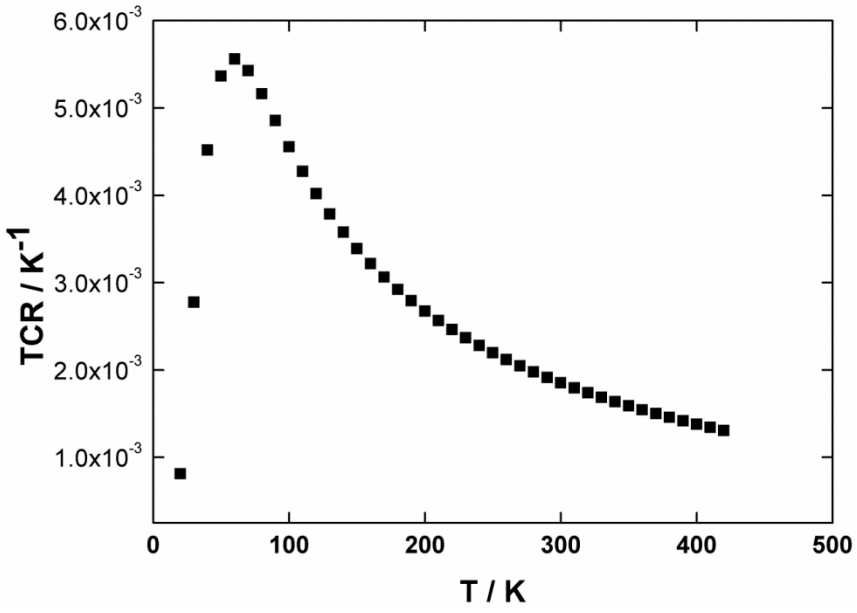

Figure 2.16 Temperature Coefficient of Resistance (TCR) as a function of temperature.

The calculated thermal conductance (G_b) of the six beams according to Eq. (2.3) is shown in **Figure 2.17**. From Eq. (2.7) and Eq. (2.8) we know that for a certain temperature excursion $\Delta T_h - \Delta T_s$, the noise-equivalent thermal conductance (NEG_s) is proportional to G_b/TCR. **Figure 2.18** shows G_b/TCR as a function of temperature, which increases monotonically. Therefore, for a temperature excursion $\Delta T_h - \Delta T_s$ = 2 K, NEG_s

will sit in the range between 1.71×10^{-10} W/K (T = 20 K) and 1.37×10^{-9} W/K (T = 420 K). At room temperature (T = 300 K), $NEG_s \approx 8.17 \times 10^{-10}$ W/K.

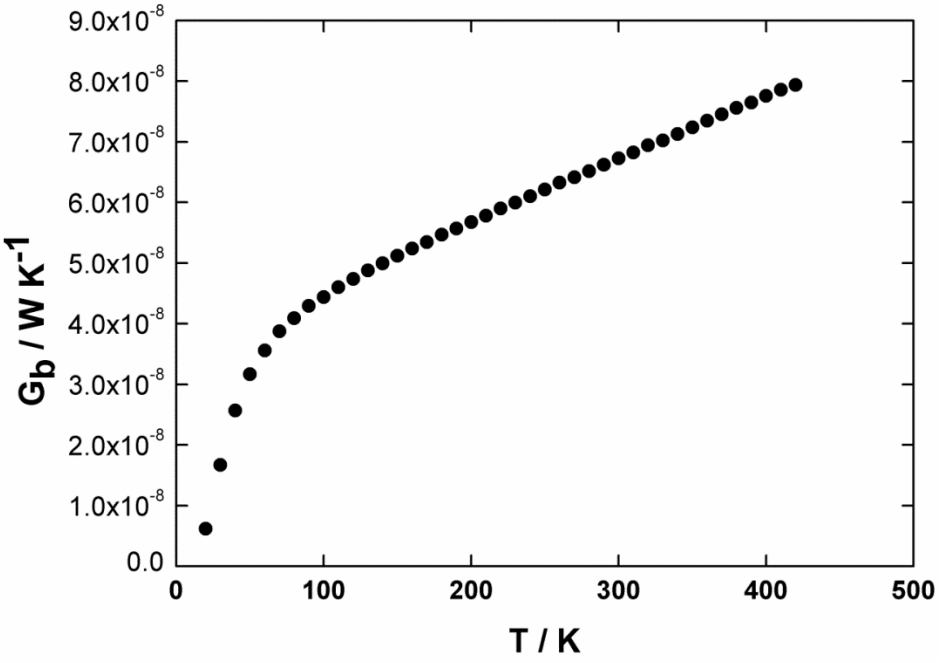

Figure 2.17 Thermal conductance (G_b) of the six beams as a function of temperature.

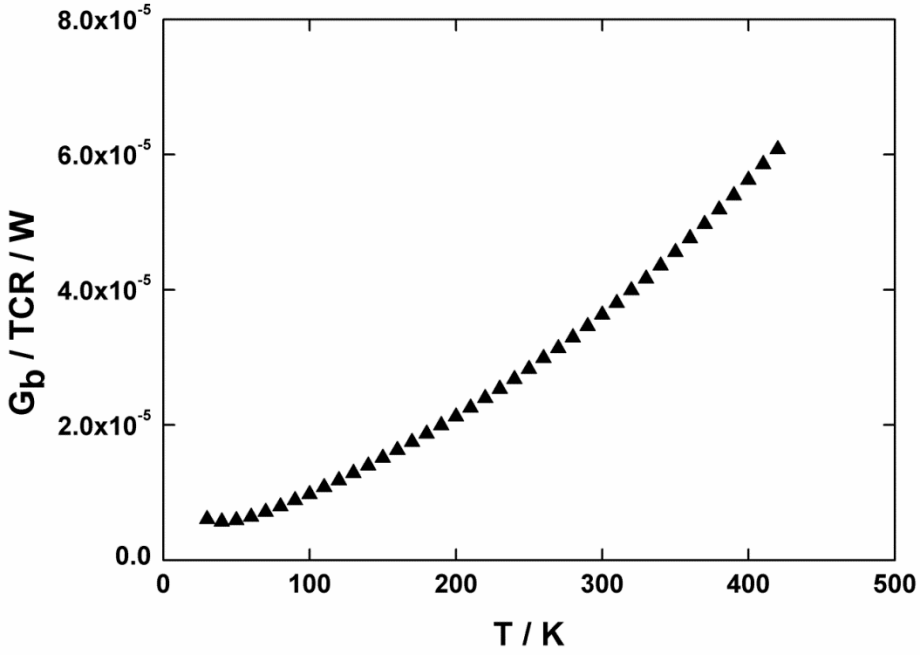

Figure 2.18 G_b / *TCR* as a function of temperature.

2.6 Measurement Error

One error source in the measurement is the heat transfer between the two membranes via radiation and air conduction/convection. The radiation thermal conductance can be estimated as (Shi, Li *et al.* 2003)

$$G_{h-s\_rad} = \sigma(T_s + T_h)(T_s^2 + T_h^2)F_{h-s}A, \tag{2.14}$$

where σ is Stefan-Boltzmann constant, $F_{h\text{-}s}$ is the view factor between the two adjacent membranes, A is the surface area of one membrane. It was estimated that $F_{h\text{-}s}A \approx 9.6\ \mu m^2$. From Eq. (2.14) we can get $G_{h\text{-}s\_rad} \approx 1.6 \times 10^{-10}$ W/K at 420 K and 1.7×10^{-14} W/K at 20 K. Compared with the measurement sensitivity we got, they are significantly lower.

The thermal conductance of air can be written as $G_{h\text{-}s\_air} = k_a A_{eq}/D$, where k_a is the thermal conductivity of the residual air molecules in the evacuated cryostat, A_{eq} and D are the equivalent surface area of the membrane and the distance between the two membranes, respectively. For a vacuum pressure of 1×10^{-5} Torr, the mean free path of air molecules is of the order of 1 m and is much larger than D. Under such circumstance, according to the kinetic theory,

$$k_a = \frac{C\upsilon D}{3}, \tag{2.15}$$

and

$$G_{h-s\_air} = \frac{C\upsilon A_{eq}}{3}, \tag{2.16}$$

where C and υ are the heat capacity and velocity of air molecules. From Eq. (2.16), it can be estimated that $G_{h\text{-}s\_air} = 2.8 \times 10^{-12}$ W K^{-1} at T = 300 K, well below the measurement sensitivity of 8.17×10^{-10} W/K.

2.7 Measurement Uncertainty

The uncertainty propagation in this measurement method is very complex and as a result, it is difficult to do an analytical calculation including all uncertainty sources. Therefore, Monte Carlo simulation, which does not require propagation equations with inherent approximation, is adopted to conduct uncertainty analysis of the electrical measurements.

2.7.1 General Approach of the Monte Carlo Method (MCM)

Figure 2.19 presents a flowchart that shows the steps involved in performing an uncertainty analysis using the Monte Carlo Method (MCM). The figure shows the sampling technique for a function of two variables, but the methodology is general for data reduction equations or simulations that are functions of multiple variables (Coleman and Steele 2009). As shown in the flowchart, first the assumed true value of each variable in the result is input. These would be the X_{best} values that we have for each variable. Then the estimates of the random standard uncertainty s and the elemental systematic standard uncertainties b_k for each variable are input. An appropriate probability distribution function is assumed for each error source. The random errors are usually assumed to come from a Gaussian distribution and the systematic error distributions are chosen based on the user's judgment. For the flowchart in **Figure 2.19**, it is assumed that the random standard uncertainties for variables X and Y come from Gaussian distributions and that each variable has three elemental systematic standard uncertainties, one Gaussian, one triangular, and one rectangular.

For each variable, random values for the random errors and each elemental systematic error are found using an appropriate random number generator (Gaussian,

rectangular, triangular, etc.). The individual error values are then summed and added to the true values of the variables to obtain "measured" values. Using these measured values, the result is calculated. This process corresponds to running the test or simulation once.

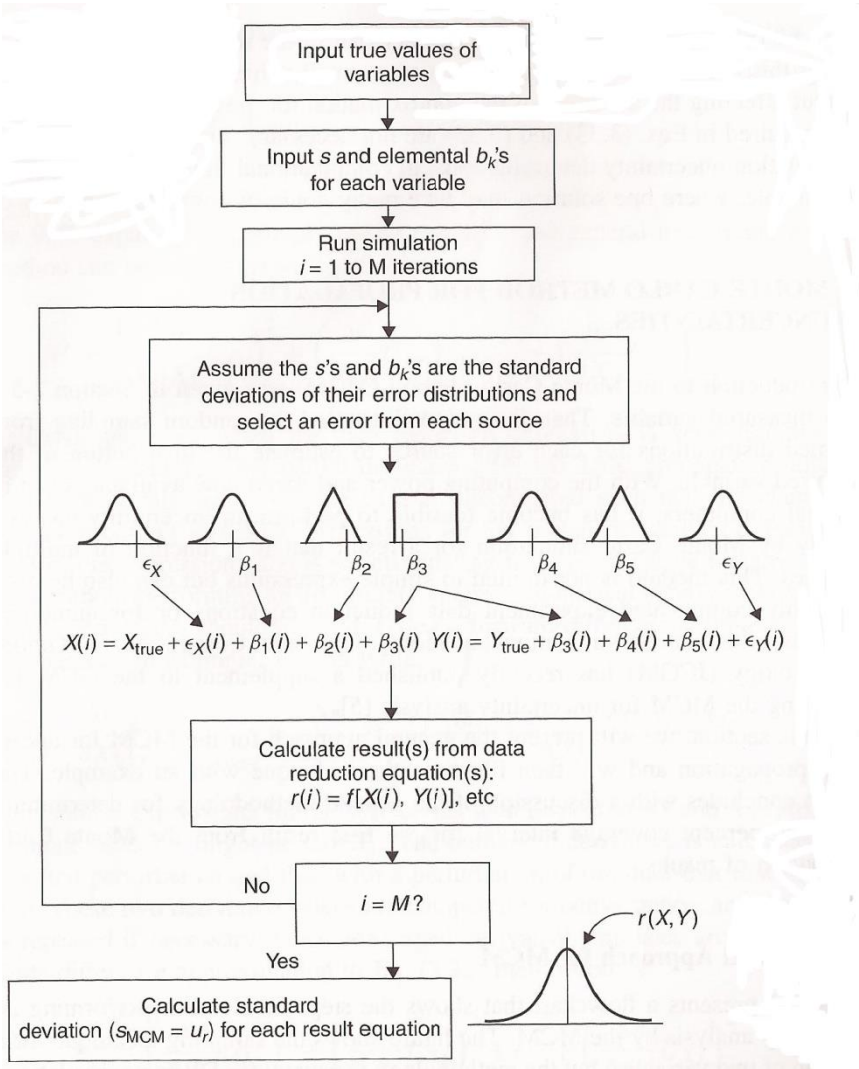

Figure 2.19 Schematic flowchart of Monte Carlo simulation (Coleman and Steele 2009).

The sampling process is repeated *M* times to obtain a distribution for the possible result values. The primary goal of this iteration process is to estimate a converged value for the standard deviation, s_{MCM}, of this distribution. An appropriate value for *M* is

determined by periodically calculating s_{MCM} during MCM process and stopping the process when a converged value of s_{MCM} is obtained. Perfectly converged value of s_{MCM} is not necessarily required to have a reasonable estimate of the combined standard uncertainty of the result, u_r. Once the s_{MCM} values are converged to within 1-5%, then the value of s_{MCM} is a good approximation of the combined standard uncertainty of the result. Assuming that the central limit theorem applies, the expanded uncertainty for the result at a 95% level of confidence is $U_r = 2u_r$ (Coleman and Steele 2009).

2.7.2 True values of variables

In our measurements, the thermal conductance is decided by the heating current, I_{DC}, the ac voltage drop on the heating coil, v_{acH}, and the ac voltage drop on the sensing coil, v_{acS}, the sine output of lock-in amplifier of the heating side, v_{sineH}, and that of sensing side, v_{sineS}, etc. So the assumed true values of variables needed to be input are the values of I_{DC}, v_{acH}, v_{acS}, v_{sineH}, v_{sineS}, etc.

For the sine output, v_{sineH} and v_{sineS}, we can simply use the value set in lock-in as the true value. For the resistances of the 1 MΩ and 500 KΩ resistors, the measured resistances are considered as the true value.

Both v_{acH} and v_{acS} are functions of I_{DC}, $v_{acH} = a_H + b_H I_{DC}^2$, $v_{acS} = a_S + b_S I_{DC}^2$. The four coefficients are calculated during experimental data processing procedure, and used to calculate the true values of v_{acH} and v_{acS} at a given I_{DC}.

2.7.3 Random and systematic uncertainty analysis of variables

All the error sources in the setup are shown in **Figure 2.20** denoted by a red ellipse. The ellipse across leg 9 and leg 10 denotes the error of R_{tot}, which is the electrical

resistance between pad 8 and 11. The error of the cryostat is the error of the base temperature of the device in the cryostat. Detailed analysis of these error sources is given as follows.

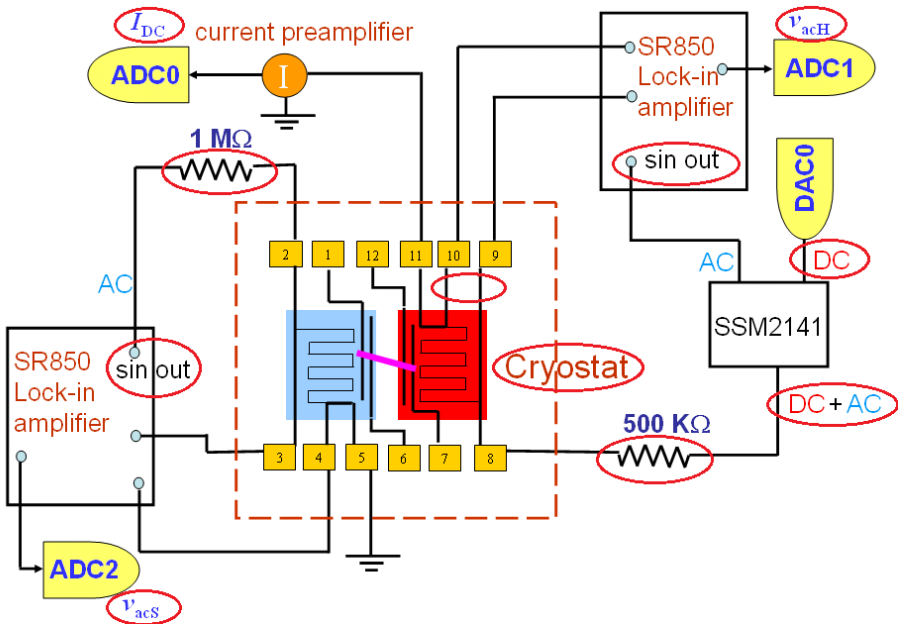

Figure 2.20 Error sources in the electrical measurement set-up.

Error of v_{acH} and v_{acS}

In order to measure the random uncertainty of v_{acH} and v_{acS}, the DC input of SSM2141 is disconnected from DAC0 and grounded by using a 50 Ω terminator, as shown in **Figure 2.21**. At 300 K, the data acquisition program we used in the thermal measurement is run and 116 points are read (sweep 2 cycles, I_{DC} = 0 A). The parameters of the lock-in amplifiers are the same as we used in thermal measurements: 50 for the heating side expand and 100 for the sensing side expand, offsets are selected so that the output of the lock-in amplifiers are about 1 V. The gain of the current preamplifier is 10^5 V/A, which is also the value we used in thermal measurements.

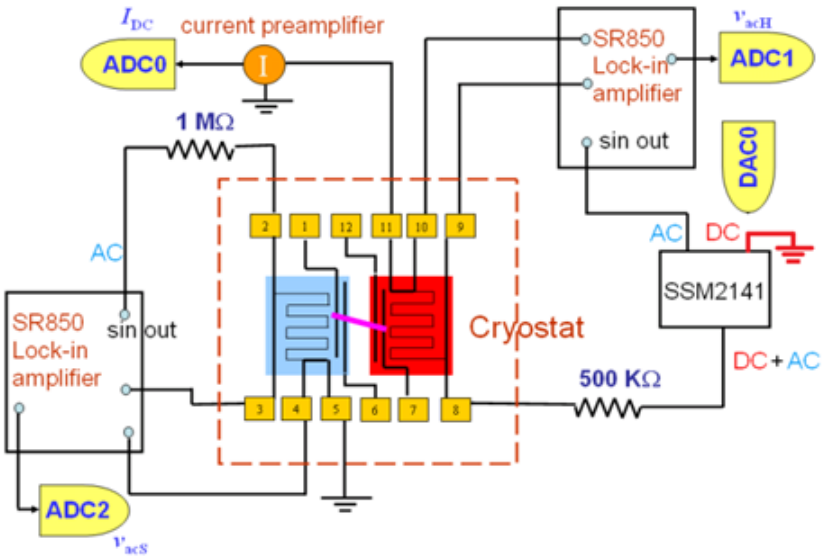

Figure 2.21 The circuit to measure the random uncertainty of v_{acH}, v_{acS} and I_{DC}.

The standard deviations obtained from the data are 0.0038 V and 0.0065 V for the v_{acH} and v_{acS} respectively. Thus the random uncertainties of v_{acH} and v_{acS} are 0.008 V and 0.013 V respectively. The random uncertainty of v_{acS} is about two times that of v_{acH}. This is because the expand of the sensing side is twice that of the heating side.

It should be pointed out that the random uncertainties of v_{acH} and v_{acS} we obtained include the contribution of errors from lock-in amplifier, SSM2141, DAQ hardware and the cryostat. The error of lock-in amplifier is composed of four parts: one is the error induced by the circuit inside lock-in amplifier, the second is the error in expand, the third is the error in the offset, and the fourth is the random error of sine output.

In order to confirm that the random uncertainty of v_{acH} is independent of the heating current, I_{DC}, we use the auxiliary output of sensing side lock-in amplifier to apply a 3 V DC voltage on the DC input of SSM2141. Thus, I_{DC} is constant during data

acquisition. The random uncertainty of the v_{acH} is 0.006 V, very close to what we got for I_{DC} = 0 A.

In order to measure the zero offsets of v_{acH} and v_{acS}, a BNC T connector is used to connect the input A to the input B of the lock-in amplifier, as shown in **Figure 2.22**. Because the signal of input A equals to that of input B, the ideal output should be zero. Thus, the average of the outputs we measured can be considered as the zero offsets of v_{acH} and v_{acS}. The zero offset values we got are 0.00333 V and 0.007788 V for v_{acH} and v_{acS} respectively.

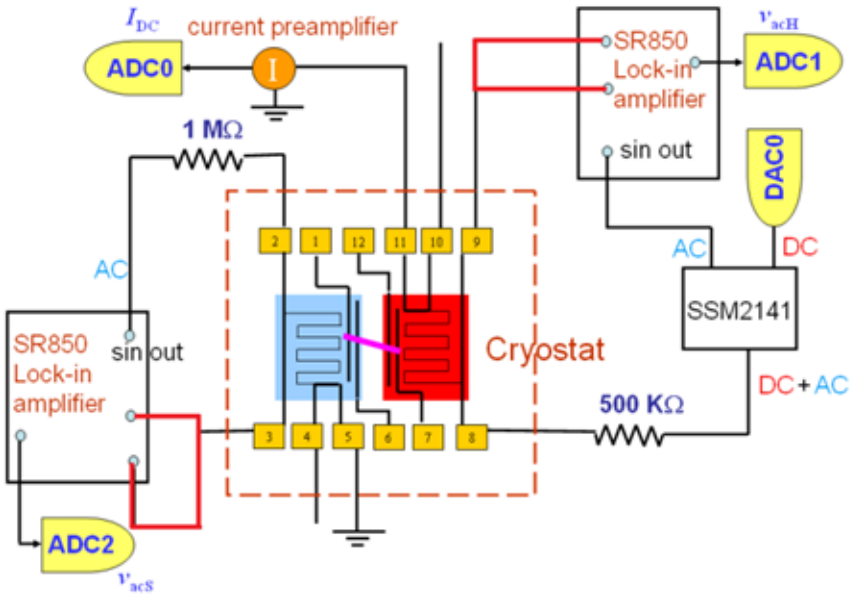

Figure 2.22 The circuit to measure the zero offsets of v_{acH} and v_{acS}.

It should be pointed out that the zero offset we obtained here should be considered in the data processing process, and should not be included in the uncertainty analysis. The systematic uncertainty considered in the uncertainty analysis is a range of zero offset with 95% confidence, and is generally used in the case that we cannot measure the zero offset.

The zero offsets of v_{acH} and v_{acS} given by the measurement include the contribution from the lock-in amplifier and DAQ hardwares.

Error of I_{DC}

The random uncertainty and zero offset of I_{DC} were measured simultaneously with the random uncertainty measurement of v_{acH} and v_{acS} as shown in **Figure 2.21**. The gain of the current preamplifier is 10^5 V/A. The standard deviation is 3.66×10^{-5} V. Thus, the random uncertainty of I_{DC} is about 8×10^{-5} V. The average of the data points is considered as the zero offset of I_{DC}, and is -0.0015 V.

The random uncertainty of I_{DC} includes contributions from the current preamplifier, the DAQ hardware, the SSM2141 and the cryostat.

Take the result of a CNT sample as an example, the parabolic fitting of v_{acH} to I_{DC} gives the zero offset of I_{DC}, which is -0.00172 V, nearly the same as the result we get here.

Base on the same reason for the zero offsets of v_{acH} and v_{acS}, the zero offset of I_{DC} should be considered in the data processing process instead of the uncertainty analysis.

Error of temperature

There are two error sources for base temperature, which should be discussed separately. First the temperature of the position where the thermocouple is mounted, T_b, and the temperature of the device, T_d, as shown in **Figure 2.23**, could be slightly different.

The error of T_b depends on the sensor used. In our system, it is a J-type thermocouple, followed by an OMEGA CN800 temperature controller and a Cryocon 32 temperature controller. The accuracy of this kind of construction is not given in the manual of Cryocon 32 temperature controller. Here we assume that the accuracy of our

control system is nearly equal to that of the system with a silicon diode sensor followed by a Cryocon 32 temperature controller, which is ±10 mK as given in the manual. Thus the systematic uncertainty of the T_b can be taken as B_{Tb}=10 mK.

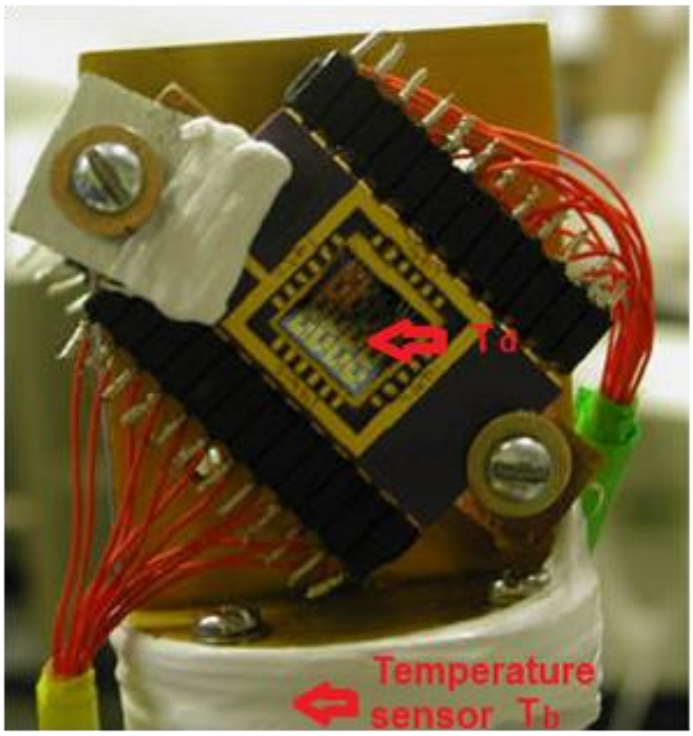

Figure 2.23 Measured temperatures in the cryostat.

The random uncertainty can be determined from the data read from the temperature controller. After an equilibration period of 1.5 hours, the accuracy of the reading is ±2 mK. Thus the random uncertainty of the T_b is P_{Tb} = 2 mK and the total uncertainty of sensor temperature $U_{Tb} = \sqrt{B_{Tb}^2 + P_{Tb}^2}$ =10.2 mK. According to the calibration conducted by Shi in a similar cryostat, the difference between T_b and T_d is less than 0.2% T_b (Shi).

From the log file created in our DAQ program, we know that one sweep cycle takes about 11 minutes. In our measurements, we always sweep 2-3 cycles at each temperature point. The time needed for taking data is about 22-33 minutes, which is far larger than the period of the base temperature fluctuation. So the contribution of the variation of T_b and T_d to the uncertainty of the measurement has been considered in the random errors of I_{DC}, v_{acH} and v_{acS} and does not need to be considered separately.

The only important factor needs to be considered here is the systematic error of T_b, which is 10 mK, as described before. Even at 20 K, it is only 0.05% of the base temperature. Therefore, we neglect the systematic error from the base temperature.

Error of the sine output of the lock-in amplifier

As given in the manual of SR 850 lock-in amplifier, the systematic error of the sine output is 0.004 V. As mentioned earlier, the contribution of the random uncertainties of sine outputs has been considered in the random uncertainties of v_{acH} and v_{acS}.

Error of the electrical resistance

There are four electrical resistances in the circuit need to be considered: the resistance of the 1 MΩ resistor, the resistance of the 500 KΩ resistor, the resistance between pad 2 and pad 5 ($R_{totS} = R_{coilS}+2R_{LS}$) at 300 K (as shown in **Figure 2.20**), and the resistance between pad 8 and pad 11 ($R_{totH} = R_{coilH}+2R_{LH}$) at 300 K. All of these resistances are measured by a Triplett 4404 digital multimeter. Generally, the accuracy of digital multimeter is (0.1%+1) to (0.7%+1). For the sake of safety, we use B_R=1%.

2.7.4 Overall uncertainty

From the electrical measurement, we get thermal conductance of the sample (G_s) and the measurement uncertainty of G_s was found through Monte Carlo simulation, as described in the previous section. In order to get thermal conductivity of the sample (κ_s), which is related to the thermal conductance G_s as:

$$\kappa_s = G_s \frac{L}{A}, \tag{2.17}$$

where L is the length of the sample between the two membranes, A is the cross-sectional area of the sample. Both L and A are determined through metrical tools such as Scanning Electron Microscope (SEM) or Atomic Force Microscope (AFM). If U_L and U_A represent the uncertainties of measured value of L and A at a 95% level of confidence, then the overall uncertainty of thermal conductivity U_κ can be calculated following the standard approach of uncertainty propagation as (Coleman and Steele 2009):

$$U_\kappa^2 = (\frac{\partial \kappa}{\partial G_s})^2 U_{G_s}^2 + (\frac{\partial \kappa}{\partial L})^2 U_L^2 + (\frac{\partial \kappa}{\partial A})^2 U_A^2. \tag{2.18}$$

If we divide both sides of Eq. (2.18) by κ^2, then we can get the overall relative uncertainty of measured thermal conductivity as

$$(\frac{U_\kappa}{\kappa})^2 = (\frac{U_{G_s}}{G_s})^2 + (\frac{U_L}{L})^2 + (\frac{U_A}{A})^2 \tag{2.19}$$

2.8 Summary

We developed a wafer-scale microfabrication process to fabricate suspended micro-devices with various designs. Individual 1D nanostructures can be placed bridging

the two suspended membranes through a two-step transfer process assisted with an in-house assembled micromanipulator, forming a thermal conduction route. Electron beam induced deposition (EBID) technique can be used to improve the thermal and electrical contacts between the sample and the membranes. The details of the experimental procedure have been discussed for simultaneous measurements of the thermal, electrical conductance and Seebeck coefficient of 1D nanostructures with a thorough uncertainty analysis.

3. INTRINSIC THERMAL CONDUCTIVITY OF MULTI-WALLED CARBON NANOTUBES

Carbon Nanotubes (CNTs), since their discovery by *Iijima* about two decades ago (Iijima 1991), has triggered great scientific and engineering interest because of their superior mechanical, electrical and thermal properties. Several experimental studies have been carried out to determine the thermal conductivities of individual CNTs, which presented both high and low values that span two orders of magnitude (Kim, Shi *et al.* 2001; Chiu, Deshpande *et al.* 2005; Yu, Shi *et al.* 2005; Choi, Poulikakos *et al.* 2006; Pop, Mann *et al.* 2006; Pettes and Shi 2009). The discrepancy in these experimental results has been attributed to the difference in the tube quality (Pettes and Shi 2009).

However, for all reported experiments, the derived thermal conductivity is an effective one, which includes effects of both the intrinsic thermal resistance of the CNTs and the contact thermal resistance between the CNT and the heat source/sink. Thus, the intrinsic thermal conductivity of the CNTs, without any negative contribution from the contact thermal resistance, should be even higher. In fact, inclusion of the contact thermal resistance is likely the reason that all experimentally observed CNT thermal conductivities (up to 3500 W $m^{-1} K^{-1}$ at room temperature (Pop, Mann *et al.* 2006)) are lower than the theoretical prediction of (6600 W m^{-1} K^{-1} for a SWCNT at room temperature (Berber, Kwon *et al.* 2000)). Therefore, to what extent the effective thermal conductivity underestimates the intrinsic one, and how much contribution the contact

thermal resistance makes to the measured total thermal resistance remain unresolved issues.

This chapter will discuss determination of the intrinsic thermal conductivity of a MWCNT and its contact thermal resistance with the supporting membranes through multiple measurements of the same MWCNT sample with different suspended lengths of MWCNT segments between the heat source and the heat sink.

3.1 Measurement Method

The measurements were performed with the suspended microdevice that has been discussed in details in Chapter 2. **Figure 3.1** shows the scanning electron microscopy (SEM) micrograph of a 66-nm-diameter MWCNT aligned in different configurations with different length CNT segments between the two suspended membranes. Without Electron Beam Induced Deposition (EBID) contact treatment, the same MWCNT was measured three times with the length of the CNT segment between the two membranes, L_M, as 12.1 μm (**Figure 3.1(a)**), 5.0 μm (**Figure 3.1(b)**), and 4.4 μm (Figure **3.1(c)**). From these measurement results, the intrinsic thermal conductivity of the MWCNT and the CNT-membrane contact thermal resistance can be extracted. It is worth noting that in all three configurations, the smallest radius of curvature is ~ 820 nm, and according to Chang *et al.* (Chang, Okawa *et al.* 2007), bending like this does not affect the thermal conductivity of CNTs. In addition, after the measurement with 4.4 μm long CNT segment between the two membranes, gold was deposited locally by EBID at the tube–membrane contacts near the edge of the membranes to enhance the contact thermal conductance, as shown in Figure **3.1(d)**. Comparison of the measurement results before and after the

EBID contact treatment allows us to estimate the effectiveness of EBID gold deposition in reducing the CNT–membrane contact thermal resistance.

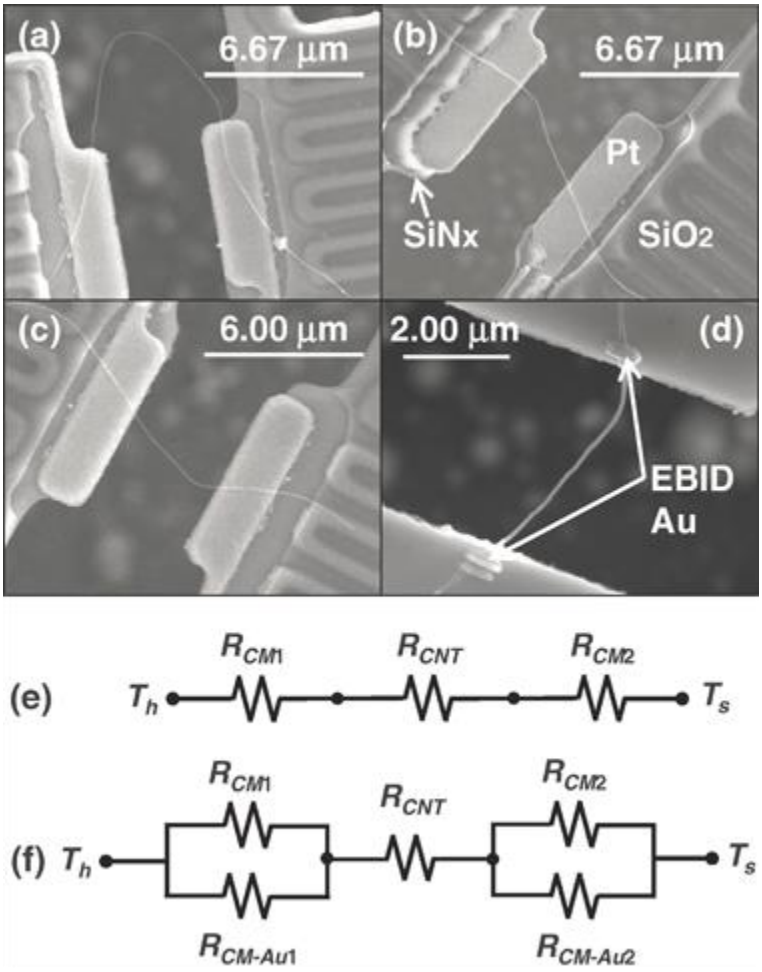

Figure 3.1 (a–d) SEM micrograph of the MWCNT sample, and **(e,f)** the corresponding thermal resistance circuits. The length of the CNT segment between the two membranes is measured as **(a)** 12.1μm **(b)** 5.0 μm **(c)** 4.4 μm and **(d)** 4.4 μm. The CNT in **(c)** and **(d)** is of the same alignment, but gold is locally deposited at the CNT–membrane contact in **(d)** to reduce the contact thermal resistance. **(e)** The thermal resistance circuit for the samples in **(a)** to **(c)**; and **(f)** the thermal resistance circuit for the sample in **(d)**. T_h and T_s are the temperatures of the heat source and the heat sink, respectively.

As shown in **Figure 3.1(e)**, for samples with no EBID contact treatment, the obtained total thermal resistance, R_{tot}, includes the intrinsic thermal resistance of the CNT segment between the two membranes, R_{CNT}, and the contact thermal resistance between the CNT and the two membranes, R_{CM1} and R_{CM2}. The total contact thermal resistance, R_{CM}, is the sum of R_{CM1} and R_{CM2}. To explicitly express the relation between the measured total thermal resistance and the CNT length between the two membranes, we further write R_{CNT} as a product of $R_{CNT/L}$, the CNT thermal resistance per unit length, and L_M, the suspended CNT length. Thus, R_{tot} can be expressed as:

$$R_{tot} = R_{CM} + R_{CNT/L} \times L_M . \tag{3.1}$$

If the CNT segment on each membrane is long enough, then we can assume that R_{CM} is the same in different measurements, as will be further justified later. Therefore, we can extract $R_{\mathrm{CNT/L}}$ and R_{CM} from the measured thermal resistance of two different measurements as

$$R_{CNT/L} = (R_{tot2} - R_{tot1})/(L_{M2} - L_{M1}), \tag{3.2a}$$

$$R_{CM} = (L_{M2}R_{tot1} - L_{M1}R_{tot2})/(L_{M2} - L_{M1}), \tag{3.2b}$$

where R_{tot1} and R_{tot2} are the measured total thermal resistance from two different measurements, and L_{M1} and L_{M2} are the corresponding suspended CNT lengths between the two membranes in each measurement.

3.2 Measured Total Thermal Conductance

The measured total thermal conductance (G_s), which is equal to $1/R_{tot}$, is given in **Figure 3.2** as a function of temperature (T). **Figure 3.2** indicates that G_s decreases as L_M increases over the whole measurement temperature range, which is reasonable because

the longer the suspended CNT segment between the two membranes is, the larger R_{CNT} is. **Figure 3.2** also shows that EBID of gold at the CNT–membrane contacts further increases the measured total thermal conductance because the gold deposition reduces the overall contact thermal resistance, R_{CM}, by providing additional heat transfer routes between the CNT and the membranes, as shown in **Figure 3.1(f)**. Based on the assumption we made previously that R_{CM} is the same in different measurements, R_{tot} should be linearly proportional to L_M, according to Eq. (3.1). The inset in **Figure 3.2**, which plots R_{tot} at 300 K as a function of L_M, suggests that this is the case. The linear relationship has also been observed in the measurement of other samples.

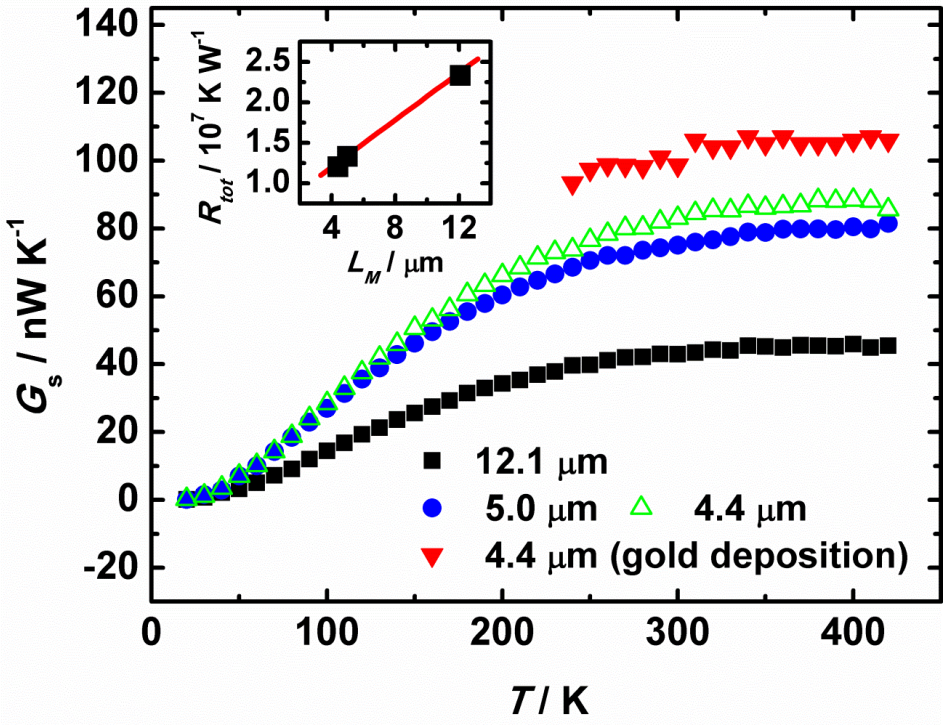

Figure 3.2 Measured total thermal conductance as a function of temperature for different cases. The legend indicates the length of the CNT segment between the two suspended membranes. The inset shows the total thermal resistance versus the CNT length between the two membranes at 300 K.

3.3 Intrinsic Thermal Conductivity of the CNT

Two sets of $R_{CNT/L}$ are calculated by comparing the R_{tot} from the measurement with L_M = 12.1 μm and those from the measurements with L_M = 5.0 μm and L_M = 4.4 μm. Based on the derived $R_{CNT/L}$, we can solve for the intrinsic thermal conductivity of the CNT, which, unlike the effective thermal conductivity derived directly from a single measurement of R_{tot}, eliminates the effect of contact thermal resistance. The solved intrinsic thermal conductivity (k) of the CNT, together with the effective ones calculated directly from each single measurement, is given in **Figure 3.3**.

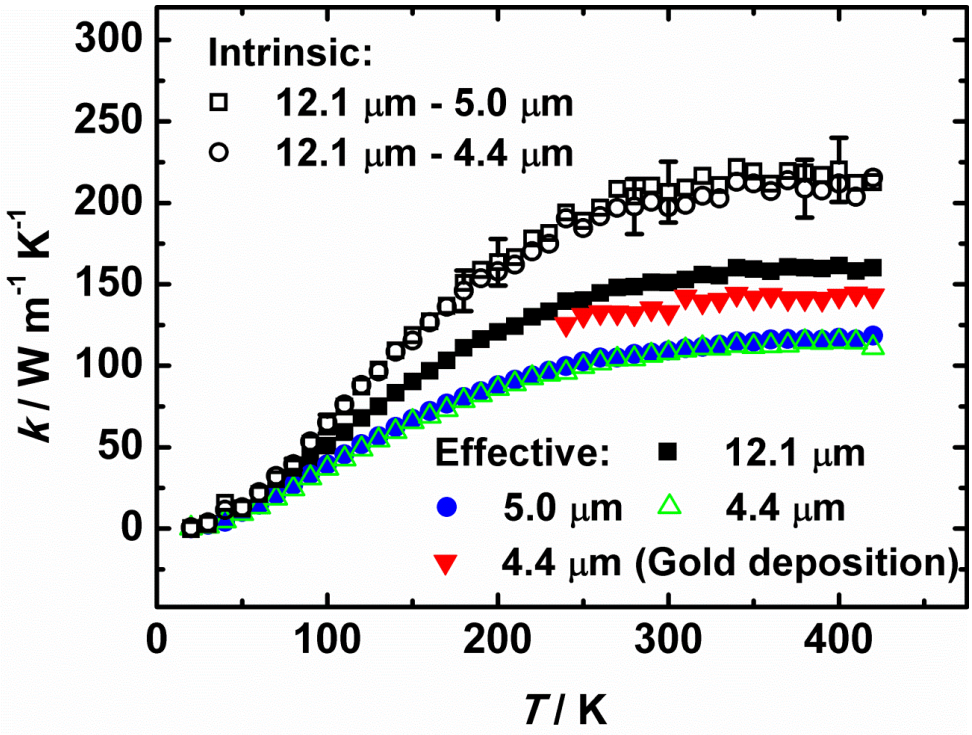

Figure 3.3 Extracted intrinsic thermal conductivity of the CNT, together with the effective thermal conductivity evaluated from each single measurement. The legend indicates the CNT length between the two membranes and the pair of measurements used for extracting the intrinsic CNT thermal conductivity.

The two sets of intrinsic thermal conductivities fit each other very well and the values are significantly larger than the effective thermal conductivities derived from any single measurements. We did not calculate the intrinsic thermal conductivity from the two measurements with L_M as 5.0 and 4.4 μm because of the small length difference, which tends to lead to large uncertainties in the results. **Figure 3.3** also indicates that the obtained effective thermal conductivity from one single measurement increases as L_M increases. This is because for the measurement with a larger L_M, R_{CNT} is larger, and the ratio of R_{CM} to R_{tot} is smaller. However, even with L_M = 12.1 μm, the obtained effective thermal conductivity is still significantly lower than the intrinsic thermal conductivity.

The intrinsic thermal conductivity of the MWCNT at room temperature is only slightly higher than 200 W m^{-1} K^{-1}, which is most probably due to the poor structural quality of the tube synthesized by chemical vapor deposition. **Figure 3.4** is the Raman spectrum of the MWCNTs, with a transmission electron microscopy (TEM) image as an inset. The peaks at 213 and 273; 1342; 1573; and 2680 cm^{-1} correspond to the radial breathing mode (RBM), disordered (D), graphite (G), and second-order Raman scattering from D-band variation (G′) modes of CNTs, respectively. The observation of RBM lines confirms the presence of CNTs. It is well known that the ratio of the intensity of the D- and G-lines (I_D/I_G) can be used to evaluate the quality of CNTs (Dresselhaus, Dresselhaus *et al.* 2005). The higher the I_D/I_G ratio is, the more bonding defects the CNTs have. The I_D/I_G ratio is usually less than 0.02 (i.e., without observation of the D-lines) for high-quality CNTs without defects and amorphous carbon. For the MWCNT tested in this work, the I_D/I_G is roughly 0.35, implying existence of defects in the sample. The low quality of the CNT sample was also verified by the TEM examination from which a

number of graphite layers, mesoscopic graphite sheets, and encapsulated metal particles were observed.

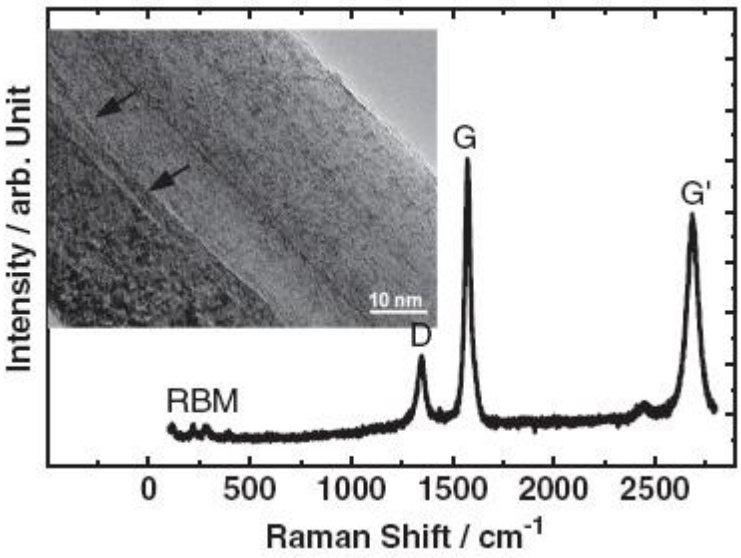

Figure 3.4 Raman analysis results, with a TEM image of the measured CNT sample as the inset. The arrows in the inset indicate the disordering layers.

The experimental results indicate that contact thermal resistance can be a significant portion in the measured total thermal resistance. For example, at room temperature, the contact thermal resistance contributes to approximately 50% of the total thermal resistance in the measurement with L_M = 4.4 μm, which leads to an effective thermal conductivity significantly lower than the intrinsic one. Considering that the thermal conductance obtained by Kim *et al.* (Kim, Shi *et al.* 2001) is about 1.6×10^{-7} W K^{-1} at room temperature, which is larger than the measured total thermal conductance of the CNT with L_M = 4.4 μm in our work (8.3×10^{-8} W K^{-1} and 1.0×10^{-7} W K^{-1} for measurements without and with the EBID gold deposition, respectively), it is likely that contact thermal resistance could still be important in measurement of *Kim et al.* Therefore,

the derived effective thermal conductivity from their experiment (> 3000 W m^{-1} K^{-1} at room temperature) could still significantly underestimate the intrinsic thermal conductivity of the measured CNT, and the intrinsic thermal conductivities of high-quality CNTs can be even higher as that predicted using molecular dynamics simulations (Berber, Kwon *et al.* 2000).

3.4 Contact Thermal Resistance

The two sets of contact thermal resistance between the tube and the suspended membranes, R_{CM}, calculated by comparing the measurements for L_M = 12.1 μm with those for L_M = 5.0 μm and L_M = 4.4 μm, are plotted in **Figure 3.5**. Above 90 K, they are approximately the same, which further verifies the assumption we made previously, in which R_{CM} remains the same in different measurements. Below 90 K, R_{tot} increases rapidly, which leads to reduced heat transfer between the heat source and heat sink, introducing larger experimental uncertainty in R_{CM} and increased difference between the two sets of R_{CM}. The rapid increase in R_{CM} is due to the quickly reduced heat capacity at low temperature, and can be understood based on the acoustic or diffuse mismatch model (Swartz and Pohl 1989). **Figure 3.5** also indicates that R_{CM} only decreases marginally as the temperature increases from 300 to 400 K, which implies that the difference in the measurement temperature may not be the reason for the large scattering in the reported results of CNT-substrate contact thermal resistance in the literature, which were measured at or above room temperature.

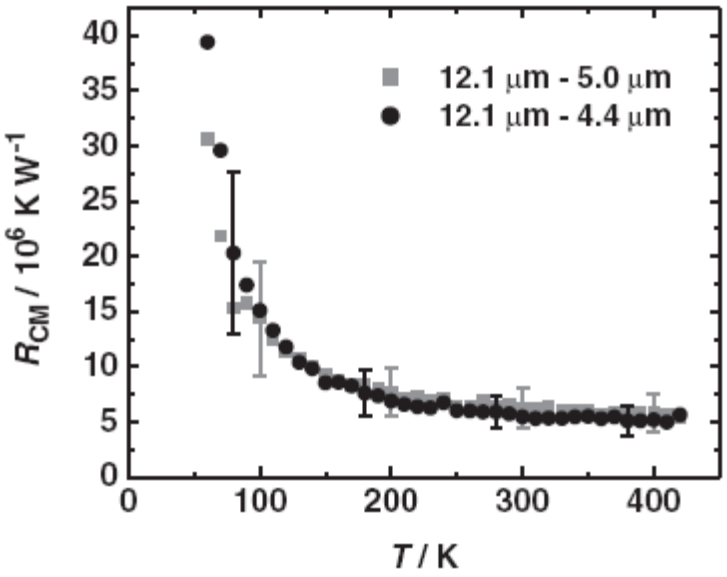

Figure 3.5 Contact thermal resistance between the CNT and the suspended membrane.

Using the fin heat transfer model (Yu, Saha *et al.* 2006), R_{CM} can be written as

$$R_{CM} = \frac{2\sqrt{R_{CNT/L} \cdot R_C^{'}}}{\tanh(L_C \sqrt{R_{CNT/L} / R_C^{'}})}, \tag{3.3}$$

where L_C is the length of the CNT segment in contact with the membrane, and $R_C^{'}$ is the contact thermal resistance for a unit length. When L_C is large enough so that the denominator in Eq. (3.3) can be approximated as unity, R_{CM} is no longer a function of L_C. In this case, we say that the CNT is fully thermalized with the supporting membrane. Because the function tanh(x) is already very close to unity for x = 2 (tanh(2) = 0.964), and approaches to unity slowly in an asymptotic manner after $x \geq 2$, we estimated the minimum contact length, $L_{C,\,min}$, required for the CNT to be fully thermalized with the suspended membranes by requiring $L_C \sqrt{R_{CNT/L} / R_C^{'}} = 2$. With this approximation, simple manipulation of Eq. (3.3) leads to $L_{C,\,min} \approx R_{CM}/R_{CNT/L}$. The calculated $L_{C,\,min}$ as the

average of the two sets of R_{CM} and $R_{CNT/L}$ is about 4 μm at 300 K and becomes smaller at lower temperature. In all our measurements with no EBID contact treatment, the actual L_C is larger than $L_{C,\,min}$, which means that R_{CM} is no longer a function of L_C. Therefore, the assumption we made previously that R_{CM} is the same in different measurements with no EBID contact treatment is reasonable. Taking the denominator in Eq. (3.3) as unity, $R_C^{'}$ can be expressed as $R_{CM}^2/(4R_{CNT/L})$ and at 300 K, $R_C^{'}$ is obtained as 5.9 m K W^{-1}, which is close to the lower end among the published data (Kim 2002; Maune, Chiu *et al.* 2006; Pop, Mann *et al.* 2006; Tsen, Donev *et al.* 2008; Shi, Zhou *et al.* 2009; Baloch, Voskanian *et al.* 2010).

If we assume that the contact thermal resistance for a unit area does not change with the tube diameter, then $R_C^{'}$ scales linearly with the contact width between the CNT and the substrate. The contact width between a MWCNT and a planar substrate through van der Waals interactions can be estimated as ~3.8 nm for a 66-nm-diameter MWCNT, and ~0.92 nm for a 10-nm-diameter MWCNT (Prasher 2008). Based on the $R_C^{'}$ value obtained here for the 66-nm-diameter tube, the $R_C^{'}$ for a 10-nm-diameter tube can be estimated as 24.4 m K W^{-1}. This value is about twice that obtained using scanning thermal microscopy between a 10-nm-diameter MWCNT and the SiO_2 substrate (12.5 m K W^{-1}) (Kim 2002), but it is much smaller than that estimated in some other references (Pettes and Shi 2009) (201–258 m K W^{-1}). One possible reason for this difference could be that in our measurement a large section of the CNT is in contact with Pt, while in the reported CNT–substrate contact thermal resistance in the reference (Kim 2002), the substrate is SiO_2.

Li *et al.* (Li, Liu *et al.* 2009) studied thermal boundary resistances (TBR) of CNTs in contact with metals and polymers and found that CNT/polymer generally gives a lower TBR compared to the CNT/metal. However, in their study, relative TBR was obtained for comparison between different metals and polymers, no absolute value of the contact thermal resistance between a CNT and metal or polymer was given. While contact thermal resistance between CNTs and metal substrates is not available in the literature, there have been several reports of contact thermal resistance between graphite and different metal substrates. As pointed out by Prasher (Prasher 2008), the thermal behavior of MWCNTs should be similar to that of graphite. Therefore, it is interesting to compare the contact thermal resistance obtained here with those between graphite and different metal substrates. Based on the contact width (3.8 nm) and the derived $R_C^{'}$ (5.9 m K W^{-1}), the contact thermal resistance for unit area for the CNT and suspended membranes can be calculated as 2.2 $\times 10^{-8}$ m^2 K W^{-1} at 300 K. This value is about three times larger than the theoretical prediction (6.3 $\times 10^{-9}$ m^2 K W^{-1}) between platinum and the graphite basal plane near room temperature (Prasher 2008; Pettes and Shi 2009), and comparable to the measured contact thermal resistance between *c*-axis-oriented highly ordered pyrolytic graphite (HOPG) and several metals (Schmidt, Collins *et al.* 2010). Our result is also comparable to the contact thermal resistance between silicon dioxide and single-layer and multilayer graphene sheets in the range of 5.6 $\times 10^{-9}$ – 1.2 $\times 10^{-8}$ m^2 K W^{-1} at room temperature (Chen, Jang *et al.* 2009).

Based on **Figure 3.1**, the length of the CNT segment on the Pt electrode of each suspended membrane is less than the minimum length required for the CNT to be fully thermalized with the membranes, and the CNT is also in contact with other parts of the

suspended membrane composed of SiO_2 and SiN_x. Based on the fin model, up to 25% of heat is transferred to or from the CNT off the Pt surface. It is worth noting that some experimental error can be introduced from the different lengths of the CNT-Pt and CNT-SiN_x/SiO_2 contacts in different measurements. However, because for all three CNT configurations, over 75% heat is transferred through the sample-Pt contacts, and the nature of contacts for both CNT-Pt and CNT-SiN_x/SiO_2 is van der Waals, we expect that the experimental error introduced should be a small fraction much less than 25%.

After the intrinsic thermal conductivity of the CNT is evaluated, the contact thermal resistance between the CNT and EBID gold can also be extracted. **Figure 3.2** shows that for the case with L_M = 4.4 μm, EBID of gold leads to an enhanced thermal conductance. Because the CNT configuration before and after the gold deposition is the same (**Figure 3.1(c)** and **3.1(d)**, respectively), the increase in the measured thermal conductance can be fully attributed to the decrease in the contact thermal resistance because of EBID gold deposition. Comparison of the total thermal resistance with and without the gold deposition yields a contact thermal resistance difference of 2.2×10^6 K W^{-1} at room temperature. This value is slightly smaller than the reduction in contact thermal resistance between a 152 nm diameter carbon nanofiber and the suspended membranes from the EBID of Pt reported in a reference (Yu, Saha *et al.* 2006) ($3 – 5 \times 10^6$ K W^{-1}). The contact thermal resistance after EBID of gold can be calculated by subtracting the intrinsic thermal resistance of the CNT segment between the two membranes from the measured total thermal resistance, which yields $3 – 4 \times 10^6$ K W^{-1} in the temperature range of 240 – 420 K. With gold deposition, the overall contact thermal resistance of each contact is composed of two parallel contact thermal resistances:

direct CNT-membrane contact thermal resistance, R_{CM1} (or R_{CM2}), and the CNT-membrane contact thermal resistance through the deposited gold, $R_{CM\text{-}Au1}$ (or $R_{CM\text{-}Au2}$), as shown in Figure **3.1(f)**. Considering the fact that gold is deposited from above, it is a reasonable assumption that only the upper half circumference of the CNT is covered by the gold. Therefore the contact area between the CNT and the gold can be estimated as $A_{C,\,Au} = L_{C,\,Au} \times \pi\, D/2$, where $L_{C,\,Au}$ is the length of the CNT-Au contact along the CNT axial direction, and D is the CNT diameter. The CNT-Au contact lengths measured from the SEM image are 0.35 and 0.47 μm for each side.

To obtain the contact thermal resistance for a unit area between the CNT and the EBID gold, we assume that the direct CNT-membrane contact thermal resistance R_{CM} is the same before and after the gold deposition. Since the CNT segment on each membrane is longer than the required minimum length for the CNT to be fully thermalized with the membrane, we further assume that R_{CM1} is equal to R_{CM2}. With these assumptions, based on the thermal resistance network shown in Figure **3.1(f)**, the contact thermal resistance between the CNT and the suspended membrane through the deposited gold for a unit area can be derived as 2.1×10^{-7} m^2 K W^{-1} at room temperature, which is one order of magnitude higher than the direct contact thermal resistance between the CNT and the suspended membrane (2.2×10^{-8} m^2 K W^{-1}). It is worth noting that the calculated contact thermal resistance between the CNT and the gold is an effective one including the contact thermal resistance between the CNT and the gold, the gold and the substrate, and the thermal resistance of the gold itself. Because of the low quality of the gold deposited using EBID (Utke, Hoffmann *et al.* 2000), the thermal resistance of the gold itself could be significant.

3.5 Uncertainty Analysis

The experimental uncertainty of the measured total thermal conductance derived from the electrical measurements has been evaluated using the Monte Carlo method (Coleman and Steele 2009), and the uncertainty is about 2% above 100 K. L_M is determined from the SEM images, in which the curved CNT is divided into several different segments, and its uncertainty is estimated conservatively as 0.3 μm. The diameter of the CNT is evaluated using TEM, and the uncertainty is assumed as 2 nm. Based on the uncertainties derived from these sources, the overall uncertainties of the intrinsic thermal conductivity and R_{CM} can be calculated following the standard approach of uncertainty propagation (Coleman and Steele 2009). At 300 K, the relative uncertainty of the intrinsic thermal conductivity is about 9%, and the relative uncertainty of R_{CM} is about 28%.

3.6 Summary

The intrinsic thermal conductivity of a MWCNT is significantly higher than the effective ones without eliminating the contact thermal resistance between the CNT and the heat source/sink. The result indicates that contact thermal resistance might be the reason for lower experimentally measured thermal conductivities than the theoretically predicted value. The experiment also suggests that EBID contact treatment can effectively reduce the contact thermal resistance. However, for nanowire/nanotube samples of high thermal conductance, it may not reduce the contact thermal resistance to a negligible level. The measured contact thermal resistance between the CNT and the

suspended membrane for a unit area is 2.2×10^{-8} m^2 K W^{-1} at 300 K, which provides important data for applications such as using CNT arrays as thermal interface materials.

4. INTRINSIC THERMAL CONDUCTIVITY OF SILICON NANORIBBONS

The thermal conductivity of low dimensional nanostructures, such as various nanotubes, nanowires and nanoribbons attracted significant attention in the past decade because boundary confinement effects could lead to promising properties for applications such as thermoelectrics (Volz and Chen 1999; Kim, Shi *et al.* 2001; Li, Wu *et al.* 2003; Li, Wu *et al.* 2003; Yu, Shi *et al.* 2005; Zhou, Jin *et al.* 2005; Pop, Mann *et al.* 2006; Boukai, Bunimovich *et al.* 2008; Chen, Hochbaum *et al.* 2008; Hochbaum, Chen *et al.* 2008). In addition, boundary confinement provides additional boundary conditions to understand complex phonon transport mechanisms in different materials (Mingo, Yang *et al.* 2003). Silicon nanowires/thin films, in particular, have been studied extensively because of the importance of silicon materials in semiconductor industry (Ju and Goodson 1999; Li, Wu *et al.* 2003; Liu and Asheghi 2005; Boukai, Bunimovich *et al.* 2008; Chen, Hochbaum *et al.* 2008; Hochbaum, Chen *et al.* 2008; Hippalgaonkar, Huang *et al.* 2010). Li *et al.* first measured the thermal conductivities of different diameter silicon nanowires, which showed significant thermal conductivity reduction from bulk values due to phonon-boundary scattering (Li, Wu *et al.* 2003). Later, thermal conductivities of thin silicon nanowires (Chen, Hochbaum *et al.* 2008) and rough silicon nanowires (Hochbaum, Chen *et al.* 2008) have been measured and disclosed more intriguing confinement effects. All these experimental studies on silicon nanowires were performed with the same measurement platform in which the sample was in contact with

two suspended membranes serving as a heat source and a heat sink, respectively. The contact thermal resistance between the sample and the suspended membranes renders the measured thermal conductivity an effective one, instead of the intrinsic properties of the silicon nanostructures. As such, the experimental data carry additional uncertainties difficult to estimate and prevent more accurate understanding of phonon transport through these nanostructures.

To eliminate the effect of contact thermal resistance, Hippalgaonkar *et al.* (Hippalgaonkar, Huang *et al.* 2010) modified the fabrication process of the suspended microdevice to integrate it with the fabrication of silicon nanowires with a rectangular cross-section. Their results showed that the monolithic contact within the device layer eliminated the contact resistance between the nanowires and the measurement device. However, this approach involves complex fabrication process and is difficult to be extended to other materials of interest. Alternatively, Mavrokefalos *et al* (Mavrokefalos, Nguyen *et al.* 2007; Mavrokefalos, Pettes *et al.* 2007) developed a four-probe thermal measurement scheme, which used the nanostructure sample itself as a differential thermocouple to determine the temperature drops at the contacts to quantify the contact thermal resistance. One limitation of this method is that the sample has to possess a relatively high Seebeck coefficient. As described in Chapter 3, we recently reported a scheme to extract the intrinsic thermal conductivity of nanostructures through multiple measurements of the same multi-walled carbon nanotube (MWCNT) with different suspended lengths between the heat source and the heat sink. This approach could also reveal the contact thermal resistance between the sample and the heat source/sink (Yang, Yang *et al.* 2011). Results showed that above 100 K, for a 66-nm-diameter MWCNT the

contact thermal resistance could contribute up to 50% of the total measured thermal resistance. Therefore, the intrinsic thermal conductivity of the MWCNT is significantly higher than the effective ones derived from a single measurement without eliminating the contact thermal resistance.

This chapter discusses measurements of intrinsic thermal conductivities of silicon nanoribbons of different geometrical dimensions fabricated using standard microfabrication techniques from silicon on insulator (SOI) wafers. Through multiple measurements of the same silicon nanoribbon with different lengths between the two suspended membranes as the heat source and the heat sink, the intrinsic thermal conductivity of the silicon nanoribbon has been extracted. Silicon nanoribbons of different dimensions have been fabricated and measured over a temperature range of 30 – 420 K. The measurement results indicate that due to the large interacting area from a flat contact between the ribbon and the suspended membranes, the contact thermal resistance is negligible. The experimental data suggest that it might take more than one parameter to characterize the simple phonon-boundary scattering effect.

4.1 Fabrication of silicon nanoribbons

Figure 4.1 shows the schematic of silicon nanoribbon fabrication process. It starts with 6″ (150 mm) diameter SOI wafers (p type Boron doped Si (100) with a dopant density of 0.7 – 1.5×10^{15} cm^{-3}, Simgui Technology Co., Ltd.) with 140 nm thick top device silicon layer and 500 nm buried oxide (BOX) layer. The SOI wafer first undergoes a dry oxidation process in an MRL Industries Furnace, after which the top silicon oxide layer is removed by a wet etching process with buffered oxide etch (BOE 6:1). As a

result, the thickness of the top device silicon layer is thinned down, which is then measured by an ellipsometry method.

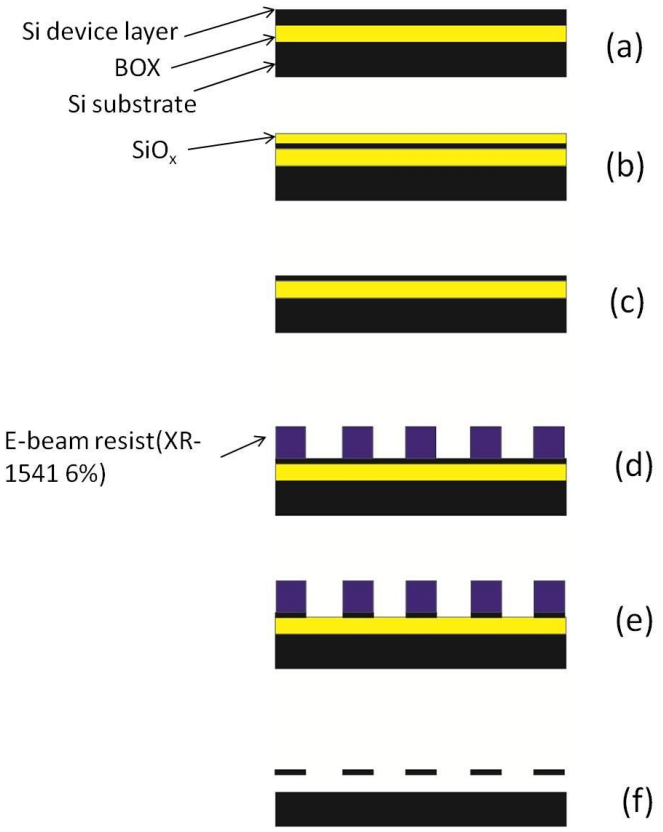

Figure 4.1 Schematic of silicon nanoribbon fabrication process. **(a)** SOI wafer (top device Si layer 140 nm, Buried Oxide (BOX) layer 500 nm), **(b)** Dry Oxidation of the silicon device layer, **(c)** Buffered Oxide Etch (BOE 6:1) to thin down top device Si layer, **(d)** E-beam lithography to pattern the ribbon structure, **(e)** Plasma etching to remove the uncovered Si layer, **(f)** Wet HF etch (10:1) and critical point dry to remove the E-beam resist and underneath BOX layer, releasing the nanoribbons into free-standing structures.

The 6″ SOI wafer is then cut into 30 × 30 mm pieces and spin-coated with Hydrogen Silsesquioxane (HSQ) E-beam resist (XR-1541 6%). XR-1541 HSQ is a

negative resist and also a flowable oxide, which provides high resolution and good etching resistance. Since the E-beam resist we used is an oxide, it can be stripped off by wet or vapor hydrofluoric acid (HF) etching. The HSQ covered SOI chips are then patterned using E-beam lithography (JEOL 6300) to form silicon ribbon structures. After developing the exposed resist, the uncovered top silicon device layer is etched by plasma etching (PlasmaTherm 770). Finally, wet hydrofluoric acid (HF) etching (10:1) and critical point dry is applied to remove the HSQ E-beam resist and the underneath BOX, releasing the silicon nanoribbons into free-standing ribbon structures.

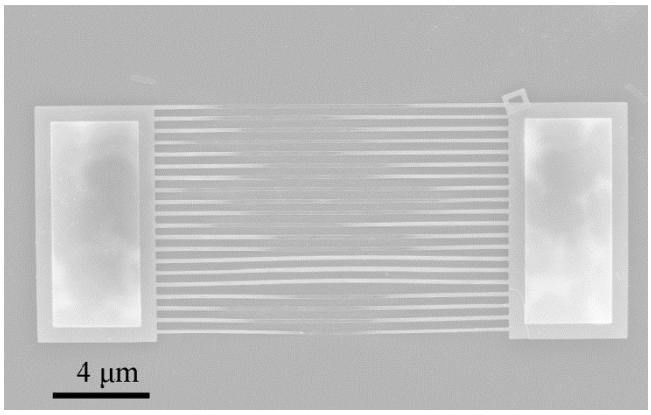

Figure 4.2 An SEM micrograph of fabricated silicon nanoribbons suspended between two rectangle shape anchors.

Figure 4.2 shows a typical Scanning Electron Microscopy (SEM) micrograph of the as-fabricated silicon nanoribbon arrays with ~30–40 nm thickness and ~150 nm width. The nanoribbon structures are suspended between two large silicon islands as the anchor. From **Figure 4.2** it can be seen that the sides of the two anchors are over etched and the middle section of some nanoribbons stuck to the substrate due to their large aspect ratio and thin thickness. Since wet hydrofluoric acid (HF) etching is isotropic, the observed

over etching indicates that the buried oxide layer under the silicon ribbons has been completely etched away and the ribbon structures are suspended. The fabrication process produces uniform silicon nanoribbons with a high yield of > 95%.

Figure 4.3 shows a high-resolution transmission electron microscopy (HRTEM) micrograph of an individual silicon nanoribbon. The nanoribbon elongated in the [110] direction has a single crystalline core and an amorphous surface layer.

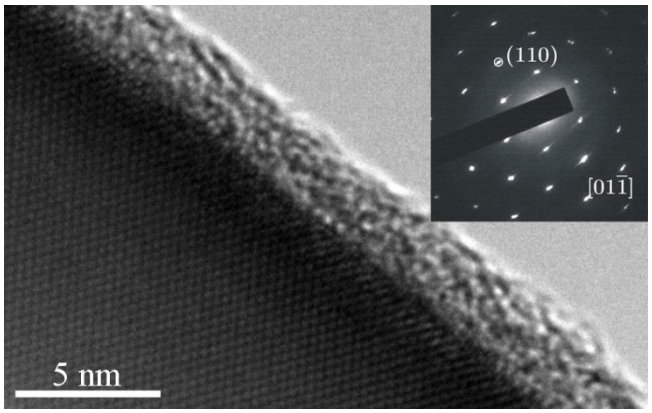

Figure 4.3 A high-resolution TEM micrograph of an individual single crystalline silicon nanoribbon. The inset shows a selected area electron diffraction pattern of the nanoribbon taken along [$01\bar{1}$] zone axis.

After the fabrication process, the silicon nanoribbon is transferred from the SOI chip to a piece of polydimethylsiloxane (PDMS) by a simple stamping process. It should be pointed out that it is critical to have the BOX layer underneath the two islands over etched as mentioned before, to reduce the contact area between islands and substrate otherwise the stamping transfer process will not be successful because the bonding strength between underneath silicon dioxide and silicon substrate is still large. An

individual silicon nanoribbon is then cut from anchors, picked up by a sharp tip mounted on the micromanipulator and transferred to the suspended microdevice. **Figure 4.4** is the schematic of the transfer and cutting process. **Figure 4.5** is the SEM micrograph of a silicon nanoribbon sample bridging the two suspended membranes of the microdevice.

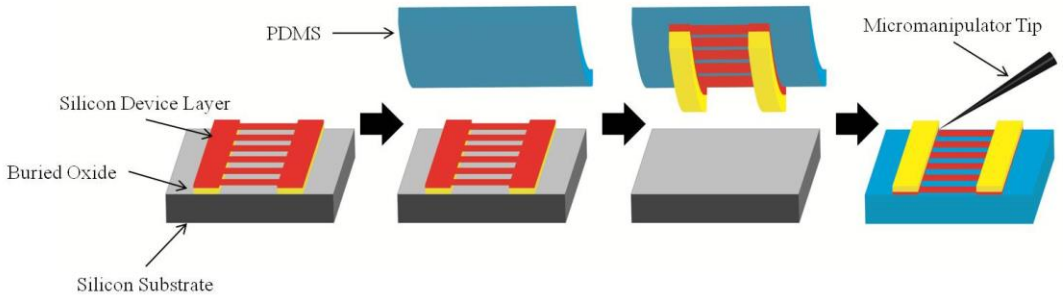

Figure 4.4 Schematic of silicon nanoribbon transfer and cutting process

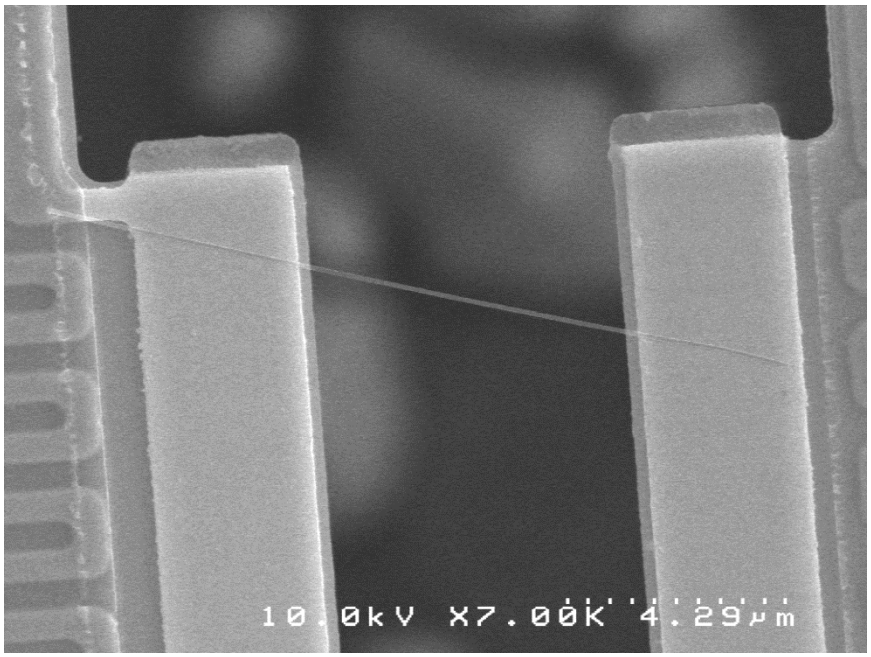

Figure 4.5 An SEM micrograph of an individual silicon nanoribbon bridging the two suspended membranes of the microdevice

4.2 Measurement Method

Same as described in Chapter 3, the measurements were performed with the suspended microdevices that have been discussed in details in Chapter 2. For intrinsic thermal conductivity measurement, each sample was measured three times. **Figure 4.6** shows the SEM micrographs of a 15 μm long, 25 nm thick, and 99 nm wide silicon nanoribbon placed in different configurations with different lengths (L_s) of ribbon segments between the two suspended membranes. The length and width of the nanoribbon was measured by SEM. After three times thermal measurements, the measured sample was transferred to a flat silicon surface and the thickness of the sample was measured by atomic force microscopy (AFM). For this specific sample, the three measurements were performed with the suspended length, L_s, as 6.14 μm (**Figure 4.6(a)**), 7.53 μm (**Figure 4.6(b)**), and 8.95 μm (**Figure 4.6(c)**), respectively.

Figure 4.6(d) shows the equivalent thermal resistance circuit. The total thermal resistance, R_{tot}, is composed of three components, the intrinsic thermal resistance of the silicon nanoribbon, R_{SiNR}, and the contact thermal resistance between the silicon nanoribbon and the two membranes, R_{SiM1} and R_{SiM2}. The total contact thermal resistance, R_{SiM}, is the sum of R_{SiM1} and R_{SiM2}. Therefore, R_{tot} can be written as

$$R_{tot} = R_{SiM} + R_{SiNR} = R_{SiM} + R_{SiNR/L} \times L_s , \tag{4.1}$$

where $R_{SiNR/L}$ is the intrinsic thermal resistance of the silicon nanoribbon per unit length. As has been discussed in the CNT measurement, we assume that R_{SiM} remains unchanged in different measurements, which will be justified later.

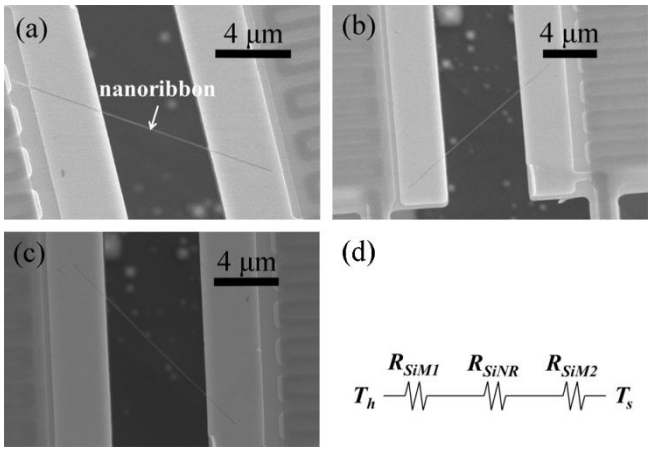

Figure 4.6 (a-c) SEM micrographs of a Si nanoribbon sample and **(d)** the corresponding thermal resistance circuit. The suspended length of the silicon nanoribbon between the two membranes is measured as (a) 6.14 μm (b) 7.53 μm (c) 8.95 μm.

4.3 Results and Discussion

The measured total thermal conductance G_s (*e.g.* $1/R_{tot}$), is given in **Figure 4.7** as a function of temperature for the three different measurements. It can be seen that G_s decreases as L_s increases, due to the fact that the longer the suspended length L_s is, the larger the intrinsic thermal resistance of the Si nanoribbon, R_{SiNR}, is. According to Eq. (4.1), larger R_{SiNR} corresponds to higher R_{tot}, and hence lower G_s. The uncertainty of the electrical measurements was evaluated using a Monte Carlo Method (Coleman and Steele 2009). The uncertainties of the ribbon length, width and thickness measurements were estimated conservatively as 0.2 μm, 5 nm and 2 nm, respectively. And the overall uncertainty was calculated following the standard uncertainty propagation equation (Coleman and Steele 2009), as shown for selected data points in **Figure 4.7**.

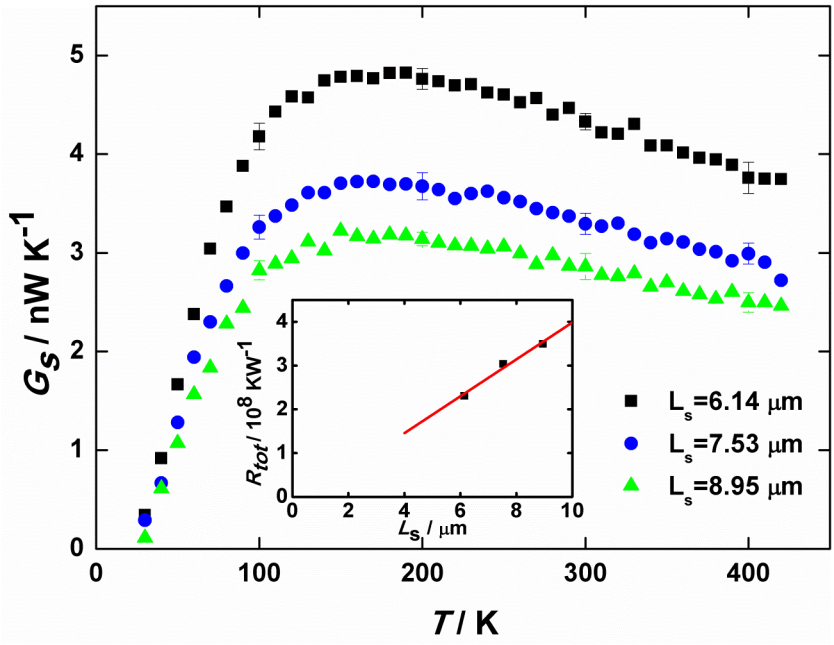

Figure 4.7 Measured total thermal conductance (R_{tot}) as a function of temperature for three different suspended lengths (L_s) of the Si nanoribbon shown in Figure 4.6. The inset shows the linear relation between R_{tot} and L_s at 300 K.

To extract the intrinsic thermal conductivity and contact thermal resistance from Eq. (4.1), we assumed that R_{SiM} remains unchanged for different measurements. If this is correct, the total thermal resistance, R_{tot}, should be linearly proportional to the suspended length, L_s. This has been verified to be exactly the case as shown in the inset of **Figure 4.7**, which plots R_{tot} as a function of L_s at 300 K. Similar linear relationship was also found at other temperatures.

Figure 4.8 shows the extracted effective thermal conductivity of the silicon nanoribbon from three different measurements. It can be seen that the effective thermal conductivities of the three different measurements nearly overlap with each other over the whole temperature range (30K – 420K), which means that the effective thermal

conductivity is very close to the intrinsic thermal conductivity and the contact thermal resistance is negligible. This is very different from the case for MWCNTs (Yang, Yang *et al.* 2011), which has a quasi-line contact with the membrane and the contact makes a significant contribution to the measured total thermal resistance. The silicon nanoribbon here, on the other hand, makes a flat contact with the suspended membranes, which has a much larger interaction area, and hence much smaller contact thermal resistance. It is worth noting that in our studies of boron nanoribbon thermal conductivity, we also observed that a flat contact between nanoribbons and suspended membranes could lead to negligible contact thermal resistance (Yang, Yang *et al.* 2012). In fact, the fitting line in the inset of **Figure 4.7** almost extrapolates to the original point, which also indicates a negligible contact thermal resistance. Therefore, the averaged effective thermal conductivity can be regarded as the intrinsic thermal conductivity of this silicon nanoribbon.

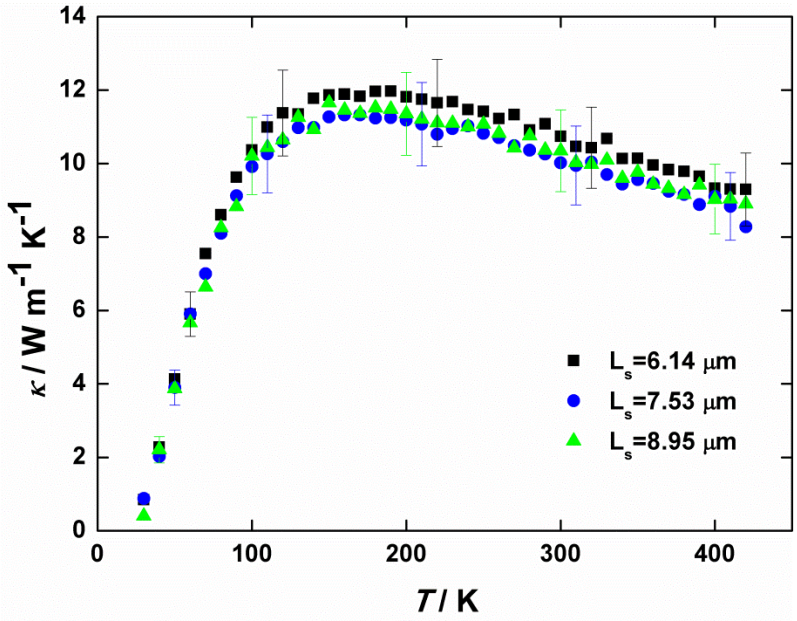

Figure 4.8 Measured effective thermal conductivities as a function of temperature for three different suspended lengths of the Si nanoribbon shown in Figure 4.6.

Following the same procedure, silicon nanoribbons of different widths and thicknesses were each measured three times with three different L_s. It is verified that contact thermal resistance is negligible for each sample and the average thermal conductivity of different measurements is taken as the intrinsic thermal conductivity of the silicon nanoribbon. **Figure 4.9** plots the intrinsic thermal conductivity of different silicon nanoribbons over the temperature range of 30–420 K. In general, the measured intrinsic thermal conductivities are much lower than the corresponding bulk value, which can be attributed to the strong phonon boundary scattering (Li, Wu *et al.* 2003; Chen, Hochbaum *et al.* 2008; Hippalgaonkar, Huang *et al.* 2010).

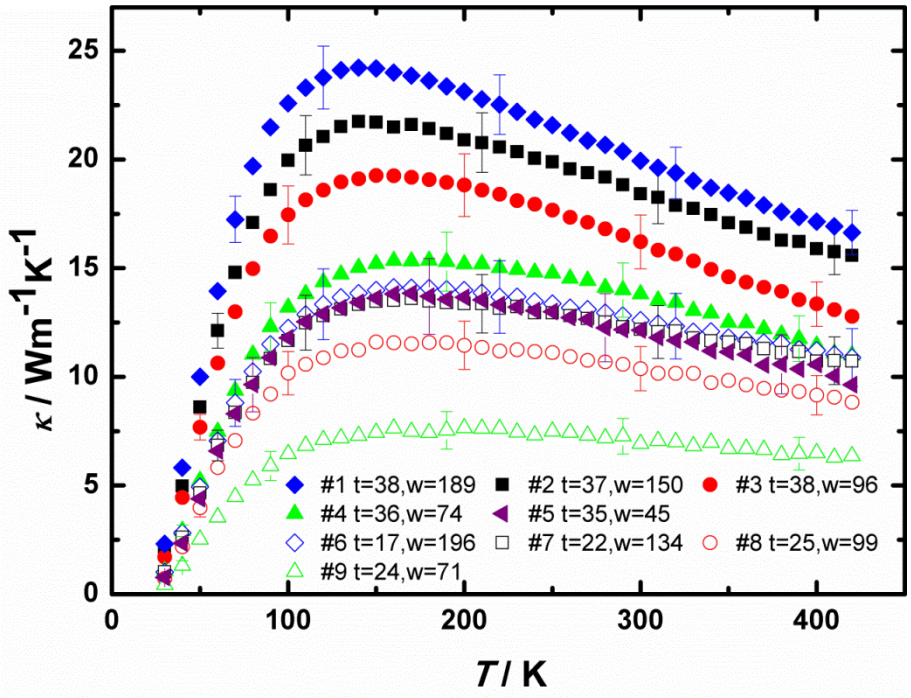

Figure 4.9 Measured intrinsic thermal conductivities of silicon nanoribbons with different thicknesses and widths.

In **Figure 4.9**, the nine measured samples can be roughly divided into two groups based on their thickness (group 1: sample #1–5 with thickness from 35–38 nm and group 2: sample #6–9 with thickness from 17–25 nm), as represented by solid and empty symbols in the figure, respectively. For both groups, over the measured temperature domain, as the width decreases, the intrinsic thermal conductivity decreases. In fact, if we neglect the thickness difference for ribbons in group 1, the room-temperature thermal conductivities drop from 19.94 W/m-K to 12.15 W/m-K as the width reduces from 189 nm to 45 nm, a very significant reduction. More importantly, the thermal conductivity of the ribbon with a cross-sectional dimension of 17 nm thick and 196 nm wide is nearly the same as or slightly higher than that of the ribbon with a cross-sectional dimension of 35 nm thick and 45 nm wide. This is interesting because one common practice in evaluating the phonon-boundary scattering effects is to use the Matthiessen's rule with the lowest lateral dimension as the dominant factor in phonon boundary scattering. Our results, however, clearly indicate that in addition to the lowest lateral dimension, i.e. the thickness of the silicon nanoribbon in our case, the other lateral dimension also plays an important role in thermal transport. This is true even when the aspect ratio of width/thickness is larger than 10, as shown in **Figure 4.9**.

For all the measured samples, as the temperature increases, the intrinsic thermal conductivities increases to a peak value and then decreases, showing signatures of Umklapp scattering. As the ribbon width decreases, the peak temperature shifts to higher values, which further supports the observation that the relatively large lateral dimension is also important in phonon boundary scattering.

Amorphous oxide layer generally exists on the surface of silicon nanostructures, which makes the actual cross-sectional area of the silicon core smaller and introduces additional interfaces in the nanostructures. For example, a recent MD simulation showed that for a silicon nanowire with a diameter of 15 nm, the thicker the surface amorphous layer, the lower the thermal conductivity (He and Galli 2012). From **Figure 4.3** it is clearly seen that there is a roughly 2 nm thick non-crystalline amorphous oxide layer outside the single crystalline silicon core. We further examined several nanoribbons of different thicknesses and widths and found that the amorphous layer thickness can vary from about 1 nm to slightly more than 3 nm. Compared with chemically synthesized silicon nanowires, which normally has only ~1 nm thick amorphous oxide layer, the oxide layer thickness of the fabricated silicon nanoribbons varies and can be significantly thicker. One possible reason for this could be the difference in induced stress from the oxide for the planar and circular cross-sections. To consider the uncertainties from the amorphous layer thickness and further study the intrinsic thermal conductivities of the single crystalline silicon nanoribbon core, we use an average amorphous layer thickness of 2 nm and subtract the contribution of the amorphous shell (use the thermal conductivity of bulk amorphous silicon dioxide (Cahill) as the thermal conductivity of amorphous shell here) from the total thermal conductance of the nanoribbon. Based on the extracted thermal conductance of the crystalline silicon core and reduced dimension, the intrinsic thermal conductivity of the silicon core can be derived, as shown in **Figure 4.10**. It is worth noting that due to the additional uncertainty source of the oxide thickness, and hence the ribbon core thickness, the overall uncertainty for each data point gets larger.

For example, the estimated overall uncertainty for the thinnest silicon nanoribbon (sample #6) can be as high as ~23%.

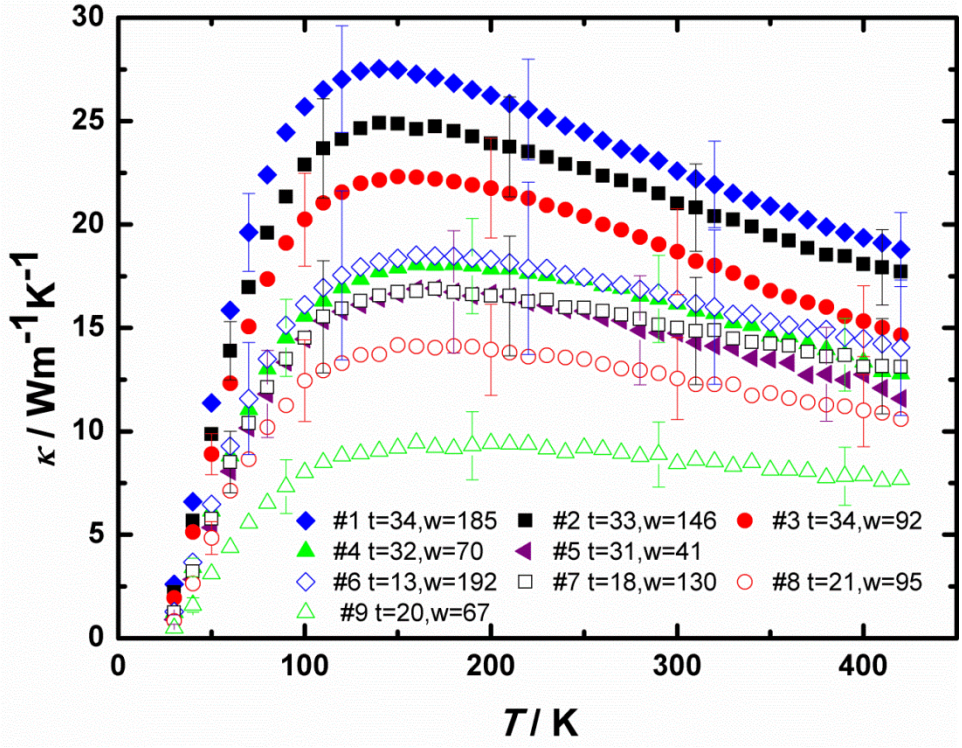

Figure 4.10 Measured intrinsic thermal conductivities of single crystalline cores of the silicon nanoribbons.

The Casimir length (L_C) has been widely used to quantify the size-dependent thermal conductivities of nanostructures (Casimir 1938). For nanowires with a rectangular cross section, if assuming a perfectly rough surface that scatters phonon diffusely, then L_C can be expressed as:(Lü, Chu *et al.* 2003; Hippalgaonkar, Huang *et al.* 2010)

$$L_C = 2\frac{\sqrt{wt}}{\sqrt{\pi}}, \tag{4.2}$$

where w and t are the width and thickness of the nanowire, respectively. We use Eq. (4.2) to calculate the L_C of our measured nanoribbon samples and compare their room temperature intrinsic thermal conductivities with several previously reported experimental data on confined silicon nanostructures (Hippalgaonkar, Huang *et al.* 2010). as shown in **Figure 4.11**. As expected, our measured intrinsic thermal conductivities of silicon nanoribbons are still smaller than the in-plane thermal conductivities of thin silicon films (Liu and Asheghi 2005) since thin films are confined only in the thickness direction. Similar to thermal conductivities of integrated rectangular silicon nanowires reported in Ref. (Hippalgaonkar, Huang *et al.* 2010), our results sit between the Vapor-Liquid-Solid (VLS) grown silicon nanowires (Li, Wu *et al.* 2003) and electrolessly etched (EE) silicon nanowires (Hochbaum, Chen *et al.* 2008). We believe that the thermal conductivity is lower than the VLS silicon nanowires most probably because the fabricated ribbons are from doped SOI wafers; and therefore, the dopants provide additional scattering to reduce the thermal conductivity. In addition, some damage from the plasma etching process (mainly to the side wall of the ribbons) cannot be fully ruled out at this stage, either.

It can be seen that for samples in either group 1 or group 2, their thermal conductivities follow the general trend of increasing with the Casimir length, respectively. However, it is very interesting to see that this trend is not true if we combine all samples in group 1 and group 2, that is, the thermal conductivity does not always increase with the Casimir length. In fact, if doing linear fit for the two groups of data, the increasing trend follows two different slopes for the two different groups, as shown in **Figure 4.11**. This interesting observation suggests that in addition to the Casimir length, the lowest lateral

dimension and the cross-sectional aspect ratio both can play a role in determining the thermal conductivity of nanostructures. Therefore, for nanostructure with a non-circular or non-square cross-section, even the simple classical size effect could be very intriguing.

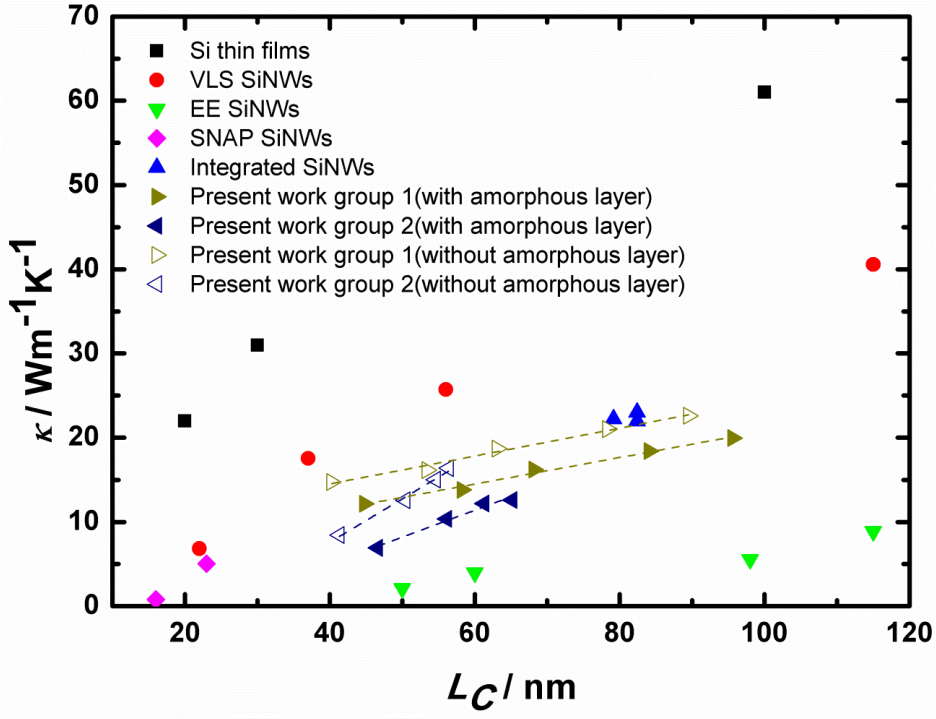

Figure 4.11 Room temperature (300 K) thermal conductivities of confined silicon structures as a function of Casimir length (L_C).

4.4 Summary

We have measured the intrinsic thermal conductivities of micro-fabricated individual silicon nanoribbons with different thicknesses and widths. Due to the relatively large flat contact area between the nanoribbons and heat source/sink, the contact thermal resistance is negligible. The dependence of the thermal conductivity on the Casimir length suggests that in addition to the Casimir length, the lowest characteristic dimension

size and the aspect ratio could both play important roles in determining thermal transport through nanoribbons of rectangular cross-section.

5. THERMAL CONDUCTIVITY OF BORON CARBIDE NANOWIRES

Boron Carbides (B_xC) have been historically utilized as abrasives and armor owing to their extreme hardness. In addition, the large neutron capture cross-section of the ^{10}B nucleus makes boron carbides ideal absorption material for nuclear energy applications (Medwick, Fischer *et al.* 1994). More recently, boron carbides have attracted some attention as high temperature thermoelectric materials because of their chemical stability at high temperature and substantial thermopowers (Bouchacourt and Thevenot 1985; Wood 1986; Medwick, Fischer *et al.* 1994; Aselage, Emin *et al.* 1998; Emin 2006). Meanwhile, recent research on nanostructured thermoelectric materials, such as nanowires (Boukai, Bunimovich *et al.* 2008; Hochbaum, Chen *et al.* 2008), superlattices (Venkatasubramanian, Siivola *et al.* 2001; Harman, Taylor *et al.* 2002) and nanocomposites (Poudel, Hao *et al.* 2008), has achieved significant improvement on thermoelectric figures of merit *ZT* compared with their bulk counter-parts. Therefore, it is of great interest to investigate thermal transport and thermoelectric properties of nanostructured boron carbides based materials.

In a wide range of compositions: from $B_{10.4}C$ (8.8 at.% C) to B_4C (20 at.% C), boron carbides exists as a rhombohedral structure (Matkovich 1977; Wood, Emin *et al.* 1985). This structure consists of 8 deformed 12-atom icosahedra located at the corners of the rhombohedral unit cell. There are direct bonds between the icosahedra. In addition, icosahedra are linked by 3-atom chain along the longest diagonal of the rhombohedron.

Carbon atoms generally reside in the boron carbides as constituents of the 3-atom chain, which make it CBC, CBB, B□B (□, vacancy) or sometimes CCC arrangements (Wood, Emin *et al.* 1985; Werheit 2006). They can also substitute for 1 of the 12 boron atoms within the icosahedra ($B_{11}C$). The variation of carbon content within the homogeneity range could lead to the presence of highly concentrated intrinsic structural defects in boron carbides (*e.g.*, ~ 9.3% in $B_{13}C_2$) (Schmechel and Werheit 1999). Such defects, in the form of incomplete occupation of specific sites or of antisite defects could greatly influence the transport properties. During the past decades, some efforts have been made to understand both the electrical and thermal transport process in boron carbides. However, most of the research is carried on bulk polycrystalline specimens prepared by melting or hot pressing (Werheit, Leithe-Jasper *et al.* 2004), which severely suffers from sample-to-sample variations. We have measured thermal conductivities of boron carbide nanowires to investigate thermal transport phenomena in low-dimensional boron carbides.

5.1 Synthesizing and characterization of boron carbides nanowires

Boron carbide nanowires were synthesized by co-pyrolysis of B_2H_6 and CH_4 at elevated temperatures in a LPCVD system. Detail description of the LPCVD system can be found elsewhere (Xu, Zheng *et al.* 2004; Amin, Li *et al.* 2009). It begins with cleaned silicon pieces coated by a 2 nm-thick nickel (Ni) thin film using magnetron sputtering (Denton Vacuum: Desk IV TSC). The coated substrates were loaded into a quartz boat, which was subsequently placed in a desired position in the quartz tube of the LPCVD system. The whole system was first evacuated to a pressure of ~7 mTorr. After which the quartz tube was ramped up to 1050 °C (center position temperature measured outside the

quartz tube by a thermocouple) in 50 minutes. A constant flow of 15 sccm (standard cubic centimeters per minute) Ar (Linde: 99.999% UHP) was maintained during the whole experiment. To synthesize boron carbide nanowires, 15 sccm B_2H_6 (Voltaix; 5% UHP B_2H_6 in research grade Ar) and 15 sccm CH_4 (Linde Gas; compressed methane) were introduced to the quartz tube for 45 minutes at 1050 °C. The typical reaction pressure was ~440 mTorr. After reaction, the quartz tube was cooled down to room temperature naturally in ~5 hours.

Figure 5.1(a) is an SEM image of as-synthesized nanowires having diameters between 15 and 90 nm and lengths up to 10 μm. Typical transmission electron microscopy (TEM) results are presented in **Figure 5.1(b)**. Inset I in **Figure 5.1(b)** is a low magnification TEM micrograph of a part of a nanowire. The catalytic material at the tip of the nanowire is clearly revealed. The HRTEM image (**Figure 5.1(b))** of the area enclosed by the black rectangle in inset I shows that the nanowire has a single crystalline core and a 0.5 – 2 nm thick amorphous sheath. The image also reveals the existence of planar defects such as twins and stacking faults in the nanowire. Inset II is the corresponding selected area electron diffraction pattern recorded along the $[12\bar{1}]_h$ zone axis. (Note: the subscript *h* refers to the hexagonal representation.) The streaks in the diffraction pattern further confirm the existence of planar defects in the nanowire. On the basis of the HRTEM imaging and electron diffraction pattern analysis, the nanowire was found to have a rhombohedral boron carbide lattice. As previously mentioned, within homogeneous range, there are phases of various ratios between boron and carbon content such as B_4C, $B_{10}C$ and $B_{13}C_2$. Based on the TEM results, it is difficult to accurately distinguish phases between various boron carbides. However, according to the Joint

Committee on Powder Diffraction Standards (JCPDS) database, the calculated lattice constants for this particular nanowire are closer to values for $B_{13.7}C_{1.48}$ according to the JCPDS 01-071-0363. The preferred growth direction of the nanowire was found to be perpendicular to the $(101)_h$ plane. (Note: the subscript *h* refers to the hexagonal representation. $(101)_h$ is equivalent to $(100)_r$, where *r* refers to the rhombohedral representation.) Among all nanowires analyzed, approximately 75% were grown perpendicular to the $(101)_h$ plane.

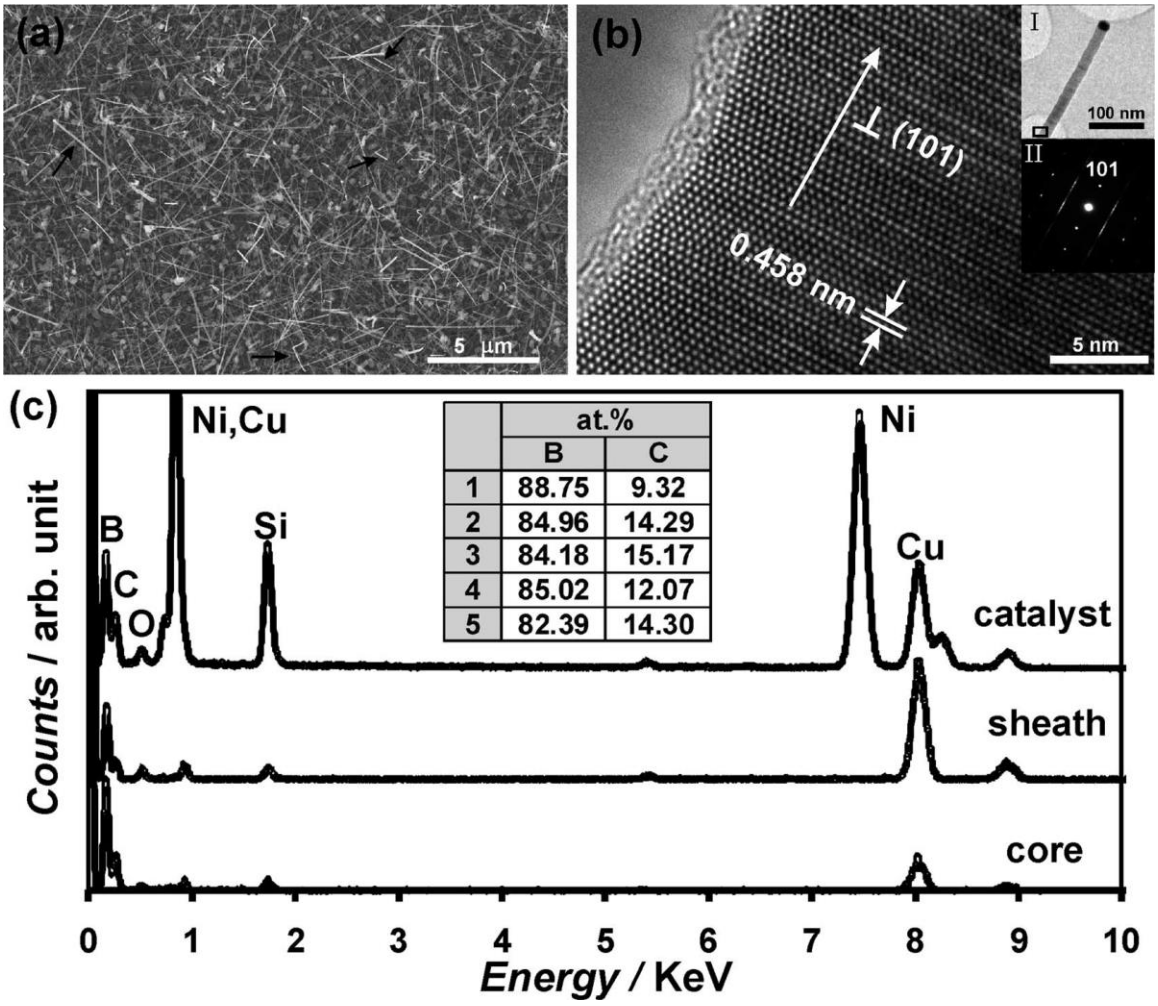

	at.%	
	B	C
1	88.75	9.32
2	84.96	14.29
3	84.18	15.17
4	85.02	12.07
5	82.39	14.30

Figure 5.1 Materials characterization of as-synthesized nanowires. **(a)** An SEM image shows both straight and kinked nanowires (pointed by black arrows). **(b)** TEM results

show the nanowire has a single crystalline core and a 0.5–2 nm thick amorphous oxide sheath. The preferred growth direction of the nanowire is perpendicular to $(101)_h$ planes. **(c)** EDS results show the compositional information within the core, sheath and catalyst of a nanowire. The inset is lists the atomic percentage of B and C in five different wires.

Figure 5.1(c) reveals the EDS results of compositional information in the core, sheath and tip of the nanowire. The existence of B, C, O and Si was found in both the core and sheath. (Note: the Cu signal comes from the supporting Cu grid and is not a component of the nanowire.) The higher O : B (or O : C) ratio observed from the sheath indicates that the periphery of the nanowire is rich in O. The inset shows the results from semi-quantitative analysis of atomic percentage of B and C in cores of five nanowires. Variation of compositions among nanowires is revealed, although all nanowires have the rhombohedral lattice. This observation is consistent with the fact that boron carbide is a solid solution with carbon atomic percentage varying between 8.8% and 20% and cannot be described by a simple fixed chemical formula (although B_4C is being widely used as the chemical formula of boron carbide). The catalytic material is composed of B, C, O, Ni and Si. A very small amount of Si exists in both the core and the sheath. The source of Si was discussed in Ref. (Xu, Nicholls *et al.* 2006). In general, the Si might come from the SiO_2/Si substrates, quartz boats and quartz tubes used for LPCVD synthesis.

5.2 Planar defects in as-synthesized boron carbides nanowires

The crystal structure of boron carbides can be viewed as a rhombohedral distortion of the cubic close packing (ccp) of B_{12} or $B_{11}C$ icosahedra (Matkovich 1977).

The {100} planes of the rhombohedral cell are considered as the close-packed planes in the ccp arrangement. They are stacked by a sequence of…ABCABC…as illustrated in **Figure 5.2(a)**. If this normal stacking sequence is disturbed, planar defects such as stacking faults and twins can be formed. Due to its relatively low stacking fault energy (75 ergs cm^{-2}) (Ashbee 1971), twins and stacking faults are commonly observed in bulk boron carbides, such as sintered samples and boron carbide particle reinforced metal matrix composites (Guan, Gutu *et al.* 2012). The introduction of a $(101)_h$ twin plane through the icosahedron distorts the inter- and intra-icosahedral bonding, which could lead to increased bipolaron hopping and affect relevant transport properties. Twins formed in bulk boron carbides are usually deformation twins. Their formation can be partly attributed to the localized stress state induced during complicated synthesis processes (*e.g.*, milling, hot pressing).

More than ninety nanowires were carefully examined by TEM. To reveal whether the nanowires have structural defects or not, wide angle of tilting was done on each nanowire during TEM examination. 75% of examined nanowires were found to have $\{101\}_h$-type planar faults. Based on the geometrical relationship between the fault plane and the preferred growth direction of the nanowire, the faults can be categorized into transverse faults (fault plane perpendicular to the nanowire preferred growth direction) and axial faults (fault plane parallel to the nanowire preferred growth direction). **Figure 5.2(b)** and **(c)** show a nanowire with transverse faults in which variable width twins and stacking faults are revealed. The faults have atomic sharp boundaries, indicating they are not deformation faults but growth faults. The white line helps the visualization of the zigzag facets on the wire side surface. These facets are $(1\bar{1}\bar{1})_h$ planes. The marked

rotation angle is approximately 146°, twice the interplanar angle between $(101)_h$ and $(1\bar{1}\bar{1})_h$ planes (=73°). The two crystallographic equivalent planes, $(101)_h$ and $(1\bar{1}\bar{1})_h$, have the highest planar density in the rhombohedral lattice. Therefore, they have the lowest surface energy and can be energetically more favorable to form during growth. For a portion of the nanowire, the disturbance of stacking sequence is labeled. The new stacking sequence is ABCBABABCA/CABC where the representative microtwinned region is underlined and one intrinsic stacking fault is illustrated by /. **Figure 5.2(d)** and **(e)** show a nanowire with axial faults. Similar to the aforementioned transverse faults, these axial faults consisted of variable-width twins and stacking faults. The side surfaces are $(101)_h$ planes.

5.3 Thermal conductivities of bulk boron carbides

Most of the reported experimental investigations on bulk boron carbides were performed on polycrystalline material obtained by melting or hot pressing (Werheit, Leithe-Jasper *et al.* 2004). Their thermal diffusivities (α) and specific heats (C_p) were experimentally got and the thermal conductivities (κ) were obtained from the relationship $\kappa = C_p \alpha \rho$, where ρ is the sample densities. **Figure 5.3** shows experimental results of the thermal conductivity (κ) of bulk boron carbides as a function of temperature (T) got by Wood *et al*. (Wood, Emin *et al.* 1985). As shown in **Figure 5.3**, boron carbide with the highest carbon concentration (B_4C) also has the highest thermal conductivity and it's a decreasing function of temperature, which is a characteristic temperature dependence of a crystal. By contrast, the thermal conductivities of boron carbides with lower carbon

concentrations are much smaller and show much weaker temperature dependences, which is similar to the behavior of glasses.

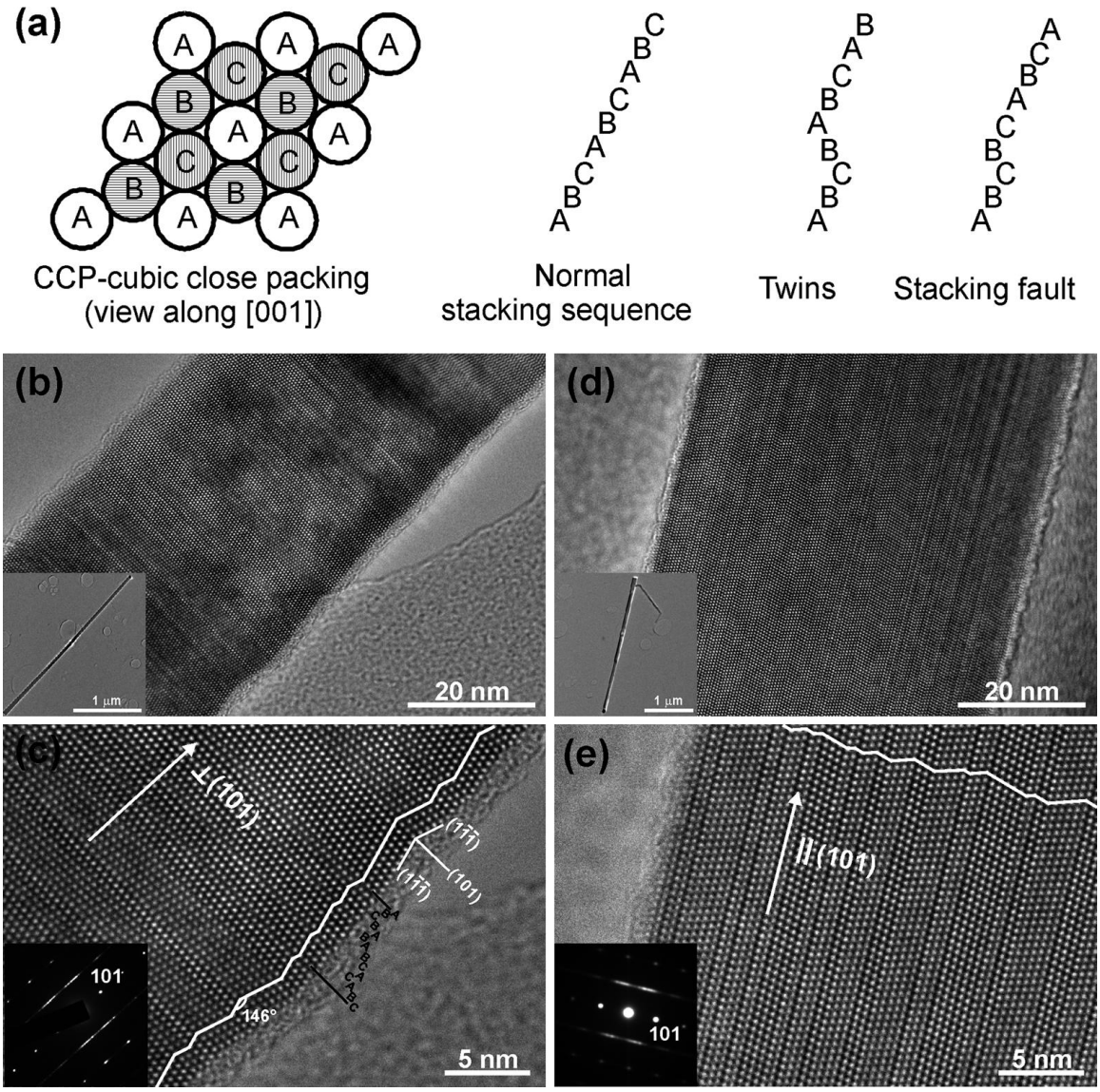

Figure 5.2 Study of planar defects in as-synthesized nanowires. **(a)** Schematic drawings show the ccp arrangement for a rhombohedral boron carbide structure, normal stacking sequence, twins and stacking faults induced by disordered stacking. (**b** and **c**) TEM results show the existence of transverse faults. (**d** and **e**) TEM results show the existence of axial faults.

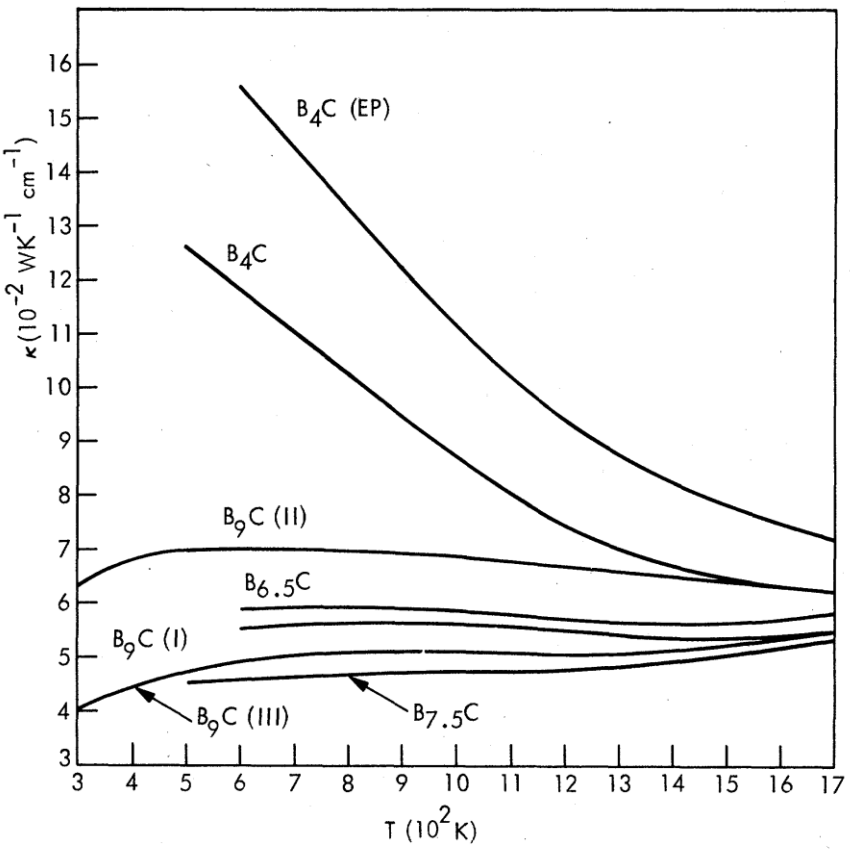

Figure 5.3 The thermal conductivity of boron carbides as a function of temperature (Wood, Emin *et al.* 1985).

Emin proposed a hopping type of thermal conduction mechanism in which the predominant transport of energy is through the intericosahedral chains (Medwick, Fischer *et al.* 1994). In this picture, the central atom of the chain provides weak coupling between anharmonic oscillators localized at the ends of the chains. One possible choice for such a vibrational unit would be the end atoms of a chain and the three icosahedral atoms connected to it. As the carbon content of the lattice varies, the bonding between atoms in the vibrational unit changes, which further causes vibrational frequencies shift of these units. Ideally, at the high-carbon end of the single-phase region (B_4C), all available

intericosahedral chain positions are filled by CBC chains, thus the two stiff vibrational units on both sides of the chain have same or similar bonding situation (depending on the icosahedral atoms they connect), which is preferable for energy transfer. In contrast, for carbon-poor boron carbides, only a fraction of the available chain locations are filled, or different types of atoms reside at opposite ends of the chain (CBB), all lead to larger frequency disparity of two vibrational units at two ends of the chain, which lower the thermal conductivity significantly.

There is one study on thermal conductivity of bulk single crystalline B_4C prepared by a Floating Zone method (Gunjishima, Akashi *et al.* 2001), as shown in **Figure 5.4**. As expected, the obtained thermal conductivity of single crystalline B_4C was the highest among the reported values from room temperature to about 1100 K. According to Emin's theory (Wood, Emin *et al.* 1985), in boron carbides, the electronic transport represents a very distinctive type of small polaron hopping. The average energy carried with a hopping carrier, E_T, is $C(kT)^2$, where the constant C is defined by $C \equiv zJ^2/16E_b^3$, z is the number of nearest neighbors, J is the intersite transfer energy, and E_b is the small bipolaron binding energy characterizing an average $B_{11}C$ icosahedron. Therefore, the transported energy increases with temperature. The electronic contribution to the thermal conductivity is a product of this energy E_T, the electronic diffusion constant D, and the rate of change of the carrier density with temperature (dn/dT), i.e., $\kappa_T = E_T D(dn/dT)$. This yields a very small electronic contribution to the total thermal conductivity. Therefore the major channel of thermal transport in boron carbides is lattice vibration. This explains the higher thermal conductivity in single crystalline boron carbides since

there is no grain boundary, which scatters phonons in polycrystalline samples and leads to lower thermal conductivity.

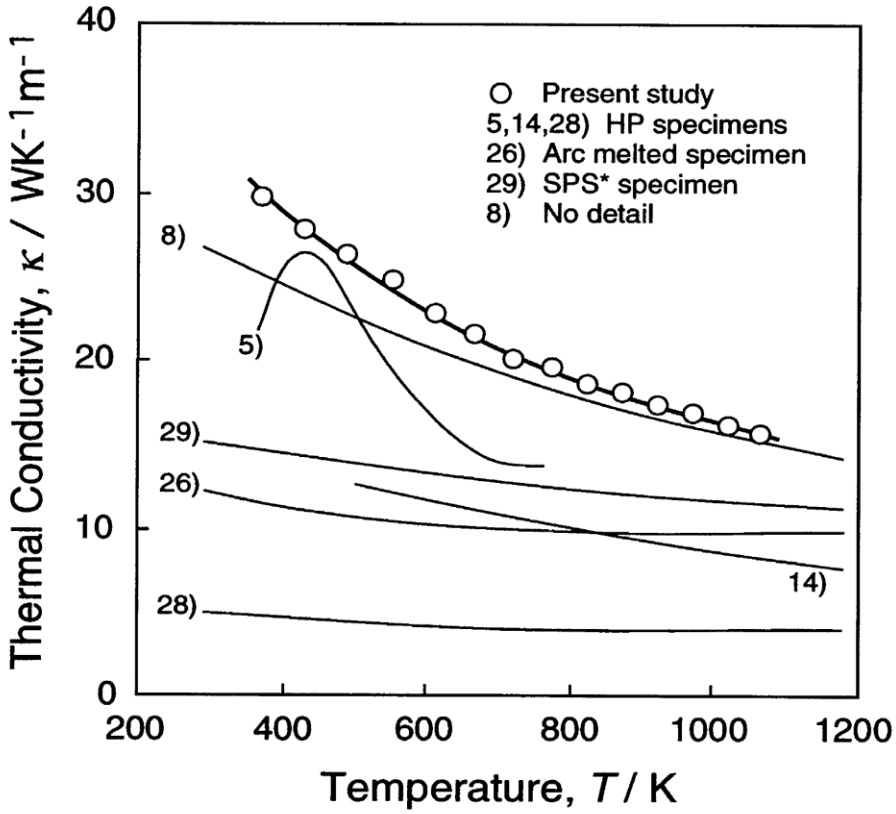

Figure 5.4 Temperature dependence of thermal conductivity (κ) of B_4C (Gunjishima, Akashi *et al.* 2001).

5.4 Sample preparation

The synthesized boron carbide nanowires were first transferred from the silicon chip to a piece of polydimethylsiloxane (PDMS) by stamping, as in the silicon nanoribbon case. An individual boron carbide nanowire is then picked up by a sharp tip mounted on a micromanipulator and transferred to the suspended microdevice.

Due to the likely low intrinsic thermal conductivity of individual boron carbide nanowires and very large contact thermal resistance between individual boron carbide nanowires and Pt electrodes, if no treatment was made to enhance the thermal conductance at the contact, the heat conducted through boron carbide nanowires from the heat source membrane to the heat sink membrane will be trivial, which cannot lead to significant resistance change of the Pt coil in the heat sink membrane above the measurement noise background. Therefore, electron beam induced deposition (EBID) has been used to deposit Au or Pt at the contact area to reduce the contact thermal resistance between individual boron carbide nanowires and Pt electrodes, as shown in **Figure 5.5**. The measured thermal conductance thus includes the intrinsic thermal conductance of individual boron carbide nanowires and the enhanced thermal conductance of the contact between nanowires and Pt electrodes.

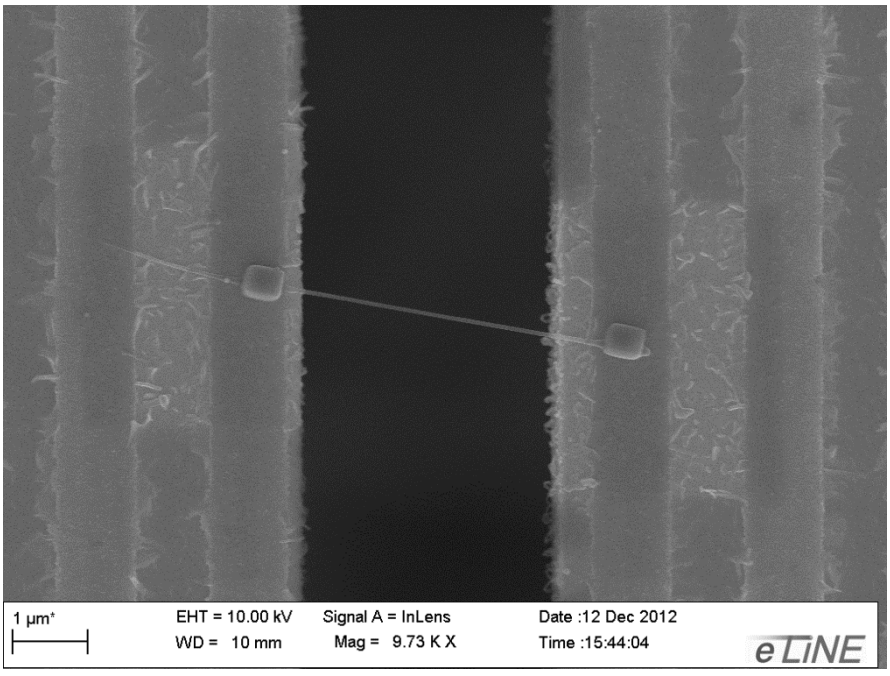

Figure 5.5 An SEM micrograph of a boron carbide nanowire bridging the four electrodes on the microdevice with EBID local deposition of Au at the contact.

5.5 Measurement results

Same as described in Chapter 3 and 4, the measurements were performed with suspended microdevices that have been discussed in details in Chapter 2. However, because of the small thermal conductivity and cross section, the measured effective thermal conductance of the boron carbide nanowire, G_s, is only several times larger than the background thermal conductance, G_{bg}, the difference between G_s and G_{bg} gets further reduced at high temperature as the parasitic radiation heat transfer becomes more apparent.

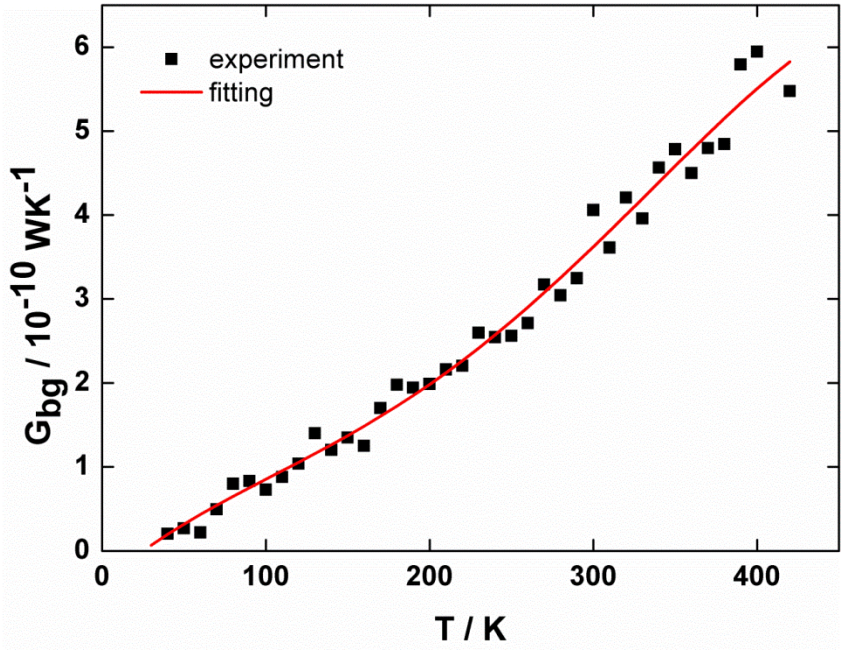

Figure 5.6 Measured background thermal conductance as a function of temperature.

To eliminate the error brought by background, using the same etch-through measurement device but without nanowire bridging the heating and sensing membrane, we measured the background thermal conductance as shown in **Figure 5.6**. G_{bg} was measured to be about 0.3 nW-K^{-1} near room temperature, which is very close to a

previous report (Pettes and Shi 2009). We fit the background data with a 4th order polynomial in a least square sense, as shown in **Figure 5.6**. At each temperature, the fitted G_{bg} was subtracted from the measured effective thermal conductance, to get the corrected thermal conductance G_s, which is contributed solely from boron carbide nanowires.

Thirteen samples with different fault orientations, fault densities and diameters have been measured. The diameters of the samples are based on the single crystalline core diameter from individual TEM characterization. The measured thermal conductivities are summarized in **Figure 5.7**.

Overall, the measured effective thermal conductivities of boron carbide nanowires are significantly lower than that of bulk single crystalline or polycrystalline samples. While we previously reported that there is a diameter dependence among 3 measured samples (Guan, Gutu *et al.* 2012), the diameter of that study is based on SEM characterization. Here we obtained the actual single crystalline core diameter of the samples, which is more accurate. For these samples, there is no clear diameter dependence, likely due to the complex crystal structure of the boron carbides and multiple factors that could influence their thermal conductivities (carbon content, fault orientations, densities, etc.) However, it seems that boron carbide nanowires with transverse faults or both transverse faults and axial faults have relatively lower thermal conductivities than nanowires with only axial faults. A further quantitative carbon content study with, for example, electron energy loss spectroscopy (EELS), is needed to dissect the effects of different factors on the thermal conductivities of these boron carbide nanowires. At this moment, the data suggests that all different factors, nanowire size,

carbon content, as well as fault orientation and density could have important effects on the thermal conductivity of boron carbide nanowires.

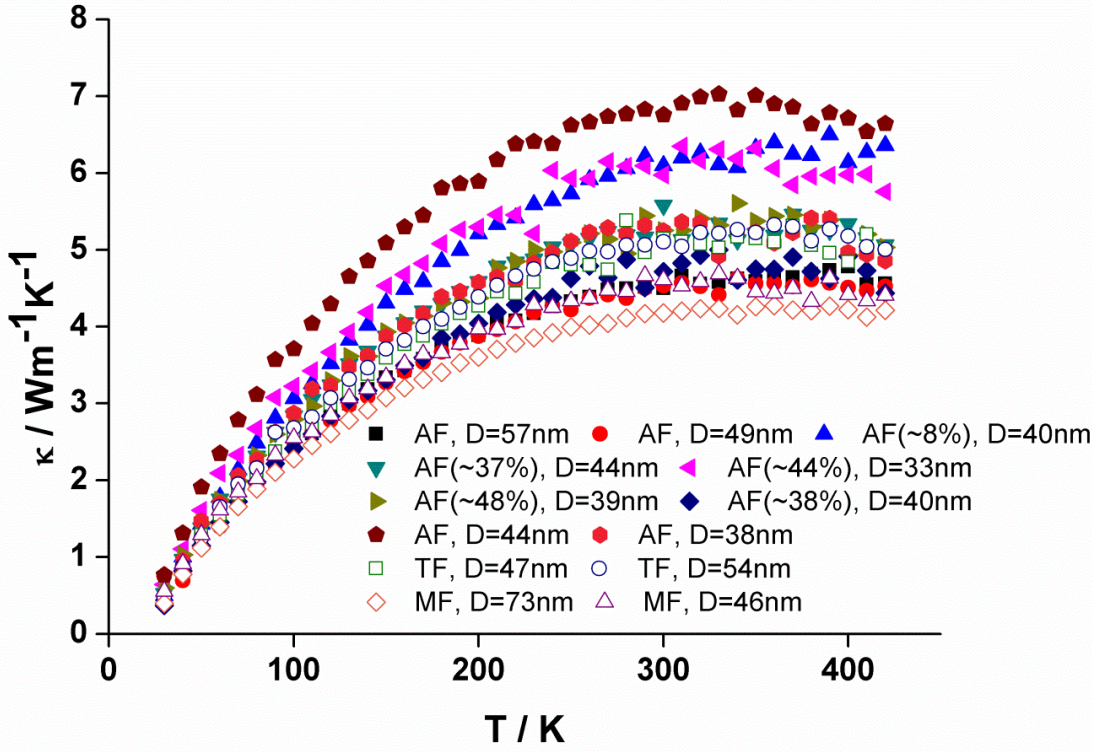

Figure 5.7 Measured thermal conductivities of boron carbide nanowires. AF (axial faults), TF (transverse faults), MF (multiple fault orientations, e.g. both AF and TF found). Numbers inside the brackets are fault densities, which are calculated as (number of faults planes)/(number of total planes counted).

5.6 Summary

Due to the complex crystal structure and factors such as carbon content, fault orientation and density, the thermal conductivity of boron carbide nanowires is intriguing and more work needs to be done to dissect the effects of each factor. However, it

represents a good opportunity to tune these parameters to achieve a better thermoelectric figure of merit.

6. CONTACT THERMAL CONDUCTANCE BETWEEN INDIVIDUAL MULTI-WALLED CARBON NANOTUBES

Carbon based nanomaterials, such as carbon nanotubes (CNTs) and graphene, which have shown superior electrical, optical, mechanical and thermal properties, have been under intensive investigation during the past two decades for achieving complete physical understanding of their novel properties, as well as utilizing them for various applications, including nanocomposite materials, nanoelectronics and nano-optics.

One of the most important applications, nanocomposite materials, which usually involve polymer as the matrix and nanomaterials such as CNTs and graphenes as fillers, have shown better performance in their mechanical strength, electrical and thermal transport properties. Although percolation thresholds have been experimentally demonstrated for CNT composites signified by steep increase in electrical conductivity at low nanotube loadings (Biercuk, Llaguno *et al.* 2002; Shenogina, Shenogin *et al.* 2005), no signature of the percolation threshold has been seen for their thermal transport measurements. The reported experimentally measured thermal conductivities of composites or suspensions filled with CNTs are well below the "law of mixtures" prediction (Choi, Zhang *et al.* 2001; Biercuk, Llaguno *et al.* 2002). The low thermal conductivities of the nanocomposites have been attributed to the high contact thermal resistances between contacted nanomaterials fillers and between fillers and the polymer matrix (Nan, Liu *et al.* 2004; Shenogin 2004). There have been several reports on trying to solve the contact problem, such as using aligned CNT films as filler (Huang, Liu *et al.*

2005), using hybrid graphite nanoplatelet-CNT as fillers (Yu, Ramesh *et al.* 2008), and magnetic field processing (Choi, Brooks *et al.* 2003). However, the improvement is relatively small and a complete physical understanding on thermal transport at interface between graphitic layers and the polymer matrix is badly needed to obtain any significant breakthrough in CNT-polymer thermal property enhancement.

Using picosecond transient absorption method, Huxtable *et al*. measured the interface thermal conductance between single-walled carbon nanotubes and sodium dodecyl sulphate (SDS) surfactant micelle, showing very small interface thermal conductance ($G \approx 12$ MW m^{-2} K^{-1}) (Huxtable, Cahill *et al.* 2003). Several molecular dynamics (MD) studies also show large interfacial resistance between CNTs or between CNTs and host materials (Shenogin 2004; Zhong and Lukes 2006; Prasher, Hu *et al.* 2009). We have performed a systematic experimental study of contact thermal conductance between two individual multi-walled CNTs (MWCNTs) as a function of tube diameters. Contrary to the expectation that the contact thermal conductance is an intrinsic property of graphitic layers, which should be linearly proportional to the contact area, we found that the normalized value, i.e., contact thermal conductance per unit area, is still a function of the tube diameter. We attribute this diameter dependence of contact thermal conductance per unit area to the unexpected large cross-plane phonon mean free path (hundreds of nanometers) in graphite.

Subjected to higher van der Waals forces along their length axis, CNTs are extremely hydrophobic and prone to aggregation, and therefore are not readily dispersed in aqueous or non-aqueous solutions (Wang, Shi *et al.* 2008). This has been a major obstacle for their applications in industry. It has been reported that natural organic matter

(NOM), in particular its major component, humic acid (HA), can disperse CNTs in the aqueous phase (Wang, Shi *et al.* 2008). Therefore, HA coated MWCNTs could be ideal candidate fillers for nanocomposite materials. In this case, since MWCNTs and the polymer matrices are not in direct contact with each other, which is the most common case because the dispersion of MWCNTs involves surfactants or other chemicals, the contact thermal resistance between MWCNTs and surfactants instead of the one between MWCNTs and polymer matrices will be of more practical significance and crucial to the thermal performance of nanocomposites.

In this chapter, the contact thermal conductance between two individual MWCNTs as a function of tube diameter will be introduced first. Then the measurement results of contact thermal conductance between two individual MWCNTs with humic acid coating will be discussed and compared with the results for tubes without humic acid coating.

6.1 Measurement scheme

Same as described in Chapter 3, 4 and 5, the measurements were performed with the suspended microdevices that have been discussed in details in Chapter 2. MWCNTs were first dispersed in reagent alcohol or humic acid to make a suspension. A drop of suspension was casted onto a PDMS piece. Using an in-house built micromanipulator, an individual MWCNT with or without humic acid coating was broken into two segments (**Figure 6.1(a-b)**) onto the PDMS piece and transferred to the measurement device, forming a cross contact (**Figure 6.1(c)**) between the two membranes (**Figure 6.1(d)**).

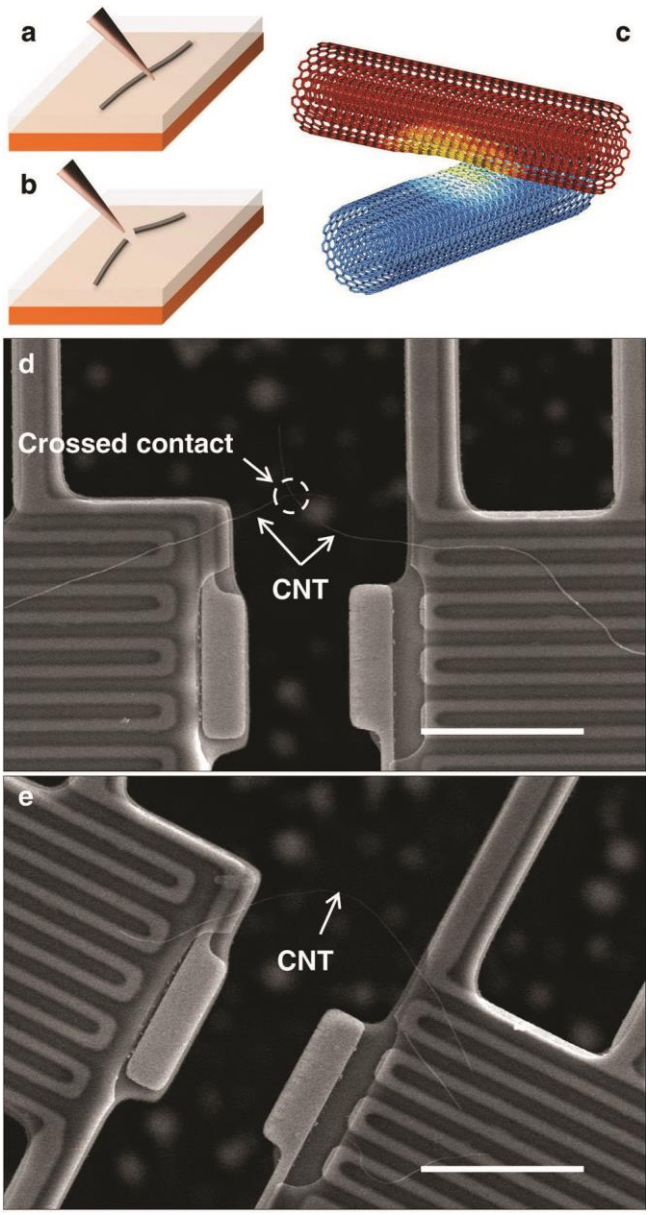

Figure 6.1 Cross-contact sample. **a-b**, One single MWCNT is cut into two segments with a sharp probe. **c**, The nansocale junction of the two segments poses dominant resistance at the contact region. **d**, A scanning electron microscopy (SEM) micrograph of one measured sample composed of two MWCNT segments forming a cross contact between the heat source/sink. Scale bar: 7.5 μm. **e**, One of the two segments is realigned

on the microdevice to evaluate the thermal resistance of the MWCNT segments in the cross contact sample. Scale bar: 7.5 μm.

After measuring the total thermal resistance of this cross-contact sample, one segment was removed and the other was realigned to bridge the two membranes, as shown in **Figure 6.1(e)**. The length of the single MWCNT segment between the two suspended membranes was adjusted to be close to that of the total heat transfer route of the cross-contact sample between the two membranes. From these two measurements, the contact thermal resistance, R_C (or conductance, G_C=1/R_C) of the nanoscale junction between the two MWCNTs can be extracted.

For the cross-contact sample, the measured total thermal resistance $R_{\text{tot-C}}$ can be written as

$$R_{tot-C} = R_{CM-C} + L_C \times R_{CNT/L} + R_C, \tag{6.1}$$

where $R_{\text{CM-C}}$ is the sum of the contact thermal resistance between the two MWCNT segments and the two SiN_x membranes, L_{C} is the total length of the two CNT segments between the two membranes forming the heat transfer route, $R_{\text{CNT/L}}$ is the thermal resistance of the MWCNT per unit length, and R_{C} is the contact thermal resistance between the two MWCNT segments. For the sample with a single CNT segment between the two membranes, the measured total thermal resistance, $R_{\text{tot-S}}$, can be expressed as

$$R_{tot-S} = R_{CM-S} + L_S \times R_{CNT/L}, \tag{6.2}$$

where $R_{\text{CM-S}}$ is the contact thermal resistance between the MWCNT segment and the two membranes, L_{S} is the length of the CNT segment between the two membranes.

It has been shown that for the same CNT, $R_{CM\text{-}C}$ is approximately equal to $R_{CM\text{-}S}$ if the length of the tube on the membrane is long enough and the CNT is fully thermalized with the membrane, as shown in Chapter 3. It is worth noting that even if the length of the CNT on one of the membranes is only half of that needed for the CNT to be fully thermalized, $R_{CM\text{-}C}$ (or $R_{CM\text{-}S}$) only increases by ~17% (Yu, Saha *et al.* 2006), which can be considered in uncertainty analysis. Based on this observation, from Eq. (6.1) and (6.2), it can be seen that if $L_S = L_C$, the contact thermal resistance between the two MWCNTs can be derived as

$$R_C = R_{tot-C} - R_{tot-S}, \tag{6.3}$$

However, in practice, it is very difficult for L_S to be exactly the same as L_C. For bare MWCNTs, what we achieved is to have L_C and L_S to be within ± 1.8 μm and the ratio of L_C/L_S to be in the range of 0.92-1.25. In fact, other than the sample of the 42 nm MWCNT, we have $|L_C - L_S| \leq 0.7$ μm and $0.92 \leq L_C/L_S \leq 1.03$. For MWCNTs with humic acid coating, the differences between L_C and L_S are within ± 0.3 μm and the ratio of L_C/L_S to be in the range of $0.99 \leq L_C/L_S \leq 1.04$. Under this condition, if we neglect the difference between $R_{CM\text{-}C} \times L_S$ and $R_{CM\text{-}S} \times L_C$, then

$$R_C = R_{tot-C} - R_{tot-S} \times L_C / L_S . \tag{6.4}$$

6.2 Uncertainty Analysis

The total contact thermal resistance, R_C, between two MWCNTs can be calculated from either Eq. (6.3) or Eq. (6.4). Eq. (6.3) neglects the difference between the lengths of the heat transfer path of the cross-contact sample and the corresponding single CNT

segment while Eq. (6.4) neglects a term of $R_{CM\text{-}S} \times L_C/L_S - R_{CM\text{-}C}$. The error introduced by using Eq. (6.3) is

$$Err_1 = | R_{CNT/L} \times (L_C - L_S) |, \tag{6.5}$$

while the error introduced by using Eq. (6.4) is

$$Err_2 = | R_{CM} \times (L_S - L_C) / L_S |, \tag{6.6}$$

where $R_{CM} = R_{CM\text{-}C} = R_{CM\text{-}S}$ when the CNT is fully thermalized.

From Eqs. (6.5) and (6.6), it can be seen that $Err_2 < Err_1$ if $R_{CM} \leq L_S R_{CNT/L}$. From Chapter 3 it has been showed that for a 66-nm-diameter MWCNT, $R_{CM} \leq 4\ \mu m \times R_{CNT/L}$ above 50 K. For bare MWCNT samples measured, all L_S are larger than 7 μm. For HA coated MWCNT samples measured, all L_S are at least 6.85 μm or above. Therefore, here we us Eq. (6.4) to calculate R_C, which will lead to a smaller error.

As discussed in Chapter 3, the minimum length needed for the 66-nm-diameter MWCNT to be fully thermalized with the membranes is ~4 μm at 300 K, and becomes smaller at lower temperature. If this prerequisite cannot be satisfied, which means the CNTs are not fully thermalized with the membrane, then $R_{CM\text{-}S}$ is not equal to $R_{CM\text{-}C}$. In this case, the difference between $R_{CM\text{-}S}$ and $R_{CM\text{-}C}$ should be considered with Eq. (6.6) changed into

$$Err_2 = \left| \frac{L_S R_{CM-C} - L_C R_{CM-S}}{L_S} \right|. \tag{6.7}$$

The uncertainty of R_C, U_{R_C}, can be written as

$$(\frac{U_{R_C}}{R_C})^2 = (\frac{U_{R_{tot-C}}}{R_C})^2 + (\frac{L_C}{L_S})^2(\frac{U_{R_{tot-S}}}{R_C})^2 + (\frac{R_{tot-S}}{R_C})^2(\frac{U_{L_C}}{L_S})^2 + (\frac{R_{tot-S}}{R_C})^2(\frac{L_C}{L_S})^2(\frac{U_{L_S}}{L_S})^2 + (\frac{Err_2}{R_C})^2 \quad , \tag{6.8}$$

where U_X is the uncertainty of variable X. The uncertainties of the measured total thermal resistance, $R_{tot\text{-}C}$ and $R_{tot\text{-}S}$, are estimated using the Monte Carlo (MC) method, as described in Chapter 2.

6.3 Contact thermal conductance between individual bare MWCNTs

6.3.1 Total contact thermal conductance

Five MWCNT samples of different diameters from 42 nm to 68 nm have been measured following the measurement procedure described before. **Figure 6.2** shows the obtained total contact thermal conductance, G_C, as a function of temperature. The results show that for all five samples, G_C increases with temperature in the measurement temperature range, due to larger heat capacity at higher T. In addition, G_C increases with the tube diameter, which is very reasonable because the contact area between two CNTs increases for larger diameter tubes.

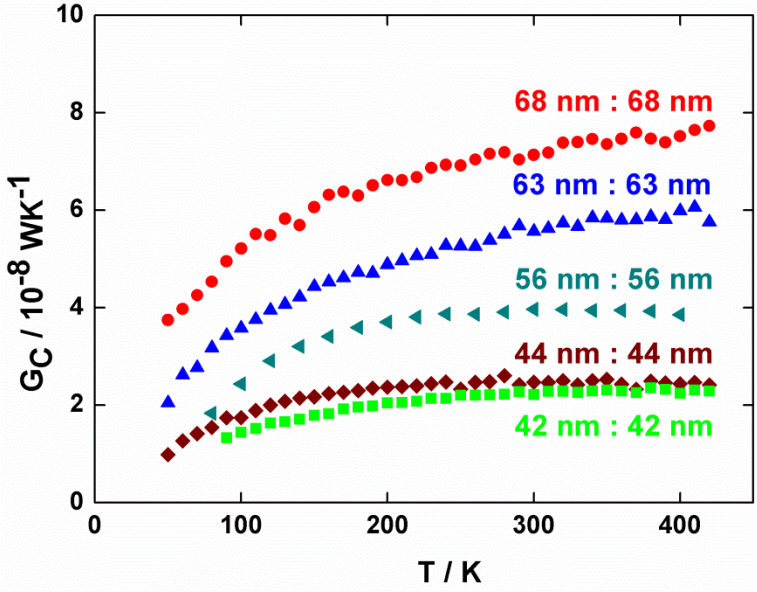

Figure 6.2 Measured total contact thermal conductance as a function of temperature for bare MWCNT samples with different diameters.

6.3.2 Contact thermal conductance per unit area

To further understand thermal transport through the nanoscale contact, we seek to normalize the measured total contact thermal conductance with respect to the contact area between the two CNTs.

To calculate the contact area, parameters for the van der Waals (vdW) interactions between two MWCNTs and the Hamaker constant for graphite need to be used. The Lennard-Jones (LJ) potential, which is commonly used to describe vdW interactions, can be written as

$$\varphi(r) = 4\varepsilon[(\frac{\sigma}{r})^{12} - (\frac{\sigma}{r})^{6}], \tag{6.9}$$

where ε is the depth of the potential well, and σ is a length scale parameter that determines the position of the potential minimum. ε = 2.4 meV, σ = 0.34 nm and ε = 4.41

meV, σ = 0.228 nm are the two sets of parameters commonly used to describe the vdW interactions between CNTs (Maruyama, Igarashi *et al.* 2006; Zhong and Lukes 2006; Kumar and Murthy 2009; Zhbanov, Pogorelov *et al.* 2010).

The Hamaker constant is defined as (Hamaker 1937)

$$H = 4\varepsilon\pi^2 N^2 \sigma^6, \tag{6.10}$$

where N is atom number density, which is calculated based on the C-C bond length (0.142 nm) and the interlayer distance of MWCNTs (0.34 nm), $N = 1.11\times10^{29}$ atom/m^3. From equation (6.10), $H = 28.9\times10^{-20}$ J, if $\varepsilon = 2.4$ meV, $\sigma = 0.34$ nm, and $H = 4.8\times10^{-20}$ J, if ε = 4.41 meV, σ = 0.228 nm. Comparing with the Hamaker constant between neighboring atomic layers in graphite, which is 23.8×10^{-20} J (Drzymala 1994), we choose $\varepsilon = 2.4$ meV, $\sigma = 0.34$ nm to describe the vdW interactions between CNTs.

The contact area between two perpendicularly crossed cylinders of same radius is the same as that between a sphere of the same radius and a plane (Pilkey 1994). Three different continuum mechanics models, the JKR model (Johnson, Kendall *et al.* 1971), the DMT model (Derjaguin, Muller *et al.* 1975), and the Maugis model (Maugis 1992) are commonly used to calculate the contact area between a sphere and a plane.

A parameter μ has been constructed to guide the choice of these models (Johnson and Greenwood 1997), and μ is defined as

$$\mu = \left(\frac{R(\Delta\gamma)^2}{E^{*2} z_0^3}\right)^{1/3}, \tag{6.11}$$

where R is the reduced radius of the sphere, and for CNT-CNT contact, R is equal to the radius of the CNT. $\Delta\gamma$ is the adhesion energy, $E^* = [(1-\nu_1^2)/E_1 + (1-\nu_2^2)/E_2]^{-1}$,

where E is the Young's modulus and ν is the Poisson's ratio. z_0 is the equilibrium separation as $z_0 = (2/15)^{1/6}\sigma$ (Yu and Polycarpou 2004), and z_0 = 0.243 nm for σ = 0.34 nm, which is very close to the value between two SWCNTs obtained from *ab initio* calculation (Fuhrer, Nygard *et al.* 2000). The adhesion energy can be calculated from the Hamaker constant as (Yu and Polycarpou 2004)

$$\Delta\gamma = \frac{H}{16\pi z_0^2}. \tag{6.12}$$

This gives $\Delta\gamma$ = 0.10 J/m^2 as H = 28.9×10^{-20} J. The radial Young's modulus of CVD-grown MWCNTs has been reported as 30±10 GPa (Palaci, Fedrigo *et al.* 2005) which is adopted in the current calculation. The Poisson's ratio is selected as that of graphite, which is 0.012 (Prasher 2008). Substituting the above values into equation (6.11), we get the value of μ as 0.4~0.48 for MWCNTs of 40~70 nm in diameter. According to the adhesion map (Johnson and Greenwood 1997), the Maugis model is selected to calculate the contact area between two MWCNTs forming a cross contact.

In Maugis model, the radius of the contact area is given as (Maugis 1992; Yu and Polycarpou 2004)

$$a = \left(\frac{3\pi\Delta\gamma R^2}{4E^*}\right)^{1/3}\lambda\left[\sqrt{m^2-1} + m^2\tan^{-1}\left(\sqrt{m^2-1}\right)\right], \tag{6.13}$$

where $\lambda = 1.16\mu$, m = r_c/a, and r_c is the critical cutoff radius ($r_c > a$), and m is given by

$$\frac{\lambda^3}{2}\left[\sqrt{m^2-1} + m^2 tan^{-1}\left(\sqrt{m^2-1}\right)\right]^2\left[\sqrt{m^2-1} + (m^2-2)tan^{-1}\left(\sqrt{m^2-1}\right)\right] +$$

$$\frac{4\lambda^3}{3}\left[\sqrt{m^2-1} + m^2 tan^{-1}\left(\sqrt{m^2-1}\right)\right]\left[\sqrt{m^2-1}tan^{-1}\left(\sqrt{m^2-1}\right) - m + 1\right] = 1. \tag{6.14}$$

Since the two MWCNTs are not always forming a cross contact of 90°, we make the following corrections to evaluate the actual contact area (A) (Roark and Young 1975):

$$A = A_{\pi/2} / \sin\alpha , \tag{6.15}$$

where $A_{\pi/2}$ denotes the contact area when the included angle of the cross contact is $\pi/2$, which can be calculated based on the radius of the contact area from Eq. (6.13).

The normalized contact thermal conductance per unit area, G_{CA}, is plotted in **Figure 6.3(a)**. For normalized G_{CA}, we expect that the results should be approximately the same for different diameter tubes, i.e., the five lines should lump into one curve. However, the results clearly show that G_{CA} increases with the tube diameter, a trend totally unexpected. To further understand the diameter dependence, we normalize G_{CA} with the tube diameter (D), as shown in **Figure 6.3(b)**. It is interesting to see that within the measurement uncertainty, the five curves of G_{CA}/D overlap with each other. The linear dependence of G_{CA} to D indicates that inner layers of the CNTs affect the contact thermal conductance at the nanoscale junction between the two CNTs, not through adding thermal resistance, but by reducing thermal resistance, which further confirms that the measured contact thermal resistance is dominated by the nanoscale junction between the two outmost layers of the two tubes.

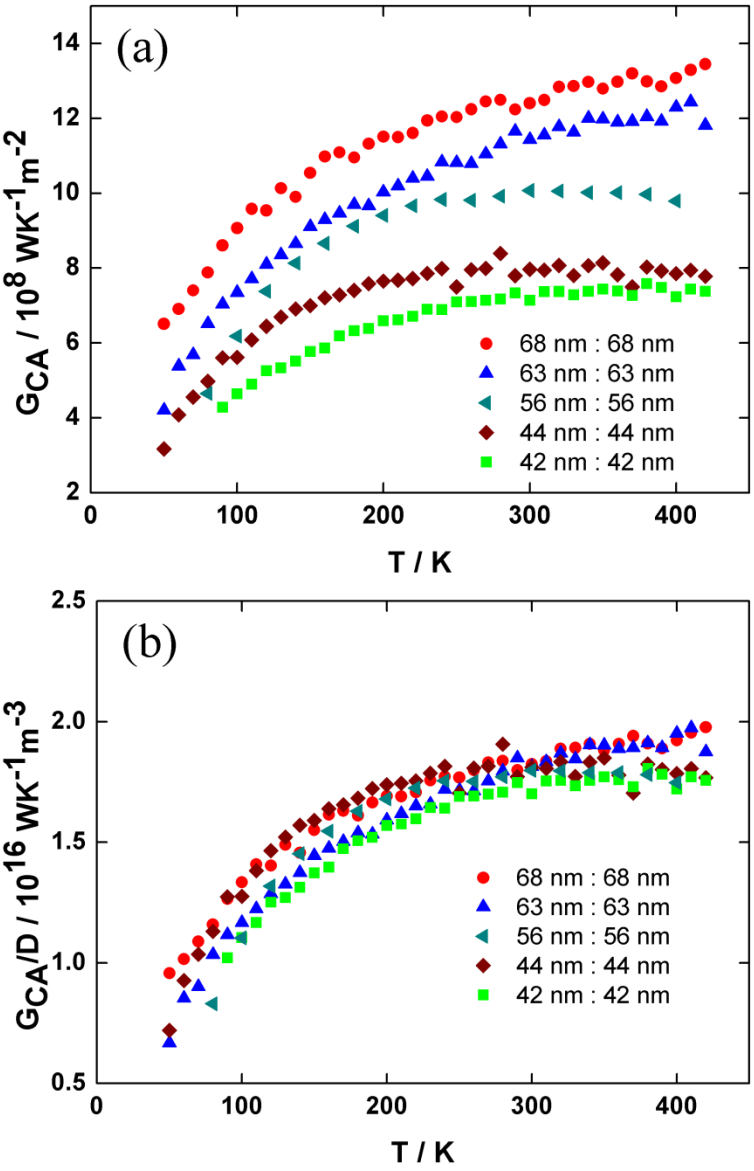

Figure 6.3 The measured contact thermal conductance as a function of temperature for bare MWCNT samples with different diameters. **(a)** The contact thermal conductance per unit area. **(b)** The contact thermal conductance per unit area normalized with the tube diameter.

The obtained G_{CA} is still far below the upper bound that can be obtained from theoretical reasoning. The upper bound for the conductance in the limit of very large

number of layers in each stack can be simply regarded as the interfacial thermal conductance between two neighboring atomic layers in bulk graphite. Assuming the interfaces can be treated as resistors connected in series, the interfacial conductance can be estimated as $G_{CA,upper} = k / a$, where k is the cross plane graphite thermal conductivity and a is the spacing between planes. With k = 6.8 W/m-K (Taylor 1966) and a = 0.34 nm, $G_{CA,upper}$ = 20 GW/m^2-K, which is still one order of magnitude higher than the experimental data.

Since we have already obtained the interfacial thermal conductance per unit area, which is not related to the size of the contact area anymore, we consider a graphite thin film of uniform cross-sectional area. When the thickness of the thin film is less than the bulk phonon mean free path (m.f.p) in the c-axis, l_∞, then the effective phonon m.f.p in the c-axis can be expressed as $1/l = 1/l_\infty + 2/L$ (Schelling, Phillpot *et al.* 2002), where L is the film thickness. The total thermal resistance for unit area of the film in the c-axis direction is then $R_t = L/k$. If we regard the total thermal resistance as the sum of the interfacial thermal resistance between two atomic layers, R_1, considering that $L = na$, then G_{CA} can be written as

$$G_{CA} = \frac{1}{R_1} = \frac{n-1}{R_t} = \frac{n-1}{\frac{L}{Fl}} = F\frac{n-1}{L(\frac{1}{l_\infty}+\frac{2}{L})} = F\frac{(n-1)l_\infty}{2l_\infty + na}, \qquad (6.16)$$

where F is a parameter representing the integral of the product of heat capacity and c-axis component of phonon velocity over an appropriate frequency range. From Eq. (6.16) we can see that if $l_\infty >> na$, then G_{CA} is linearly proportional to the number of layers, n. In fact, based on Eq. (6.16), we can estimate the cross-plane phonon m.f.p for graphite. At

300 K, if we normalize G_{CA} with the number of layers in the MWCNTs, by assuming that the distance between neighboring CNT layers is 0.34 nm, the average G_{CA} / (*# of layers*) is 0.805×10^7 W/m^2-K-layer, which can be regarded as half of the pre-factor (F) in Eq. (6.16) and has the physical meaning as the increment of interfacial thermal conductance with each additional atomic layer added. If the film thickness further increases and approaches the limit that *na* is much larger than l_∞, then the upper bound of the interfacial conductance $G_{CA,upper}$ = 20 GW/m^2-K is reached and we can solve for l_∞ from Eq. (6.16) as 422 nm.

This is a surprisingly large value because it is widely believed that the *c*-axis l_∞ for graphite is only a few nm. It is worth noting that the very short m.f.p is obtained by assuming that all phonon modes in graphite contribute to thermal transport in the *c*-axis direction. However, for graphite, the vdW interactions between different atomic layers cannot sustain transport of the high frequency phonons existing in each atomic layer.

6.4 Contact thermal conductance between individual MWCNTs with humic acid coating

Four MWCNT samples with humic acid coating of different diameters have been measured following the measurement scheme described before. **Figure 6.4** shows the obtained total contact thermal conductance, G_C, as a function of temperature. Different from the results of bare MWCNT, here the measured total contact thermal conductance doesn't show any sensible diameter dependence. In addition, the contact thermal conductance is lower than that between bare MWCNTs of similar diameter.

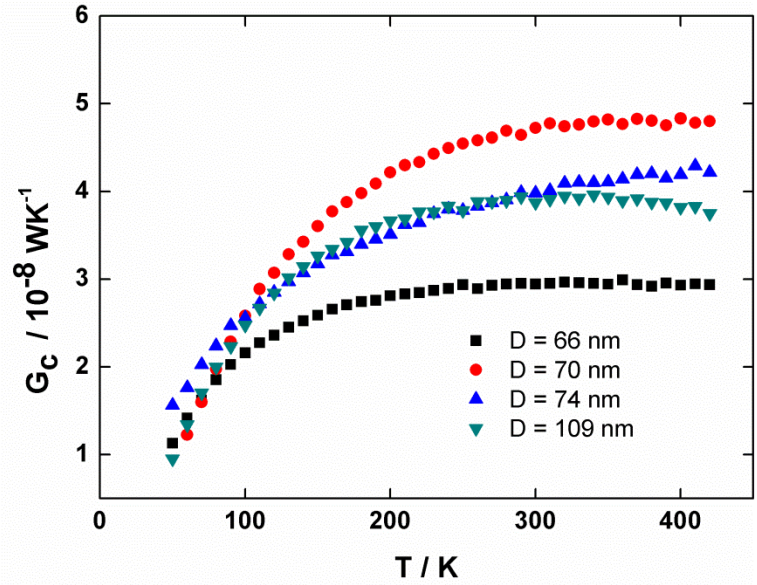

Figure 6.4 Measured total contact thermal conductance as a function of temperature for MWCNT samples with humic acid coating of different diameters.

Instead of direct interactions between graphite carbon layers, thermal transport between two individual HA coated MWCNTs will go through three interfaces and two HA layers: namely the interface between graphite carbon layer and HA coating layer in MWCNT 1, the HA layer in MWCNT 1, the interface between HA coating layers of MWCNT 1 and 2, the HA layer in MWCNT 2, and the interface between HA coating layer and graphite carbon layer of MWCNT 2. Therefore, the measured contact thermal conductance, R_C, is composed of five parts:

$$R_C = R_{C-1} + R_{HA-1} + R_{C-1,2} + R_{HA-2} + R_{C-2}, \tag{6.17}$$

where $R_{C\text{-}1}$ and $R_{C\text{-}2}$ are the contact thermal resistances between graphite carbon layer and HA coating layer in MWCNT 1 and 2, respectively. $R_{C\text{-}1,2}$ is the contact thermal resistance between HA layers in MWCNT 1 and 2. $R_{HA\text{-}1}$ and $R_{HA\text{-}2}$ are thermal resistances of HA layers in MWCNT 1 and 2, respectively.

Figure 6.5(a-c) shows TEM micrographs of three different positions in the measured 109 nm in diameter MWCNT sample. It's clear that the thickness of the outside HA coating layer is not uniform, as well as the roughness of the HA layer. At current stage, because it is impossible to perform a high resolution TEM examination of the MWCNT-MWCNT contact, it's extremely difficult to precisely determine the morphology of the HA layer at the CNT-CNT contact. Therefore, there is no way to clearly understand the contribution of different thermal resistance to the measured total thermal resistance. However, from **Figure 6.5** we can see that due to the variations of HA coating from tube to tube, factors other than the tube diameter will affect the terms in Eq. (6.17). For example, the thickness of the HA coating could be different and the contact between the HA coatings could also varies since they are not as flat as the atomic graphite layers in bare MWCNTs. Therefore, we expect no diameter dependence of measured contact thermal conductance, as shown in **Figure 6.4**.

Figure 6.6 shows the measured contact thermal conductance of both bare and HA coated MWCNT samples. As the diameters of the measured MWCNT samples with HA coatings are larger or at least comparable to the bare MWCNT samples, it clearly shows that HA coating will impede thermal transport between MWCNTs and lower the contact thermal conductance. However, it is worth noting that even though several more resistances are added at the contact, the contact thermal conductance only increases by ~100% on average, which is not very significant considering the very different property of HA and MWCNT.

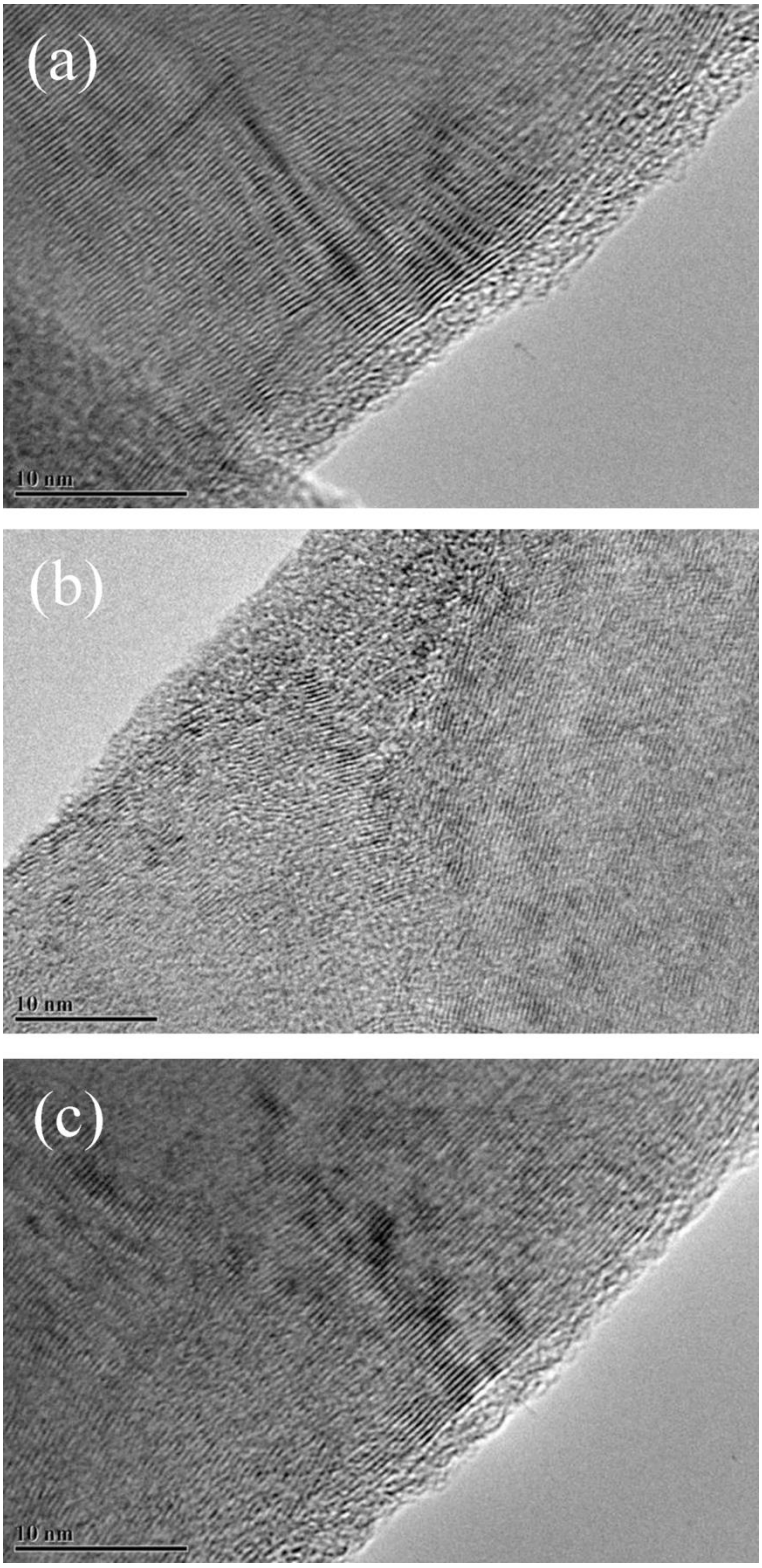

Figure 6.5 TEM micrographs of three different positions in the measured 109 nm in diameter MWCNT sample.

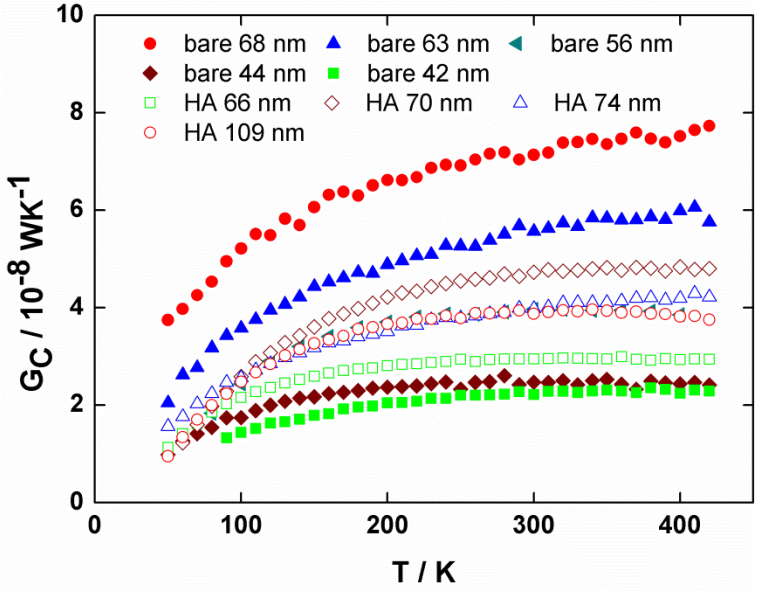

Figure 6.6 Measured contact thermal conductance of both bare and HA coated MWCNT samples.

6.5 Summary

The contact thermal conductance between individual bare MWCNTs and humic acid coated MWCNTs were measured. For bare MWCNTs, contrary to the common expectation, the normalized contact thermal conductance per unit area between MWCNTs depends linearly on the tube diameter, showing that the phonon mean free path in the *c*-axis direction of graphite is two orders of magnitude higher than the commonly believed value of just a few nanometers. For MWCNTs with humic acid coating, no diameter dependence was observed for the total contact thermal conductance, likely due to the humic acid layer variations, which could have significant impact on the total contact thermal resistance.

7. SUMMARY

This dissertation presents an experimental study on thermal transport through various individual nanostructures and their contacts. By utilizing a suspended microdevice-based thermal measurement platform and designing different measurement schemes, thermal properties of these nanostructures and contacts that are normally difficult to capture were successfully measured. Interesting transport phenomena were discovered and the underlying physics was discussed. This chapter will summarize these results and discuss future directions.

The suspended microdevice was fabricated by standard microfabrication techniques. It includes two adjacent suspended SiN_x membranes each supported by six long SiN_x beams and patterned with integrated platinum coils serving as resistance heaters and thermometers. By adding a few more steps, TEM compatible etch-through suspended microdevices were designed and fabricated to fulfill the needs for one on one thermal property-structure characterization. Individual nanostructures, such as nanowires and nanotubes can be placed bridging the two membranes by careful micromanipulation. Electron Beam Induced Deposition (EBID) technique can be used to locally deposit Au or Pt at the wire/tube-membrane contact to reduce the contact thermal resistance. Monte Carlo simulation was used to estimate the electrical measurement uncertainty and combined with uncertainties of materials dimensions from SEM, AFM or TEM characterization, the overall uncertainty of the thermal measurement can be estimated.

The intrinsic thermal conductivity of an individual carbon nanotube and its contact thermal resistance with the heat source/sink have been extracted simultaneously through multiple measurements with different lengths of the tube between the heat source and the heat sink. Results on a 66-nm-diameter MWCNT show that above 100 K, contact thermal resistance can contribute up to 50% of the total measured thermal resistance. Therefore, the intrinsic thermal conductivity of the MWCNT is significantly higher than the effective thermal conductivity derived from one single measurement without eliminating the contact thermal resistance. At 300 K, the contact thermal resistance between the tube and the substrate for a unit area is 2.2×10^{-8} m^2 K W^{-1}, which is on the lower end among several published data. Results also indicate that for nanotubes of relatively high thermal conductance, electron-beam-induced gold deposition at the tube-substrate contacts may not reduce the contact thermal resistance to a negligible level.

Following similar scheme, intrinsic thermal conductivities of individual silicon nanoribbons with different thicknesses and widths are acquired through multiple measurements of the same sample with different lengths between the heat source and heat sink to eliminate the effects of contact thermal resistance between the sample and the heat source/sink. Results show that due to the flat contact and relatively large contact area, the contact thermal resistance between silicon nanoribbons and suspended membranes is negligible. For ribbons of 17–38 nm thick, their thermal conductivities still show a clear width dependence even when the width is ~2–10 times larger than the thickness. Detailed examination of the thermal conductivity versus the Casimir length suggests that the Casimir length is not the only important parameter for the classical boundary confinement effects on thermal transport in nanostructures. A more accurate physical

model capturing both width and thickness boundary scattering effect need to be established to further compared with the experimental observation.

Because of the great potential as high temperature thermoelectric materials, thermal conductivities of boron carbide nanowires were measured using the etch-through suspended microdevice platform. One on one thermal property-structure characterization was performed to explore the effect of various structure factors on its thermal properties. The results show that the fault orientation, namely axial faults and transverse faults may have different effects on phonon transport through the nanowire. Carbon content, which has large impact on the thermal conductivities of bulk boron carbides, is very likely to affect thermal transport through boron carbide nanowire as well. Therefore, it's necessary to quantify the carbon content in measured samples. Once the carbon content factor is isolated, a solid conclusion on faults orientation and density on thermal transport inside boron carbide nanowires can be better understood. By recognizing the effect of different structural factors on thermal transport and through controllable materials synthesis, thermoelectric efficiency of boron carbide nanowires might be enhanced.

The contact thermal conductance between individual bare MWCNTs or humic acid coated MWCNTs were acquired by measuring the thermal conductance of nanotube assemblies and individual nanotubes separately. For bare MWCNTs, contrary to the common expectation, the normalized contact thermal conductance per unit area between MWCNTs depends linearly on the tube diameter, suggesting that the phonon mean free path in the *c*-axis direction of graphite is two orders of magnitude higher than the commonly believed value of just a few nanometers. For MWCNTs with humic acid coating, no diameter dependence was observed for the total contact thermal conductance,

likely due to variations of the humic acid coating, which have significant impact on the total contact thermal resistance. To further understand the effects of coating on the contact thermal conductance, more controllable coating method, such as atomic layer deposition (ALD) to uniformly coat the MWCNTs with a monolayer of materials is needed. Measurement based on those samples may disclose more interesting phenomena for thermal transport through interface between graphitic carbon nanomaterials and polymer matrices.

REFERENCES

Amin, S. S., S.-y. Li, et al. (2009). "Single Crystalline Alkaline-Earth Metal Hexaboride One-Dimensional (1D) Nanostructures: Synthesis and Characterization." *Chemistry of Materials*, **21**, 763-770.

Aselage, T. L., D. Emin, et al. (1998). "Large Enhancement of Boron Carbides' Seebeck Coefficients through Vibrational Softening." *Physical Review Letters*, **81**, 2316-2319.

Ashbee, K. H. G. (1971). "Defects in boron carbide before and after neutron irradiation." *Acta Metallurgica*, **19**, 1079-1085.

Baloch, K. H., N. Voskanian, et al. (2010). "Controlling the thermal contact resistance of a carbon nanotube heat spreader." *Applied Physics Letters*, **97**, 063105.

Berber, S., Y.-K. Kwon, et al. (2000). "Unusually High Thermal Conductivity of Carbon Nanotubes." *Physical Review Letters*, **84**, 4613-4616.

Bid, A., A. Bora, et al. (2006). "Temperature dependence of the resistance of metallic nanowires of diameter ⩾15nm: Applicability of Bloch-Grüneisen theorem." *Physical Review B*, **74**.

Biercuk, M. J., M. C. Llaguno, et al. (2002). "Carbon nanotube composites for thermal management." *Applied Physics Letters*, **80**, 2767.

Bouchacourt, M. and F. Thevenot (1985). "The correlation between the thermoelectric properties and stoichiometry in the boron carbide phase B4C-B10.5C." *Journal of Materials Science*, **20**, 1237-1247.

Boukai, A. I., Y. Bunimovich, et al. (2008). "Silicon nanowires as efficient thermoelectric materials." *Nature*, **451**, 168-171.

Brown, E., L. Hao, et al. (2005). "Ballistic thermal and electrical conductance measurements on individual multiwall carbon nanotubes." *Applied Physics Letters*, **87**, 023107.

Cahill, D. G. "Thermal conductivity data." http://users.mrl.uiuc.edu/cahill/tcdata/tcdata.html

Cahill, D. G., W. K. Ford, et al. (2003). "Nanoscale thermal transport." *Journal of Applied Physics*, **93**, 793.

Casimir, H. B. G. (1938). "Note on the conduction of heat in crystals." *Physica*, **5**, 495-500.

Chang, C., D. Okawa, et al. (2007). "Nanotube Phonon Waveguide." *Physical Review Letters*, **99**.

Chen, R., A. I. Hochbaum, et al. (2008). "Thermal Conductance of Thin Silicon Nanowires." *Physical Review Letters*, **101**, 105501.

Chen, Z., W. Jang, et al. (2009). "Thermal contact resistance between graphene and silicon dioxide." *Applied Physics Letters*, **95**, 161910.

Chiu, H. Y., V. Deshpande, et al. (2005). "Ballistic Phonon Thermal Transport in Multiwalled Carbon Nanotubes." *Physical Review Letters*, **95**.

Choi, E. S., J. S. Brooks, et al. (2003). "Enhancement of thermal and electrical properties of carbon nanotube polymer composites by magnetic field processing." *Journal of Applied Physics*, **94**, 6034.

Choi, S. U. S., Z. G. Zhang, et al. (2001). "Anomalous thermal conductivity enhancement in nanotube suspensions." *Applied Physics Letters*, **79**, 2252.

Choi, T.-Y., D. Poulikakos, et al. (2006). "Measurement of the Thermal Conductivity of Individual Carbon Nanotubes by the Four-Point Three-omega Method." *Nano Letters*, **6**, 1589-1593.

Coleman, H. W. and W. G. Steele (2009). Experimentation, Validation, and Uncertainty Analysis for Engineers. Hoboken, New Jersey, John Wiley & Sons, Inc.

Derjaguin, B. V., V. M. Muller, et al. (1975). "Effect of Contact Deformations on the Adhesion of Particles." *Journal of Colloid and Interface Science*, **53**, 314-326.

Dresselhaus, M. S., G. Dresselhaus, et al. (2005). "Raman spectroscopy of carbon nanotubes." *Physics Reports*, **409**, 47-99.

Drzymala, J. (1994). "Hydrophobicity and collectorless floation of inorganic materials." *Advances in Colloid and Interface Science*, **50**, 143-185.

Emin, D. (2006). "Unusual properties of icosahedral boron-rich solids." *Journal of Solid State Chemistry*, **179**, 2791-2798.

Fuhrer, M. S., J. Nygard, et al. (2000). "Crossed Nanotube Junctions." *Science*, **288**, 494-497.

Fujii, M., X. Zhang, et al. (2005). "Measuring the Thermal Conductivity of a Single Carbon Nanotube." *Physical Review Letters*, **95**.

Guan, Z., T. Gutu, et al. (2012). "Boron carbide nanowires: low temperature synthesis and structural and thermal conductivity characterization." *Journal of Materials Chemistry*, **22**, 9853.

Gunjishima, I., T. Akashi, et al. (2001). "Thermoelectric Properties of Single Crystalline B4C Prepared by a Floating Zone Method." *Materials Transactions*, **42**, 1445-1450.

Hamaker, H. C. (1937). "The London-van der Waals attraction between spherical particles." *Physica*, **4**, 1058-1072.

Harman, T. C., P. J. Taylor, et al. (2002). "Quantum dot superlattice thermoelectric materials and devices." *Science*, **297**, 2229-2232.

He, Y. and G. Galli (2012). "Microscopic Origin of the Reduced Thermal Conductivity of Silicon Nanowires." *Physical Review Letters*, **108**, 215901.

Hippalgaonkar, K., B. Huang, et al. (2010). "Fabrication of Microdevices with Integrated Nanowires for Investigating Low-Dimensional Phonon Transport." *Nano Letters*, **10**, 4341-4348.

Hochbaum, A. I., R. Chen, et al. (2008). "Enhanced thermoelectric performance of rough silicon nanowires." *Nature*, **451**, 163-167.

Huang, H., C. Liu, et al. (2005). "Aligned Carbon Nanotube Composite Films for Thermal Management." *Advanced Materials*, **17**, 1652-1656.

Hull, R. (1999). Properties of crystalline silicon, The Institution of Engineering and Technology.

Huxtable, S. T., D. G. Cahill, et al. (2003). "Interfacial heat flow in carbon nanotube suspensions." *Nature materials*, **2**, 731-734.

Iijima, S. (1991). "Helical microtubules of graphitic carbon." *Nature*, **354**, 56-58.

Johnson, K. L. and J. A. Greenwood (1997). "An Adhesion Map for the Contact of Elastic Spheres." *Journal of Colloid and Interface Science*, **192**, 326-333.

Johnson, K. L., K. Kendall, et al. (1971). "Surface Energy and the Contact of Elastic Solids." *Proceedings of the Royal Society A: Mathematical, Physical and Engineering Sciences*, **324**, 301-313.

Ju, Y. S. and K. E. Goodson (1999). "Phonon scattering in silicon films with thickness of order 100 nm." *Applied Physics Letters*, **74**, 3005-3007.

Keesom, W. H. and A. P. Keesom (1936). "On the heat conductivity of liquid helium." *Physica*, **3**, 359-360.

Kim, P. (2002). "Mesoscopic thermal transport and energy dissipation in carbon nanotubes." *Physica B: Condensed Matter*, **323**, 67-70.

Kim, P., L. Shi, et al. (2001). "Thermal Transport Measurements of Individual Multiwalled Nanotubes." *Physical Review Letters*, **87**, 215502.

Kumar, S. and J. Y. Murthy (2009). "Interfacial thermal transport between nanotubes." *Journal of Applied Physics*, **106**, 084302.

Kurti, N., B. V. Rollin, et al. (1936). "Preliminary experiments on temperature equilibria at very low temperatures." *Physica*, **3**, 266-274.

Li, D., Y. Wu, et al. (2003). "Thermal conductivity of Si/SiGe superlattice nanowires." *Applied Physics Letters*, **83**, 3186-3188.

Li, D., Y. Wu, et al. (2003). "Thermal conductivity of individual silicon nanowires." *Applied Physics Letters*, **83**, 2934-2936.

Li, Q., C. Liu, et al. (2009). "Thermal Boundary Resistances of Carbon Nanotubes in Contact with Metals and Polymers." *Nano Letters*, **9**, 3805-2809.

Li, Q., C. Liu, et al. (2009). "Measuring the thermal conductivity of individual carbon nanotubes by the Raman shift method." *Nanotechnology*, **20**, 145702.

Liu, W. and M. Asheghi (2005). "Thermal conduction in ultrathin pure and doped single-crystal silicon layers at high temperatures." *Journal of Applied Physics*, **98**, 123523.

Lü, X., J. H. Chu, et al. (2003). "Modification of the lattice thermal conductivity in semiconductor rectangular nanowires." *Journal of Applied Physics*, **93**, 1219-1229.

Maruyama, S., Y. Igarashi, et al. (2006). "Anisotropic Heat Transfer of Single-Walled Carbon Nanotubes." *Journal of Thermal Science and Technology*, **1**, 138-148.

Matkovich, V. I. (1977). Boron and Refractory Borides. Berlin, Heidelberg, New York, Springer-Verlag.

Maugis, D. (1992). "Adhesion of Spheres: The JKR-DMT Transition Using a Dugdale Model." *Journal of Colloid and Interface Science*, **150**, 243-269.

Maune, H., H.-Y. Chiu, et al. (2006). "Thermal resistance of the nanoscale constrictions between carbon nanotubes and solid substrates." *Applied Physics Letters*, **89**, 013109.

Mavrokefalos, A., N. T. Nguyen, et al. (2007). "In-plane thermal conductivity of disordered layered WSe[sub 2] and (W)[sub x](WSe[sub 2])[sub y] superlattice films." *Applied Physics Letters*, **91**, 171912.

Mavrokefalos, A., M. T. Pettes, et al. (2007). "Four-probe measurements of the in-plane thermoelectric properties of nanofilms." *The Review of scientific instruments*, **78**, 034901.

Medwick, P. A., H. E. Fischer, et al. (1994). "Thermal conductivity and specific heat of boron carbides." *Journal of Alloys and Compounds*, **203**, 67-75.

Mingo, N. and D. A. Broido (2005). "Carbon Nanotube Ballistic Thermal Conductance and Its Limits." *Physical Review Letters*, **95**, 096105.

Mingo, N., L. Yang, et al. (2003). "Predicting the Thermal Conductivity of Si and Ge Nanowires." *Nano Letters*, **3**, 1713-1716.

Mirmira, S. R. and L. S. Fletcher (1998). "Review of the Thermal Conductivity of Thin Films." *Journal of Thermophysics and Heat Transfer*, **12**, 121-131.

Nan, C.-W., G. Liu, et al. (2004). "Interface effect on thermal conductivity of carbon nanotube composites." *Applied Physics Letters*, **85**, 3549.

Palaci, I., S. Fedrigo, et al. (2005). "Radial Elasticity of Multiwalled Carbon Nanotubes." *Physical Review Letters*, **94**.

Pettes, M. T. and L. Shi (2009). "Thermal and Structural Characterizations of Individual Single-, Double-, and Multi-Walled Carbon Nanotubes." *Advanced Functional Materials*, **19**, 3918-3925.

Pilkey, W. D. (1994). Formulas for Stress, Strain, and Structural Matrices, John Wiley & Son, Inc.

Poker, D. and C. Klabunde (1982). "Temperature dependence of electrical resistivity of vanadium, platinum, and copper." *Physical Review B*, **26**, 7012-7014.

Pop, E., D. Mann, et al. (2006). "Thermal Conductance of an Individual Single-Wall Carbon Nanotube above Room Temperature." *Nano Letters*, **6**, 96-100.

Poudel, B., Q. Hao, et al. (2008). "High-thermoelectric performance of nanostructured bismuth antimony telluride bulk alloys." *Science*, **320**, 634-638.

Prasher, R. (2008). "Thermal boundary resistance and thermal conductivity of multiwalled carbon nanotubes." *Physical Review B*, **77**.

Prasher, R., X. Hu, et al. (2009). "Turning Carbon Nanotubes from Exceptional Heat Conductors into Insulators." *Physical Review Letters*, **102**.

Rego, L. G. C. and G. Kirczenow (1998). "Quantized Thermal Conductance of Dielectric Quantum Wires." *Physical Review Letters*, **81**, 232-235.

Roark, R. J. and W. C. Young (1975). Formulas for Stress and Strain, McGraw-Hill Book Company.

Schelling, P. K., S. R. Phillpot, et al. (2002). "Comparison of atomic-level simulation methods for computing thermal conductivity." *Physical Review B*, **65**.

Schmechel, R. and H. Werheit (1999). "Correlation between structural defects and electronic properties of icosahedral boron-rich solids." *Journal of Physics: Condensed Matter*, **11**, 6803-6813.

Schmidt, A. J., K. C. Collins, et al. (2010). "Thermal conductance and phonon transmissivity of metal–graphite interfaces." *Journal of Applied Physics*, **107**, 104907.

Schwab, K., E. A. Henriksen, et al. (2000). "Measurement of the quantum of thermal conductance." *Nature*, **404**, 974-977.

Shenogin, S. (2004). "Role of thermal boundary resistance on the heat flow in carbon-nanotube composites." *Journal of Applied Physics*, **95**, 8136.

Shenogina, N., S. Shenogin, et al. (2005). "On the lack of thermal percolation in carbon nanotube composites." *Applied Physics Letters*, **87**, 133106.

Shi, L. "Data Processing Uncertainty Analysis Version 4." *unpublished*.

Shi, L., Q. Hao, et al. (2004). "Thermal conductivities of individual tin dioxide nanobelts." *Applied Physics Letters*, **84**, 2638.

Shi, L., D. Li, et al. (2003). "Measuring Thermal and Thermoelectric Properties of One-Dimensional Nanostructures Using a Microfabricated Device." *Journal of Heat Transfer*, **125**, 881-888.

Shi, L., J. Zhou, et al. (2009). "Thermal probing of energy dissipation in current-carrying carbon nanotubes." *Journal of Applied Physics*, **105**, 104306.

StanfordResearchSystems (2007). manual of SR850 DSP Lock-In Amplifier. Sunnyvale, Stanford Research Systems.

Swartz, E. T. and R. O. Pohl (1989). "Thermal boundary resistance." *Reviews of Modern Physics*, **61**, 605-668.

Taylor, R. (1966). "The thermal conductivity of pyrolytic graphite." *Philosophical Magazine*, **13**, 157-166.

Tighe, T. S., J. M. Worlock, et al. (1997). "Direct thermal conductance measurements on suspended monocrystalline nanostructures." *Applied Physics Letters*, **70**, 2687-2689.

Tsen, A. W., L. A. K. Donev, et al. (2008). "Imaging the electrical conductance of individual carbon nanotubes with photothermal current microscopy." *Nature Nanotechnology*, **4**, 108-113.

Utke, I., P. Hoffmann, et al. (2000). "Focused electron beam induced deposition of gold." *J. Vac. Sci. Technol. B*, **18**, 3168-3171.

Venkatasubramanian, R., E. Siivola, et al. (2001). "Thin-film thermoelectric devices with high room-temperature figures of merit." *Nature*, **413**, 597-602.

Volz, S. G. and G. Chen (1999). "Molecular dynamics simulation of thermal conductivity of silicon nanowires." *Applied Physics Letters*, **75**, 2056-2058.

Walkauskas, S. G., D. A. Broido, et al. (1999). "Lattice thermal conductivity of wires." *Journal of Applied Physics*, **85**, 2579.

Wang, P., Q. Shi, et al. (2008). "Enhanced environmental mobility of carbon nanotubes in the presence of humic acid and their removal from aqueous solution." *Small*, **4**, 2166-2170.

Werheit, H. (2006). Thermoelectric Properties of Boron-Rich Solids and their Possibilities of Technical Application. 25th International Conference on Thermoelectrics.

Werheit, H., A. Leithe-Jasper, et al. (2004). "Some properties of single-crystal boron carbide." *Journal of Solid State Chemistry*, **177**, 575-579.

Wood, C. (1986). "Boron Carbides As High Temperature Thermoelectric Materials." *AIP conference proceedings*, **140**, 362-372.

Wood, C., D. Emin, et al. (1985). "Thermal conductivity of boron carbides." *Physical Review B*, **31**, 6811-6814.

Xu, T. T., A. W. Nicholls, et al. (2006). "Boron Nanowires and Novel Tube-Catalytic Particle-Wire Hybrid Boron Nanostructures." *Nano*, **1**, 55-63.

Xu, T. T., J.-G. Zheng, et al. (2004). "Crystalline Boron Nanoribbons: Synthesis and Characterization." *Nano Letters*, **4**, 963-968.

Yang, J., Y. Yang, et al. (2011). "Measurement of the Intrinsic Thermal Conductivity of a Multiwalled Carbon Nanotube and Its Contact Thermal Resistance with the Substrate." *Small*, **7**, 2334-2340.

Yang, J., Y. Yang, et al. (2012). "Enhanced and switchable nanoscale thermal conduction due to van der Waals interfaces." *Nature Nanotechnology*, **7**, 91-95.

Yu, A., P. Ramesh, et al. (2008). "Enhanced Thermal Conductivity in a Hybrid Graphite Nanoplatelet - Carbon Nanotube Filler for Epoxy Composites." *Advanced Materials*, **20**, 4740-4744.

Yu, C., S. Saha, et al. (2006). "Thermal Contact Resistance and Thermal Conductivity of a Carbon Nanofiber." *Journal of Heat Transfer*, **128**, 234.

Yu, C., L. Shi, et al. (2005). "Thermal Conductance and Thermopower of an Individual Single-Wall Carbon Nanotube." *Nano Letters*, **5**, 1842-1846.

Yu, N. and A. A. Polycarpou (2004). "Adhesive contact based on the Lennard-Jones potential: a correction to the value of the equilibrium distance as used in the potential." *Journal of Colloid and Interface Science*, **278**, 428-435.

Zhbanov, A. I., E. G. Pogorelov, et al. (2010). "Van der Waals Interaction between Two Crossed Carbon Nanotubes." *ACS Nano*, **4**, 5937-5945.

Zhong, H. and J. Lukes (2006). "Interfacial thermal resistance between carbon nanotubes: Molecular dynamics simulations and analytical thermal modeling." *Physical Review B*, **74**.

Zhou, J., C. Jin, et al. (2005). "Thermoelectric properties of individual electrodeposited bismuth telluride nanowires." *Applied Physics Letters*, **87**, 133109.

Ziman, J. M. (1960). Electrons and Phonons. Oxford, Clarendon Press.